Materials Advances

REVIEW

View Article Online
View Journal | View Issue

Cite this: *Mater. Adv.*, 2025, 6, 8239

Insights into N_2O decomposition in environmental catalysis: evaluation and an advanced outlook

Khezina Rafiq,[a] Mamoona Sabir,[a] Iqra Sadia,[a] Muhammad Zeeshan Abid,[a] Muhammad Arif Nadeem[b] and Ejaz Hussain*[ab]

Nitrous oxide (N_2O) is a potent greenhouse gas and a significant contributor to stratospheric ozone depletion. Its emission arises from a combination of natural and anthropogenic sources, including microbial processes such as nitrification, denitrification, nitrifier denitrification and abiotic chemical pathways such as chemodenitrification and hydroxylamine oxidation. Effective decomposition of N_2O into harmless nitrogen and oxygen is therefore critical for climate mitigation. This review provides a comprehensive overview of the current state of N_2O decomposition, with a focus on mechanisms, catalyst composition and material design strategies. Catalysts are systematically classified based on their decomposition pathways *i.e.* direct catalytic decomposition (DCD), selective catalytic reduction (SCR), and surface-mediated redox processes. In addition, they are further classified on the basis of their compositional attributes, encompassing both precious as well as and non-precious metal-based catalysts systems. Furthermore, a progress-based classification is presented, encompassing classical metal oxides, spinel oxides, layered double hydroxides, MXenes, and metal–organic frameworks (MOFs). Emerging systems such as antenna-reactor catalysts and quantum dots have also been discussed based on their unique properties and potential. Mechanistic insights into N_2O activation, including thermal, surface-catalysed, Mars–van Krevelen-type redox, radical and photocatalytic pathways, are explored in depth. This review highlights the significance of catalyst design, oxygen vacancy engineering and atomically dispersed active sites in enhancing activity and selectivity. Future perspectives emphasize the development of low-cost, thermally stable and environmentally benign catalysts, along with gaining a mechanistic understanding through *in situ* studies and computational modelling. This review aims to guide the rational design of next-generation catalysts for efficient N_2O abatement across industrial and environmental systems.

Received 24th June 2025,
Accepted 13th September 2025

DOI: 10.1039/d5ma00668f

rsc.li/materials-advances

1. Introduction

Climate change has become a challenge to international agencies such as the WHO, EPA, IPCC (Intergovernmental Panel on Climate Change), AFED (Arab Forum for Environment and Development), APAN (Asian Pacific Adaptation Network), CCCCC (Caribbean Community Climate Change Centre), CAN (Climate Action Network), CCL (Citizens' Climate Lobby), CJA (Climate Justice Alliance), EDF (Environmental Defense Fund, USA), HEA (Health and Environmental Alliance) and NRDC (Natural Resources Defense Council).[1] For a long time, nitrous oxide (N_2O) was not considered a significant environmental pollutant, and it did not receive much attention from an environmental perspective. In recent decades, N_2O has been recognized as a potent greenhouse gas. It contributes to the greenhouse effect by trapping the heat in Earth's atmosphere and leading to global warming. In addition, it is believed to play a role in the destruction of ozone in the stratosphere, contributing to ozone layer depletion.[2] The presence of N_2O in the atmosphere causes acid rain, which can have detrimental effects on the ecosystem and environment. Moreover, N_2O raises a particular concern due to its long atmospheric lifetime, estimated at approximately 120 years. This means that once released into the atmosphere, it persists for a very long time.[3] The global warming potential (GWP) of N_2O is nearly 310 times that of carbon dioxide (CO_2). This high GWP makes it a significant contributor to climate change.[4] Chemical industries, especially those involving processes such as nitric acid production and the industrial synthesis of adipic acid, are major sources of anthropogenic N_2O emissions. Specifically, in the synthesis of adipic acid, N_2O is produced when a cyclohexanone/cyclohexanol mixture reacts with nitric acid. It is noted that N_2O emissions from the adipic acid industry contribute a substantial percentage (5–8%) to anthropogenic sources of N_2O in the atmosphere.[5,6] Both natural and anthropogenic sources of N_2O exist, with industrial sources responsible for emitting a significant amount (400–500 kt) annually.[7]

[a] *Institute of Chemistry, Inorganic Materials Laboratory 52S, The Islamia University of Bahawalpur, 63100, Pakistan. E-mail: ejaz.hussain@iub.edu.pk, khezina.rafiq@iub.edu.pk*
[b] *Catalysis and Nanomaterials Lab 27, Department of Chemistry, Quaid-i-Azam University, Islamabad 45320, Pakistan*

2. N_2O generation mechanisms

N_2O is generated through multiple pathways, primarily mediated by microbial processes, and also *via* abiotic chemical reactions. Key mechanisms include nitrification, where ammonia is oxidized and N_2O is formed as a by-product, and denitrification, where nitrate is reduced to nitrogen gases, often realising N_2O when the process in incomplete. Nitrifier denitrification also plays a role under oxygen-limiting conditions, while abiotic chemical reactions, such as nitrate reduction by iron or manganese, contribute to additional N_2O fluxes. On top of natural processes, human activities significantly amplify these emissions, particularly through intensive agriculture, wastewater management and industrial processes. Different mechanisms are summarized in this section, shown in Fig. 1.

2.1. Nitrification

Nitrification is an aerobic microbial process where ammonium (NH_4^+) or ammonia (NH_3) is oxidized to nitrate (NO_3^-) *via* nitrite (NO_2^-). This process is mediated by ammonia-oxidizing archaea (AOA), as well as nitrate-oxidizing bacteria (NOB) in a two-step sequence. The oxidation of hydroxylamine (NH_2OH), a key intermediate, can inadvertently release N_2O as a by-product. N_2O production during nitrification is particularly pronounced under suboptimal oxygen conditions, low pH, or high substrate (ammonia) availability, which destabilize the electron transport chain in AOB. Moreover, recent studies have suggested that AOA contribute significantly to N_2O emissions in acidic soils, where bacterial nitrification is less efficient. Thus, nitrification represents both a fundamental nitrogen cycle process and a critical source of N_2O in agricultural and natural soils.[8]

2.2. Denitrification

Denitrification is an anaerobic respiratory process in which nitrate (NO_3^-) is sequentially reduced to nitrite (NO_2^-), nitric oxide (NO), nitrous oxide (N_2O) and finally dinitrogen gas (N_2). This pathway is primarily driven by facultative anaerobic bacteria such as *Pseudomonas*, *Paracoccus*, and *Bacillus* species under low-oxygen or anoxic conditions. The process requires organic carbon as an electron donor, linking it closely to carbon cycling. The accumulation of N_2O often occurs when the enzyme nitrous oxide reductase (NosZ), responsible for reducing N_2O to N_2, is inhibited by low pH, low copper availability, or the presence of oxygen. As a result, soils and sediments under fluctuating oxygen conditions, such as wetlands, wastewater systems, and agricultural fields after irrigation, often exhibit high N_2O fluxes. Denitrification is considered the largest single biological source of N_2O globally.[9]

2.3. Nitrifier denitrification

Nitrifier denitrification is a hybrid pathway in which nitrifying organisms, under oxygen-limited or microaerophilic conditions, reduce nitrite (NO_2^-) to nitric oxide (NO), nitrous oxide (N_2O) and nitrogen gas (N_2). Unlike conventional denitrification carried out by facultative anaerobes, this process is mediated by ammonia-oxidizing bacteria (AOB). The pathway is particularly relevant in soils, sediments, and wastewater treatment systems where oxygen availability fluctuates. Nitrifier denitrification can account for substantial N_2O emissions when ammonia and nitrite are both abundant, such as in fertilized agricultural soils. It provides a mechanistic link between nitrification and denitrification, highlighting the versatility of microbial nitrogen metabolism under transitional redox conditions.[8]

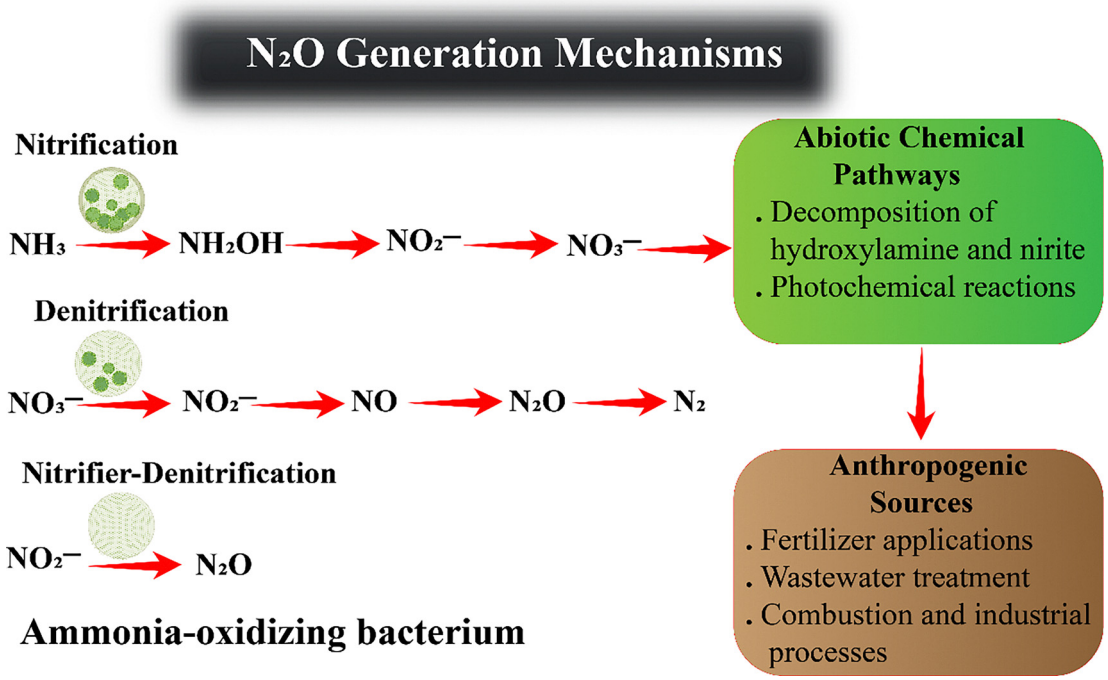

Fig. 1 Key mechanisms of N_2O generation.

2.4. Abiotic chemical pathways

Although microbial processes dominate, abiotic pathways also contribute to N_2O formation. These include: (i) chemodenitrification: it involves the reduction of nitrites by ferrous ions (Fe^{2+}) or other reductants, leading to N_2O release. This mechanism is common in waterlogged soils, sediments and mining-impacted environments with high levels of reduced metals. (ii) Oxidation of hydroxylamine can occur through reactions with metal oxides, particularly ferric (Fe^{3+}) and manganese (Mn^{4+}) oxides, producing N_2O and NO. Additionally, photochemical reactions in sunlit waters and soils have been reported to drive abiotic N_2O formation from nitrite. While biotic pathways may represent a smaller fraction globally, they can dominate under specific geochemical conditions, especially in soils rich in iron or manganese.[10]

2.5. Anthropogenic sources

Human activities have amplified N_2O emissions far beyond natural background levels. These include (i) agriculture: excessive application of nitrogen-based fertilizers (urea, ammonium nitrate) and livestock manure leads to surplus reactive nitrogen in soils, fueling nitrification, denitrification and nitrifier denitrification. Agricultural soils are estimated to contribute more than 60% of global anthropogenic N_2O emissions. (ii) Wastewater treatment: biological nitrogen removal processes, particularly in activated sludge and sequencing batch reactors, release N_2O due to incomplete nitrification and denitrification under variable oxygen conditions. Emerging evidence shows that wastewater plants may be hotspots of N_2O release if not properly managed. (iii) Industrial processes: N_2O is also released during the production of nitric acid (used in fertilizers) and adipic acid (used in nylon manufacture). Though mitigation technologies exist, incomplete adoption leads to continued emissions. (iv) Biomass burning and fossil fuel combustion: smaller but notable contributions come from burning crop residues, forests, and fossil fuels, releasing reactive nitrogen that indirectly contributes to N_2O formation. Together, these anthropogenic sources have increased atmospheric N_2O concentrations to record highs, making it the third most important long-lived greenhouse gas and a major contributor to stratospheric ozone depletion. Fig. 2a shows the distribution of natural *versus* anthropogenic sources.

3. Categories of N_2O decomposition catalysts based on their mechanisms and compositions

Catalysts for N_2O decomposition are generally classified into different categories depending on their catalytic mechanism, composition, and support material. This classification helps us

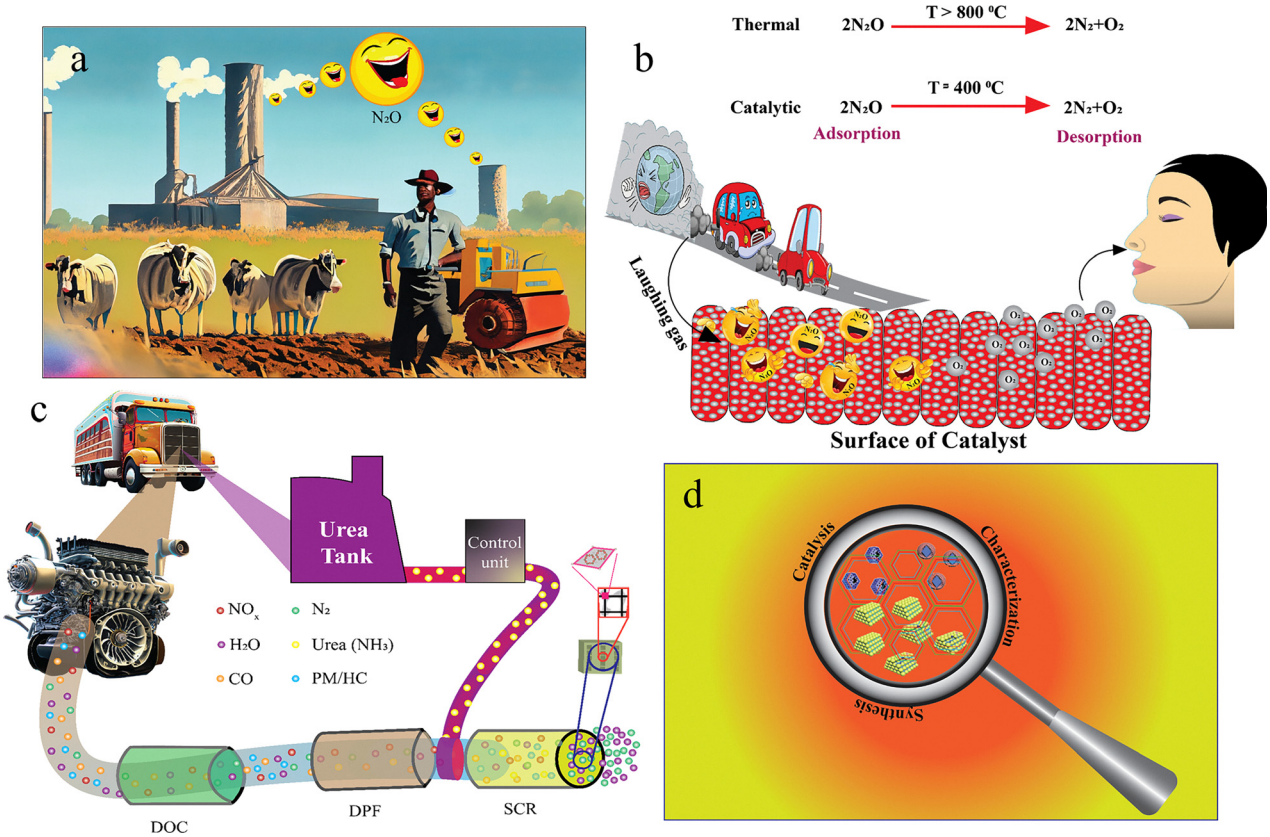

Fig. 2 (a) Natural and anthropogenic sources of N_2O (infamous laughing gas). (b) Thermal and catalytic paths of N_2O decomposition. (c) Functioning of Cu-exchanged zeolites in the selective catalytic reduction of NO_x from mobile sources.[11] Reproduced with permission from the American Chemical Society (Copyright©2013) (d). Advances in zeolite synthesis and characterization techniques for heterogeneous catalysis.

in understanding theory operational principles, activity under industrial conditions, cost-effectiveness and long-term stability. A detailed overview of each category is presented below.

3.1. Based on catalytic mechanisms

3.1.1. Direct catalytic decomposition (DCD). In this mechanism, catalysts decompose nitrous oxide (N_2O) directly into N_2 and O_2 without the need for a reducing agent:

$$2N_2O \rightarrow 2N_2 + O_2$$

Examples of such catalysts include metal oxides [such as cobalt oxides (Co_3O_4), iron oxide (Fe_2O_3) and manganese oxide (MnO_2)], perovskites (*e.g.* $La_{1-x}Sr_xCoO_3$ with tunable oxygen vacancies that improve oxygen mobility and enhance N_2O activation) and spinels (*e.g.* $CuFe_2O_4$, $MnAl_2O_4$) known for their stable structures and redox properties. In DCD, oxygen vacancies on these catalysts adsorb and activate N_2O, leading to bond cleavage and release of N_2. The oxygen atoms are either released as O_2 or incorporated temporarily into the lattice. These catalysts are widely considered for industrial emission control (*e.g.* nitric acid plants) where large volumes of N_2O are generated.

3.1.2. Selective catalytic reduction (SCR). In SCR, a reducing agent (such as NH_3, CO or hydrocarbons like CH_4 and C_3H_6) is introduced to facilitate the reduction of N_2O into N_2:

$$N_2O + 2CO \rightarrow N_2 + 2CO_2$$

$$N_2O + 2NH_3 \rightarrow 2N_2 + 3H_2O$$

Examples of these catalysts include Fe- or Cu-exchanged zeolites (Fe–ZSM-5, Cu–SSZ-13, and Cu–ZSM-5) and vanadium-based catalysts (V_2O_5/TiO_2 and $V_2O_5–WO_3/TiO_2$). The reducing agent reacts with oxygen species from N_2O decomposition, enhancing N_2 formation. SCR can operate at relatively low temperatures compared to DCD, making it practical for vehicular exhaust systems and stationary sources. SCR is often applied in mixed gas systems such as automotive exhausts, power plants, and mobile sources. Fig. 2c demonstrates the role of Cu-zeolites in ammonia-assisted SCR of N_2O, particularly effective in diesel engines.

3.2 Based on catalyst compositions

3.2.1. Precious metal-based catalysts. Precious metals such as Rh, Ru, Pt and Pd are highly active for N_2O decomposition. They promote rapid N–O bond cleavage due to their strong adsorption capacity for N_2O. Examples include Rh/Al_2O_3, Ru/CeO_2, and Pt/ZrO_2. High catalytic activity and efficiency at relatively low temperatures are their key advantages. Their limitations are high cost (that makes them less suitable for large-scale industrial use) and susceptibility to deactivation due to sintering or poisoning (*e.g.* by sulphur or water vapours). They are often used in niche or specialized applications where high efficiency is required despite high costs (*e.g.* medical gas purification or research setups).

3.2.2. Non-precious metal-based catalysts. Non-precious metals (mainly transition metals and mixed oxides) are more cost-effective and environmentally sustainable, making them widely used in industrial processes. Examples include transition metal oxides (*e.g.* Co_3O_4, MnO_x, CuO, and Fe_2O_3), perovskites ($LaCoO_3$, $LaMnO_3$, and Sr-doped cobaltites with enhanced oxygen mobility), spinels ($CuFe_2O_4$ and $MnAl_2O_4$) and zeolites (Fe–ZSM-5 and Cu–SSZ-13 with high hydrothermal stability). Their advantages include low cost, abundant raw materials and high thermal stability. They generally require higher operating temperatures than that needed for precious metals, but can be optimized by doping or adding promoters. These are widely employed in industrial emission abatement systems, including nitric acid and adipic acid plants, as well as power generation facilities.

3.3 Based on support types

The support material plays a crucial role in dispersing active catalytic sites, enhancing redox behaviour, and providing structural stability under harsh reaction conditions. Common supports include metal oxides such as Al_2O_3, TiO_2 and CeO_2 due to their high surface area and redox properties. CeO_2, in particular, enhances oxygen storage and mobility, improving the catalytic efficiency. Zeolites include framework structures (such as ZSM-5, SSZ-13 and beta-zeolites) provide high surface area and microporosity. Their ion-exchange ability allows the incorporation of Fe or Cu cations, which significantly enhances SCR activity. SSZ-13 is particularly noted for high hydrothermal stability under automotive exhaust conditions. In carbon-based supports, activated carbon and graphene are sometimes used due to their large surface area and electrical conductivity. However, they are less common for N_2O decomposition because of limited thermal stability at high operating temperatures. The choice of support directly influences catalyst dispersion, durability, oxygen mobility and tolerance to poisons (*e.g.* SO_2 and H_2O). Hence, support selection is as important as the active catalytic phase itself.

4. Significance of catalytic decomposition of N_2O

N_2O is also a by-product in various industrial processes, including the catalytic abatement of nitrogen oxides (NO_x) in three-way catalytic converters and selective catalytic reduction (SCR) of NO_x with NH_3. As N_2O is a significant greenhouse gas and its emission contributes to the global warming and climate change, there is a pressing need to reduce N_2O emissions from anthropogenic sources. One effective and economical method to reduce N_2O emissions is the catalytic decomposition of N_2O into its elemental components (nitrogen and oxygen), which is known as catalytic decomposition of N_2O.[12,13] To make it effective, the catalyst must be durable and selective. Durability ensures long-term effectiveness of the catalyst and selectivity ensures that N_2O is effectively converted into nitrogen and oxygen without the formation of undesirable by-products.[14] Catalysts designed for N_2O decomposition should be stable even in the presence of moisture, as they may encounter atmospheric moisture during real-world applications. N_2O decomposition is an exothermic

reaction, meaning that it releases heat during the process. This can occur either thermally (without any catalyst) or catalytically (Fig. 2b). The choice between these paths depends on the factors such as operating temperature and the amount of catalysts used.[15] However, noble metal-based photocatalysts are among reliable options for N_2O decomposition. These catalysts utilize noble metals (*e.g.* Pt and Pd) to facilitate the decomposition of N_2O under the influence of light, making them a potential choice for efficient N_2O abatement.[16]

A considerable amount of work has been done in the catalytic decomposition of N_2O, and a number of catalyst systems with various compositions such as zinc, platinum, copper oxides and zeolites have been developed.[17] Metal surfaces,[18] supported metals,[19] metal oxides,[20,21] supported oxides,[22] ternary oxides,[23] spinel oxides,[24] perovskite-type oxides,[25] hydrotalcites,[26] and transition metal exchanged zeolites[27] are well-known catalysts that can decompose N_2O into its elements even at low temperatures. In this review, important categories of N_2O decomposition catalysts are covered, which include transition metal-based zeolites, hydrotalcites, spinel oxides, mixed metal oxides, metal/metal oxides in mesoporous silica, metal oxides, metal-doped nanotubes, nanosheets and nanocages, graphene and graphitic oxides/nitrides, metal–organic frameworks (MOFs), and MOF-derived catalysts. This review compares the different synthesis strategies of catalyst fabrication, experimental conditions, catalyst characterization techniques, N_2O decomposition temperatures and catalytic efficiencies of various catalysts (Fig. 2d).

5. Progress-based systematic classification of N_2O decomposition catalysts

N_2O decomposition catalytic materials are classified into five main categories based on their structure, composition and research progress/maturity. Each category includes subtypes ordered by their level of maturity, from well-established (extensively studied) to emerging (recently developed or still under intense research).

5.1. Classical metal oxide-based catalysts

Classical metal oxide-based catalysts such as Fe_2O_3, Co_3O_4 and MnO_2 are most well-established and extensively studied for decades. They are renowned for their thermal stability, redox flexibility, and cost-effectiveness. These oxides typically possess high oxygen mobility and variable oxidation states, enabling efficient N_2O decomposition *via* lattice oxygen participation. Their simple structures allow for easy synthesis, scalability, and tunability through doping or morphology control. Spinel-type oxides, in particular, exhibit strong metal–oxygen interactions and good resistance to sintering. Despite their maturity, continued research enhances their surface area, dispersion, and durability under reaction conditions. Their robustness and versatility make them fundamental benchmarks in both industrial and environmental catalytic applications. Four categories of these catalysts are particularly important with respect to N_2O decomposition.

5.1.1. Metal oxide catalysts. Transition metal oxides such as NiO, Co_3O_4, MnO_2, CuO, Cr_2O_3 and Fe_2O_3 exhibit high catalytic activity for the decomposition of N_2O. The transition metal oxides are known for their high thermal and chemical stability, making them suitable candidates for catalytic applications.[28–30] For example, Gaidei and co-workers synthesized a series of oxide catalysts containing up to 30% active metal components on an alumina carrier. The temperature dependence of N_2O decomposition on these catalysts follow a well-defined S-shaped curve, similar to Pt family metals, but these transition metal oxide catalysts are somewhat less active than Pt-based catalysts. The catalytic activity of these metal oxide catalysts was ranked as follows in the increasing order of decomposition temperature: $Fe_2O_3 < Cr_2O_3 < CuO < MnO_2 < NiO < Co_3O_4$. Among the catalysts based on non-noble metals, Co_3O_4 showed the highest catalytic activity. The calculated activation energy values for these catalysts vary, with CuO and Cr_2O_3 having the highest E_a (187–176 kJ mol^{-1}) and MnO_2, Co_3O_4 and NiO having lower values (133–143 kJ mol^{-1}). Based on experimental data, Co, Cu, Mn and Cr oxides are recommended as active components for developing deposited catalysts based on non-noble metals.[31] Fig. 3 signifies the use of acidic and high valence metal sites on the various metal oxide catalysts based on MnO_x, CeO_2, Fe_2O_3, VO_x and CuO for the NH_3-assited SCR of NO_x.[32]

CaO obtained from the domestic limestone has also demonstrated its catalytic effect in N_2O decomposition. The effects of CO and CO_2 on N_2O conversion activity were found antagonistic to each other. On the one hand, CO increases the N_2O decomposition activity. On the other hand, higher CO_2 concentrations slowly decrease the N_2O decomposition activity. As NO was also a hindering factor in N_2O decomposition, in order to lessen its concentration, N_2O was concurrently passed in the circulating fluidized bed combustion (CFBC) reactor. Selective non-catalytic reduction (SNCR) is a method of choice for the NO removal from flue gas.[33] Similarly, various Bi-based semiconductors were fabricated by a hydrothermal strategy,[34–36] *e.g.* Liu group examined monoclinic $BiVO_4$, orthorhombic Bi_2MoO_6 and Bi_2WO_6 catalysts for the photocatalytic degradation of N_2O into N_2 and O_2, as shown in Fig. 4a. They found that $BiVO_4$ exhibited the highest degradation activity due to stronger absorption of visible light and higher charge separation.[37]

Metal-supported metal oxide catalysts are also popular for N_2O decomposition reactions. Komvokis *et al.* synthesized a series of Ru/Al_2O_3 nanocatalysts *via in situ* reduction with ethylene glycol (EG) and compared their N_2O reduction activity with the catalysts prepared through the typical incipient wetness procedure. The EG reduction approach resulted in the formation of spherical Ru nanoparticles (particle size: 1–3 nm; dispersion: 70–35%). While impregnated calcined catalysts had larger sized nanoparticles with a very small dispersion degree (particle size: 10–80 nm; dispersion: 10%). The catalysts synthesized *via* EG reduction showed significantly higher N_2O decomposition activity in an O_2-rich environment irrespective of CO, CO_2, NO, H_2O and SO_2. The higher surface area of Ru metal

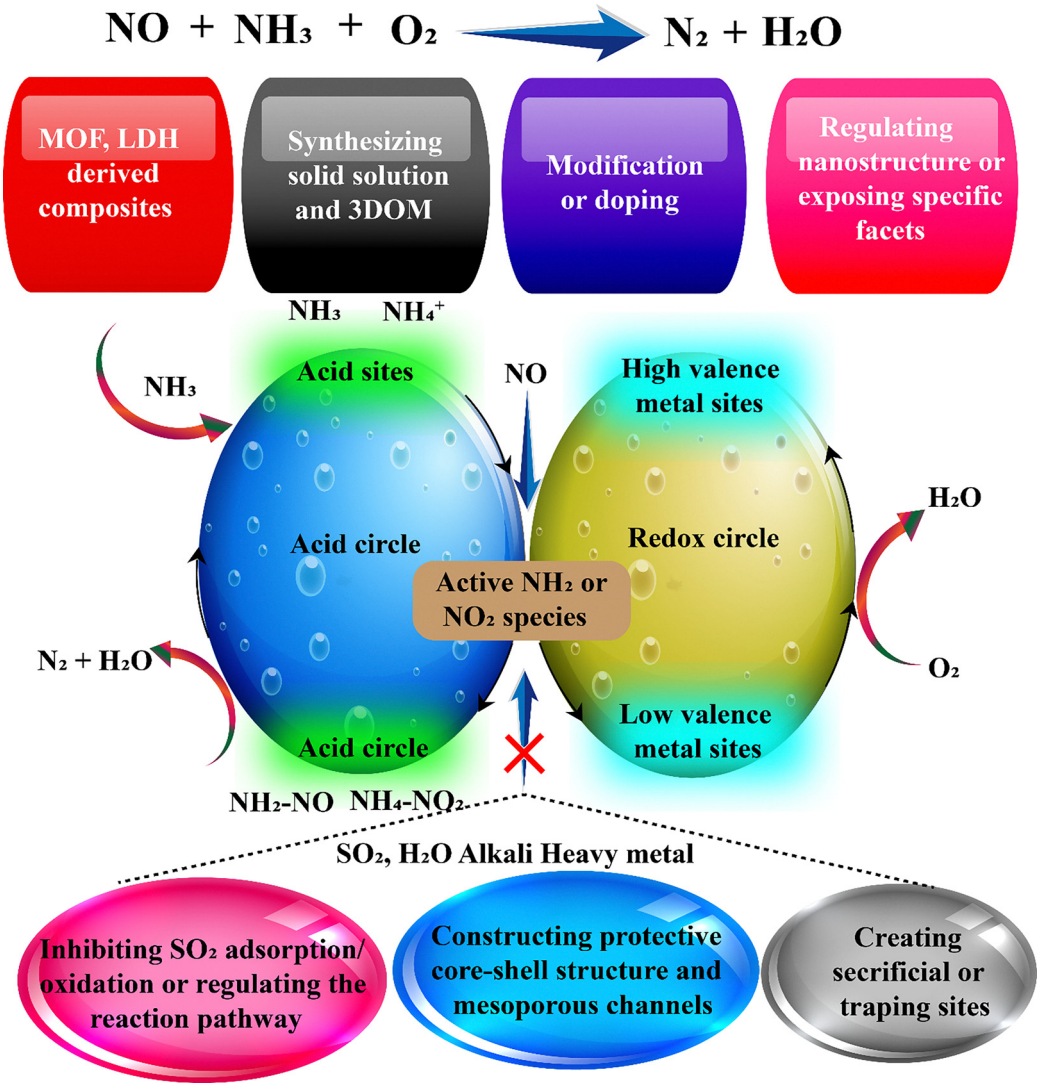

Fig. 3 Selective catalytic reduction of nitrogen oxides with NH_3 employing various acidic metal oxide composite catalysts.[32] Reproduced with permission from the American Chemical Society (Copyright©2019).

contributes to their higher catalytic activity. These catalysts have a low apparent activation energy, which suggests that they require less energy to initiate the chemical reaction. Ru/Al_2O_3 nanocatalysts can be regenerated effectively that helps to restore their catalytic activity, achieving a conversion rate of over 90%.[39] Similarly, Reddya *et al.* synthesized alumina-supported Pd catalysts (Pd/Al_2O_3) employing the deposition precipitation (DP) and impregnation (IMP) methods and studied their effect on N_2O conversion activity. Higher catalytic efficiency was recorded for DP catalysts as compared to their IMP equivalents due to the formation of partially oxidized Pd^{2+} species over the surface of the DP–Cl catalyst.[40]

In a general N_2O decomposition reaction, CO is adsorbed over the surface of catalysts to reduce N_2O, but this strong adsorption of CO may lead to the catalyst's poisoning. For example, Zhang *et al.* have utilized the Mans-van-Krevelen mechanism by employing phosphotungstic acid (PTA)-supported single-atom catalysts (SACs), M/PTA, where M = Fe, Co, Mn, Rh, Ru, Ir, Os, Pt and Pd. Adsorbed CO reacts with the surface oxygen atoms of PTA support and create holes on the M/PTA surface. N_2O acts as an oxygen donor to regenerate catalyst and releases N_2. It was also demonstrated that among all metals, Pd/PTA, Rh/PTA and Pt/PTA are most efficient catalysts. Fig. 4b shows the mechanism for the reduction of N_2O by CO over M/PTA catalysts.[38] Metals such as Co, Cu or Fe supported on ZrO_2 are also active in the decomposition of N_2O. The activity pattern is Co > Cu ≫ Fe. ZrO_2 catalysts have the advantage of hydrothermal stability. Unlike that of zeolite systems, their catalytic activity is recovered when H_2O vapours are eliminated from the feed gas.[41]

Tuti *et al.* further investigated N_2O adsorption and decomposition on ZrO_2. At 25 °C, N_2O molecularly adsorbs through the O_2 end on Zr^{4+} sites and dissociative adsorption of N_2O occurs on surface defect sites, *i.e.* Zr^{3+} sites. It was noted that N–N bond dissociation did not occur and oxygen atoms of the lattice become incorporated into the product O_2 molecules.[42]

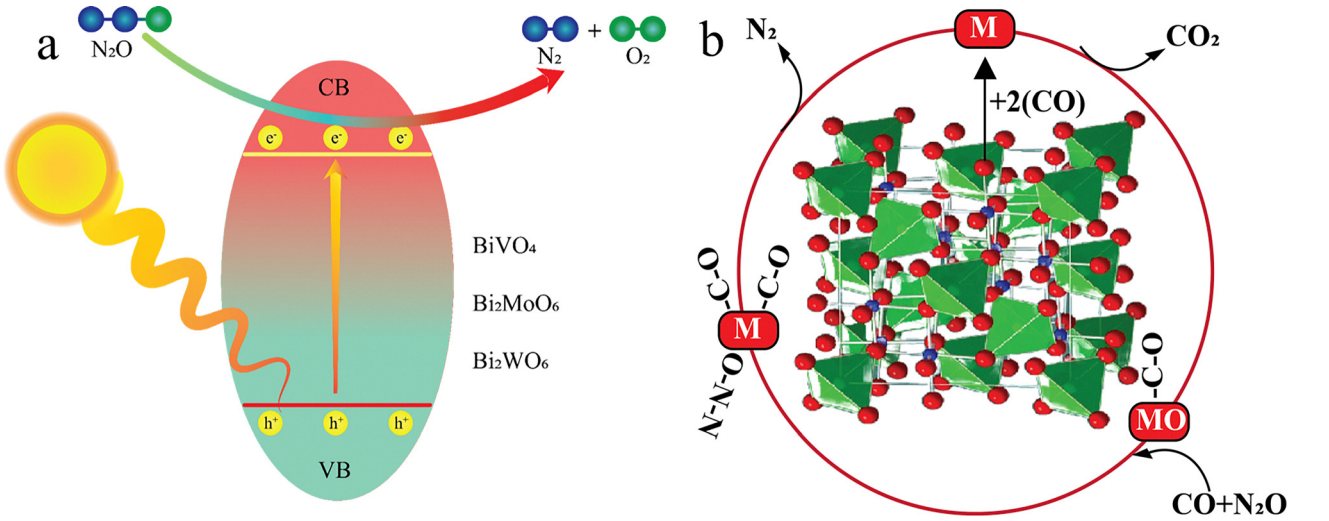

Fig. 4 (a) Photocatalytic N_2O decomposition *via* Bi-based photocatalysts (*i.e.* $BiVO_4$, Bi_2MoO_6 and Bi_2WO_6) under visible light irradiation.[37] Reproduced with permission from the American Chemical Society (Copyright©2018). (b) Mans–van Krevelen mechanism over phosphotungstic acid supported SACs for the reduction of N_2O by CO.[38] Reproduced with permission from the American Chemical Society (Copyright©2019).

In a different study, researchers have used a cluster model represented by $M(OH)_3(H_2O)_2$, where M represents different transition metals such as Co, Fe and Rh. The results indicated that Rh and Co sites were more active for the N_2O decomposition reaction as compared to Fe. The rate-limiting step is the formation of adsorbed O_2 molecules *via* the interaction of adsorbed oxygen atoms with N_2O. A correlation was observed between the activation energy (E_a) and the strength of the M–O bond. Weaker metal-adsorbed oxygen bonds for Co and Rh sites facilitated the decomposition of the second N_2O molecule into O_2, lowering the activation barrier.[43] In the case of $Fe(OH)_3(H_2O)_2$, the transition state analysis suggested that N_2O dissociation was achieved through electron density donation from the metal to an N_2O molecule.[44] Various other examples of N_2O decomposition metal oxide catalysts are provided in Table 1.

5.1.1.1. Shortcomings of metal oxide catalysts. Though pure metal oxides show the highest catalytic efficiencies in the cases of transition metal oxides of group VIII and some rare earth oxides (*e.g.* La), it is also worthwhile to note that, based upon experimental conditions, metal oxides including MnO_2, MnO, Cu_2O and CoO are not stable and are partially decomposed.[54] As a result, N_2O decomposition studies took a turn towards the development of more active and stable catalytic systems. Another important fact about pure metal oxide catalysts is the utilization of high temperature for catalyzing N_2O decomposition because of the limited availability of active sites at low temperatures due to adsorbed oxygen recombination. In addition, the presence of H_2O exerts a negative effect on catalytic efficiency due to its competitive adsorption on active sites.[21]

5.1.1.2. Application scenario: nitric acid plants. Metal oxide catalysts such as Co_3O_4, Fe_2O_3 and MnO_2 are low-cost, stable, and effective for N_2O decomposition under high-temperature conditions typical of nitric acid plants. They offer thermal robustness and environmental compatibility but require elevated activation temperatures, show reduced efficiency at intermediate ranges and are vulnerable to deactivation by H_2O and SO_2 impurities.

5.1.2. Spinel oxides. Spinel oxides, having the structural formula of AB_2O_4, show high thermal stability and redox

Table 1 Overview of synthesis methods, reaction conditions and various techniques employed during the course of analysis of metal oxide-based catalysts for N_2O decomposition

Catalysts	Method of preparation	Reaction atmosphere	Air speed (mL min^{-1})	N_2O decomposition temp-range (°C K^{-1})	Techniques used for the characterization and assessing the activity of catalysts	Ref.
CaO catalysts	Hydrothermal	—	—	1073–1273 K	DFT method, on-line gas flue analyzer, GC	45
γ-Fe_2O_3	Co-precipitation	N_2	50	100–400 °C	XRD, XPS, FTIR	46
Al-doped MoS_2	—	Ethylene oxide	—	—	DFT	47
3.0F–Co_3O_4	Sol–gel	Ar	50	250–450 °C	TEM, HRTEM	48
Ti_3O_6@TiO_2	—	—	—	—	DFT	49
Ni > Co > Fe > Cu	Impregnation	N_2	400	200–500 °C	DFT	50
Co_3O_4	Sol–gel	—	—	—	UV-visible spectra, H_2-TPR, XPS, TEM, EXAFS, EDS, NAP-XPS	51
$Sm_{0.1}$–Co_3O_4	Sol–gel	Ar	50	300–500 °C	XRD, XPS, STEM, EELS, H_2-TPR	52
N-doped Co_3O_4	Sol–gel	H_2/N_2	30	150–500 °C	FTIR, XRD, TEM, EDX, XPS, O_2-TPD	53

activity. In several redox reactions such as the reduction of N_2O and oxidation of higher hydrocarbons and CO, cobalt spinel catalysts have been widely investigated.[55] It has been demonstrated that Co_3O_4 is more active in CO oxidation than Fe_2O_3, Cu_2O, NiO, MnO, V_2O_5, Cr_2O, CeO_2 and ZnO. Because of its capability to bind quickly with oxygen and a very low M–O bond energy, cobalt spinel is believed to display the highest activity in hydrocarbon oxidation.[56] Fig. 5 represents the synthesis and use of various metal spinels in different electronic materials (ORR and OER).[57]

Shen *et al.* investigated the catalytic conversion of N_2O using cobalt oxide catalysts supported on various materials and synthesized using a co-precipitation method. Among the supports tested, alkaline MgO was found to be the most effective due to its strong electron-donating properties. Here cobalt existed in the form of Co_3O_4 nanoparticles dispersed in the MgO matrix. Under specific conditions, the Co–MgO-15% catalyst demonstrated good activity on decomposing N_2O, making it a potential candidate for mitigating greenhouse gas emissions from anthropogenic sources.[58] The advantages of using Co oxide-based spinel catalysts lie in their capability to decompose N_2O below 400 °C and sufficient catalytic activity. Another benefit of using spinel oxide catalysts containing Rh is that they exhibit unusual catalytic activities in the absence of water but these catalysts rapidly lose their activity upon exposure to water.[59,60]

Researchers have tried to find whether the catalytic activity of cobalt spinel oxide catalysts is influenced by the addition of gases such as NO_2, NO, O_2 and H_2O vapours or not. It has been found that operating the reaction at 850 °C led to a higher N_2O conversion rate than operating the reaction at 800 °C.

This improvement was attributed to the presence of O_2, which altered the oxidation state of Co in the catalyst.[25]

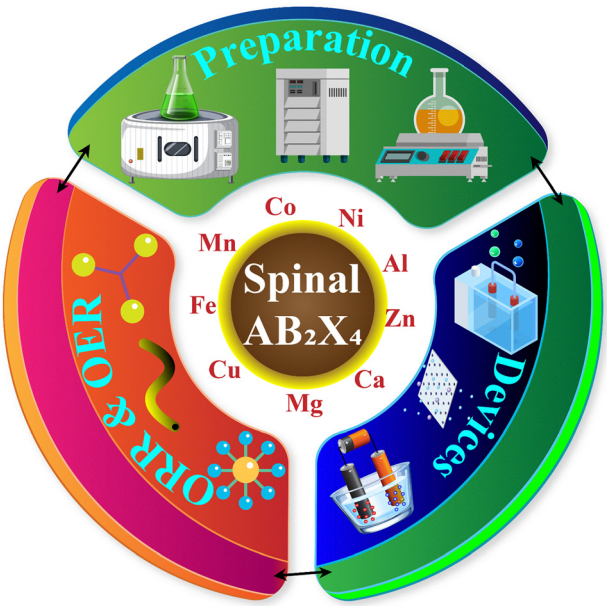

Fig. 5 Synthesis routes and applications of spinel oxides (AB_2X_4).[56] Reproduced with permission from the American Chemical Society (Copyright©2017).

However, at lower temperatures, the presence of O_2 reduced N_2O conversion. H_2O vapours also have a detrimental effect on the catalyst's activity at all temperatures. This was likely due to the competitive chemisorption of H_2O vapours on the active sites, hindering N_2O decomposition. Unlike O_2 and H_2O vapours, however NO_2 did not decompose over the cobalt catalyst and it did not impact the catalyst's state. It had no effect on N_2O conversion. However, the presence of NO in the feed gas mixture at 850 °C led to higher N_2O reduction values. This was attributed to NO's influence on the process, possibly affecting the last phase of N_2O decomposition. The state of catalyst was also influenced by temperature variations, particularly when exposed to a feed gas mixture containing O_2, N_2O and Ar at temperatures ranging from 700 °C to 850 °C.[61] Extensive examples of the N_2O decomposition by spinel oxide catalysts are enlisted in Table 2.

5.1.2.1. Shortcomings of spinel oxide catalysts. Spinel oxide catalysts often suffer from limited surface area and poor dispersion of active sites, reducing their catalytic efficiency. Their high-temperature synthesis can lead to particle sintering, decreasing reactivity. Additionally, some spinels exhibit slow oxygen mobility and reduced activity at low temperatures, limiting their applicability under mild reaction conditions. Stability under hydrothermal conditions can also be a concern.

5.1.2.2. Application scenario: industrial flue gas treatment. Spinel oxides are attractive for N_2O decomposition in industrial flue gas streams due to their structural stability, redox flexibility and cost-effectiveness. They operate efficiently at high temperatures and tolerate thermal stress, but limitations include moderate activity at lower temperatures and susceptibility to poisoning by SO_2 and H_2O commonly present in flue gases.

5.1.3. Hydroxyapatites. Hydroxyapatites, having the formula $Ca_{10}(PO_4)_6(OH)_2$, act as dual catalysts in acid-base and redox catalysis. They enable moderate activity for N_2O decomposition. Their flexible structure allows ion substitution (*e.g.* with transition metals), enhancing catalytic sites. They exhibit good thermal stability and surface hydroxylation but generally require modification for high activity. Their tenability makes them suitable for multifunctional or hybrid catalytic systems under mild conditions.[81]

In the 1990s, hydroxyapatite catalysts (containing calcium and phosphate ions) were employed for indirect N_2O decomposition *via* partial oxidation of methane.[82,83] However, during the last few years, hydroxyapatites have been used as supports for Rh and Ru catalysts in N_2O abatement.[84,85] Galloni *et al.* evaluated Cu- and Fe-loaded hydroxyapatite catalysts for N_2O decomposition, revealing superior Cu performance due to nanoparticle formation, with detailed structural, stability and resistance analyses supporting catalytic behaviour.[86] Wei *et al.* obtained natural hydroxyapatite from bone, and after doping it with Co ions, Co/nHAP catalysts were prepared and utilized for the investigation of N_2O decomposition reaction.[62] Fig. 6a shows the mechanistic pathway of N_2O reduction over a Co/nHAP catalyst, while Fig. 6b indicates N_2O conversion profiles with respect to the increasing temperature. Similarly, Tan *et al.* synthesized hydroxyapatite-supported bimetallic (Fe, Rh) catalysts for plasma-

Table 2 Overview of synthesis methods, reaction conditions and various techniques employed during the course of analysis of different spinel oxide catalysts for N_2O decomposition

Catalysts	Methods	Reaction atmosphere	Air speed (mL min^{-1})	N_2O decomposition temp-range (°C K^{-1})	Techniques used for characterization and activity of catalysts	Ref.
Co/nHAP	Hydrothermal	Ar	—	200–600 °C	XRD, TEM, HADDF–STEM, XPS	62
(Co_3O_4) (CS–N)	Co-precipitation	—	—	100–400 °C	XRD	63
Co_3O_4	Hydrothermal	He	30	100–600 °C	O_2-TPD, DFT calculations, XRD, FTIR, SEM, XRF, TPSR	55
Co_3O_4-based catalyst	Co-precipitation	N_2	50	400–600 °C	XRF, XRD, H_2-TPR, TEM, EDX, SAED	64
Cs-doped Co-spinel catalysts (Cs–Co_3O_4)	Wetness impregnation	—	—	<200 °C	XRF, XRD, SEM, XPS, Raman, TPCR, QMS	65
deNO_x and deN_2O	Precipitation	—	—	425–450 °C	FTIR	66
$Cu_xCo_{1-x}Co_2O_4$ spinel-oxide catalysts	Co-precipitation	N_2	200	150–500 °C	TGA, DTA, FTIR, XRD	67
Co_3O_4	PVA-assisted precipitation	N_2	65	300–600 °C	DFT, XRD, XPS, TEM, SEM, FTIR, EPR	68
Co_3O_4	PVA-assisted precipitation	—	—	150–450 °C	XRD	69
K-doped $Cu_xCo_{3-x}O_4$ catalysts	Thermal decomposition	O_2	20	250–650 °C	XRD, TGA, TPR, N_2-physisorption, O_2-TPD, ICP-OES, BET	70
Co–Mn–Al mixed oxide catalysts	Precipitation	H_2	50	40–450 °C	AAS, XRD, SEM, Raman, FTIR, TPR-H_2, TPD-N_2O, SEM, EDS, MS	71
Co-based spinel oxides	Impregnation	—	50	25–400 °C	XRD, BET, H_2-TPR, O_2-TPD, XPS	59
Ag_xCo (x = 0–0.08) oxide catalysts	Co-precipitation	Ar	30	200–400 °C	XRD, TEM, O_2-TPD, BET, H_2-TPR, GC-TCD, XPS	72
Bi–Co_3O_4 catalysts	Co-precipitation	Ar	50	200–500 °C	O_2-TPD, BET, XRD, GC	73
Alien cations doped-nanocrystalline Co-spinel catalysts	Co-precipitation	He	30	100–600 °C	XRD, Raman, BET, XPS, H_2-TPR, TEM	74
LT-deN_2O catalysts (K/$Zn_{0.4}Co_{2.6}O_4$/αAl_2O_3)	Co-precipitation	—	—	405–445 °C	FTIR using on-line analyzer	75
$Zn_xCo_{1-x}Co_2O_4$ spinel catalyst	Co-precipitation	O_2	10	—	XRD, EDX	76
Co_3O_4–Cs	Wet impregnation	H_2	50	100–400 °C	XPS, SEM, H_2-TPR, XRD	77
Cd–Co_3O_4 spinel catalysts	Co-precipitation	—	—	—	TGA, DTA, XRD, FTIR, N_2-physisorption, AAS	78
N-doped Co_3O_4	Sol–gel method	H_2/N_2	30	200–500 °C	XRD, FTIR, Raman, N_2-physisorption, TEM, EDX, HADDF–STEM, H_2-TPR, O_2-TPD, EPR, CO_2-TPD	53
$(CuMgNiZn)_1Co_2O_4$ catalysts	Co-precipitation	H_2	50	150–500 °C	DFT, TPSR	79
Mn–Fe spinel catalysts	Co-precipitation	H_2	100	100–400 °C	NH_3-TPD, NO-TPD, DRIFTS, FTIR, DFT	80

assisted N_2O decomposition studies. In this instance, reaction temperature was lowered to a higher degree as free radicals generated by plasma initiated the catalytic decomposition reaction faster even at low temperatures.[87] Fig. 6c and d indicate the mechanism and conversion profiles of N_2O. More examples are represented in Table 3.

5.1.3.1. Shortcomings of hydroxyapatite catalysts. These catalysts face several limitations including relatively low intrinsic activity compared to conventional metal oxides. Their performance heavily depends on metal ion doping, as pure HAP is largely inactive. Additionally, achieving uniform dispersion of active sites can be a challenge. They may also show reduced thermal stability under harsh conditions, and are susceptible to deactivation by sulphur or alkali contaminants without proper modification.

5.1.3.2. Application scenario: wastewater treatment facilities. These catalysts offer tunable surface properties, ion-exchange capacity and good thermal stability, making them promising for N_2O decomposition in wastewater treatment off-gases. Their biocompatibility and low costs are additional advantages. However, they often show limited intrinsic activity, require modification with transition metals to enhance performance, and may suffer from deactivation under humid, impurity-rich gas conditions.

5.1.4. Mixed metal oxide catalysts. A lot of work has already been conducted on mixed metal oxide systems, *e.g.* metal-doped oxides and transition metal ions in inert matrices. Due to the unusual structure, thermal stability, synthesis at high temperature and low SSAs, the mixed metal oxides are famous for their N_2O decomposition activity.[93] Transition metal ions are very specific in their activity based on their oxidation state, *e.g.* MgO matrix-dispersed Mn(III) ions showed the highest catalytic efficiency as compared to Mn(II) and Mn(IV).[94] However, the supported oxides possess better practical applications than pure and mixed metal oxides because of higher dispersion of metal ions in the large surface areas of different well-known supports including alumina, mesoporous silica, zirconia, ceria and titania. The catalytic efficiency is determined by metal loading, method of synthesis, and temperature.

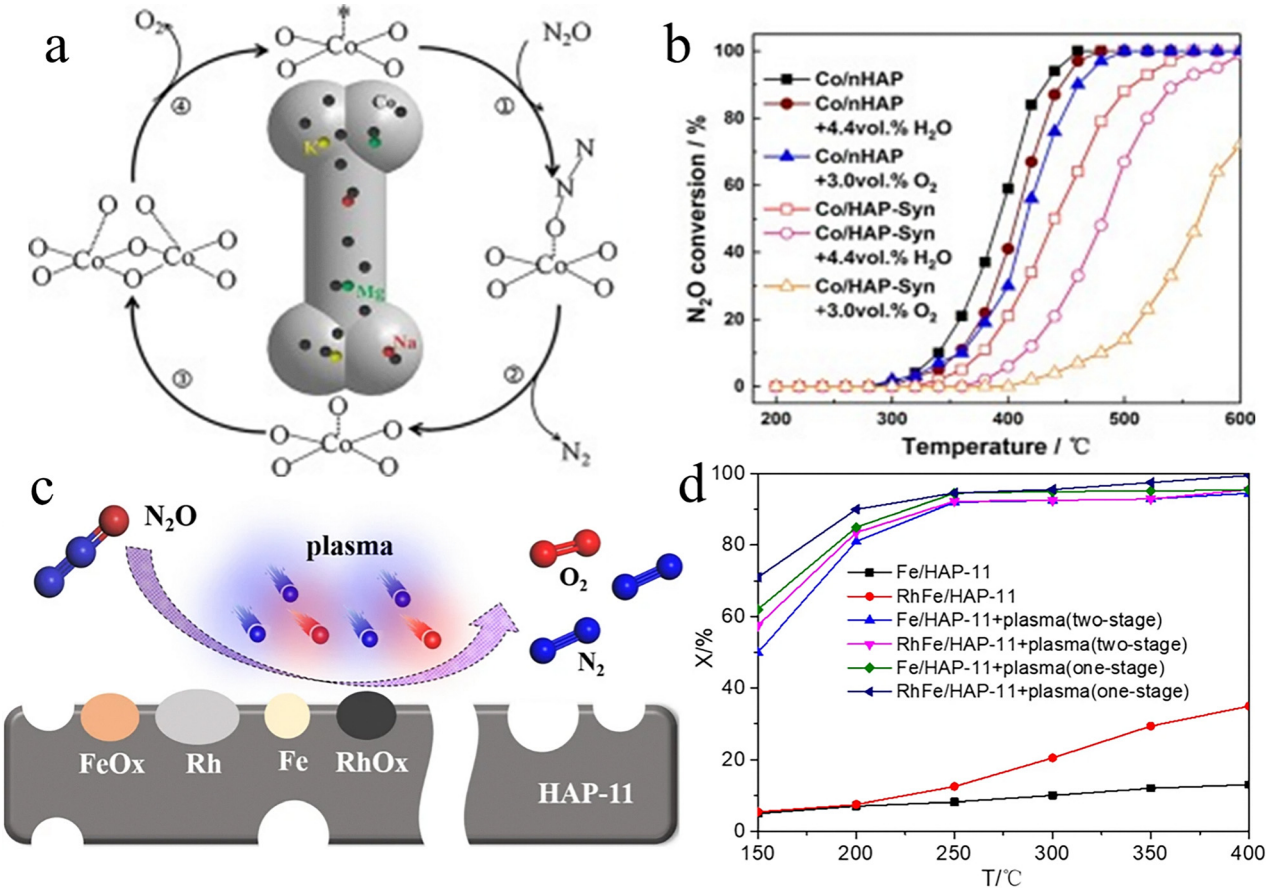

Fig. 6 (a) Break down of N_2O over the surface of Co-doped bone-derived hydroxyapatite (Co/nHAP) catalysts. (b) N_2O decomposition profile.[62] Reproduced with permission from Elsevier (Copyright©2020). (c) Mechanism of plasma-assisted N_2O degradation over the surface of bimetallic RhFe/HAP catalysts. (d) Variation in % N_2O decomposition w.r.t. temperature on RhFe/HAP and Fe/HAP catalysts.[87] Reproduced with permission from Springer-Nature (Copyright©2023).

Table 3 Overview of synthesis methods, reaction conditions and various techniques employed during the course of analysis of hydroxyapatite-based catalysts for N_2O decomposition

Catalysts	Method	Reaction atmosphere	Air speed (mL min^{-1})	N_2O decomposition temp-range (°C K^{-1})	Techniques used for characterization and activity of catalysts	Ref.
Hydroxyapatite-supported RhO_x catalysts (RhO_x-HAP)	Wet impregnation	O_2	30	150–400 °C	XRD, TEM, ICP, XPS, BET, CO_2-TPD, O_2-TPD, GC, FT-IR	88
RuO_x/M−P−O catalysts	Impregnating	H_2/He	10	150–400 °C	ICP–OES, XRD, BET, TEM, XPS, CO_2-TPD, O_2-TPD, H_2-TPR, GC-TCD, QMS	84
Co/Hydroxyapatite	Hydrothermal	—	—	100–900 °C	XRD, TEM, HRTEM, EDX, STEM, UV-vis	89
Hydroxyapatite supported Rh, Fe, and Rh–Fe catalysts	Impregnation	He	60	150–200 °C	XRD, SEM, TEM, TG, XPS, CO_2-TPD	87
Hydroxyapatite (HAP, $Ca_{10}(PO_4)_6(OH)_2$)	Hydrothermal	NO	15	400–450 °C	N_2-physisorption, XRPD, NH_3-titration, UV-DRS, Mössbauer, XPS, and EXAFS	90
Calcium hydroxyapatite (HAP, $Ca_{10}(PO_4)_6(OH)_2$)	Co-precipitation	—	—	120–800 °C	UV-DRS and Mössbauer spectroscopies, NH_3 titration, N_2-physisorption and XRPD	91
Apatite-supported Co_3O_4	Co-precipitation	H_2/N_2	30	300–600 °C	XRD, XPS, H_2-TPR, TEM, Raman, FT-IR	92

For the purpose of efficient N_2O abatement, mixed metal oxide catalysts have been proved to be very effective catalysts.[95–98] Beyer *et al.* studied the N_2O decomposition over different Rh-supported metal and non-metal oxides, *e.g.* Rh/SiO_2, Rh/MgO, Rh/Al_2O_3, Rh/TiO_2 and Rh/CeO_2, in both the presence and the absence of O_2. Rh/SiO_2 and Rh/MgO showed high catalytic activity for N_2O conversion, even at low temperatures in the presence of O_2. In Rh/Al_2O_3, Rh/TiO_2 and Rh/CeO_2, smaller sized Rh nanoparticles were abundant, resulting in lower catalytic activities. The particle size of Rh was a crucial factor affecting the overall catalytic performance.[99] The redox properties of active Rh components were affected by the acid-base properties of the support. The reduction

abilities of Rh species decreased as the basicity of the support increased, indicating a strong interaction of Rh species with O_2. Han *et al.* employed mesoporous TiO_2@Fe_2O_3@Al_2O_3 core-shell nanostructures for low-temperature selective catalytic reduction (SCR) of NO_x. It effectively prevented the deposition of sulphur compounds and accelerated the SCR of NO_x by facilitating electron transfer at the Fe_2O_3–TiO_2 interface. Fig. 7a depicts the comparison of mechanisms for the standard SCR with the fast SCR that these catalysts follow.[100]

Similarly, Gaidei *et al.* also synthesized and compared N_2O decomposition activities of various Rh-supported metal oxide catalysts, *i.e.* Rh/ZrO_2, Rh/Al_2O_3 and Rh/Al_2O_3–SiO_2. The catalysts were exposed to an intimal temperature of 450 °C in a reactor. As a result, they exhibited excellent dynamic characteristics to initiate and sustain the reaction. The catalyst's activity decreased over time. Unloaded catalysts achieved 100% decomposition of N_2O within the temperature range of 460–480 °C that indicated its effectiveness in promoting decomposition reaction. X-ray analysis revealed the presence of phase transitions in carrier materials and oxidation of Rh during the operational time.[102] In yet another study, Ratanatawanate *et al.* have devised a method that combined PbS QD-decorated TiO_2 nanotubes with S-nitrosocysteine that released NO_2 that further produced singlet oxygen.[101] The whole setup for the attachment of PbS QDs with the surface of TiO_2 nanotubes and release of NO_2 is shown in Fig. 7b.

Imamura *et al.* investigated the impact of adding praseodymium (Pr) to CeO_2 to investigate the catalytic decomposition of N_2O. They prepared a catalyst by incorporating Rh on Pr/CeO_2 composites. These catalysts were then subjected to calcination at different temperatures. However, the presence of Pr alone did not significantly affect the catalytic activity. A significant acceleration in the N_2O decomposition rate was observed, as the calcination temperature of the catalysts was increased. Notably, the catalytic performance of the Rh-supported composite oxides (Pr–Rh/CeO_2) calcined at 800 °C was found to be most effective.[103] One of the chief advantages of Rh-doped ceria catalysts is that they retain an exceptionally high catalytic efficiency even in the presence of oxygen and water. Because of the hydrophobic nature of Rh/CeO_2 catalysts, they are much less sensitive to moisture than the other catalysts.[104] In another investigation, Peck *et al.* fabricated a series of CeO_2-supported Fe_2O_3 and Co_2O_3 catalysts along with the increase in the metal loadings to determine monolayer surface coverage on the CeO_2 support. It results in higher catalytic activities through the maximization of supporting metal–oxygen bonds. NO_x was reduced by CO in the presence of sufficient amounts of O_2.[105] Fig. 8 represents the overall layout of NO_x reduction by CO.

N_2O decomposition was also tested on mixed metal oxides containing noble metals (*i.e.* Pt and Pd) supported on various oxide materials. The type of support material has a significant impact on the initial decomposition of N_2O. Important support materials include SiO_2 and Al_2O_3. At low temperatures (298 K), the Pt/SiO_2–Al_2O_3 catalysts showed low activity compared to the other catalytic systems. However, their activity boosted at higher temperatures (573 K). This suggested that the support material's influence on N_2O decomposition depends on the reaction temperature.[106] Another important aspect of the support effect is change in the N_2O conversion with pulse numbers. In most cases, N_2O decomposition exhibited a steep decrease with the increase in pulse number. However, Pt/SiO_2–Al_2O_3 catalysts showed exceptionally high N_2O conversion rates at the second and third pulses.[107]

Rh-, Ru-, and Ir-based mixed metal oxides exhibited the highest activity in decomposing N_2O. However these catalysts are susceptible to oxidation at high temperatures due to their oxidation potentials. Ru- and Ir-based metal oxide catalysts tend to form highly volatile oxides at elevated temperatures, leading to the loss of active metal components and a decrease in catalytic activity. Given its stability in the context of N_2O decomposition, Rh is recommended as the preferred active component for catalysts used in this reaction.[108] Table 4 presents various examples of mixed metal oxide catalysts utilized for N_2O abatement studies.

5.1.4.1. Shortcomings of mixed metal oxide catalysts. Mixed metal oxide catalysts, despite their tunable composition and synergistic effects, often suffer from limited control over active site uniformity and metal dispersion. Their synthesis can lead to phase separation or undesired crystallinity, reducing the catalytic efficiency. Additionally, some systems exhibit poor low-temperature activity and deactivation under long-term operation, especially in the presence of moisture or contaminants. Scalability and reproducibility also remain a challenge for complex multi-metal formulations.

5.1.4.2. Application scenario: nitric acid plant emissions. Mixed metal oxides are highly effective for N_2O abatement in nitric acid plant emissions due to their synergistic redox properties, abundant oxygen vacancies and strong thermal stability. They are cost-efficient and tunable, but challenges include maintaining long-term stability under fluctuating gas conditions and vulnerability to poisoning by SO_2 and water vapour.

5.2. Layered and framework structures

Layered and framework structure-based catalysts such as zeolites, hydrotalcites and mesoporous silica-supported systems offer unique structural advantages for N_2O decomposition. Their well-defined pores and channels facilitate controlled diffusion and confinement of reactants, enhancing the selectivity and activity. Transition metal ions incorporated into frameworks (*e.g.* Fe–ZSM-5) act as isolated redox centres, promoting effective N–O bond cleavage.

Hydrotalcites provide tunable acid-base sites and high dispersion of metal species upon calcination. These materials also support ion-exchange capabilities, allowing precise modifications of active sites. However, their catalytic performance can depend heavily on pore architecture, metal loading and thermal stability under reaction conditions. Three classes of this category are given in this section.

5.2.1. Hydrotalcites (layered double hydroxides). With the structural formula of $[M_{1-x}^{2+}M_x^{3+}(OH)_2]^{x+}(A^{n-})^{x-}\cdot yH_2O$, hydrotalcites (HTs) possess excellent anion exchange capacity and

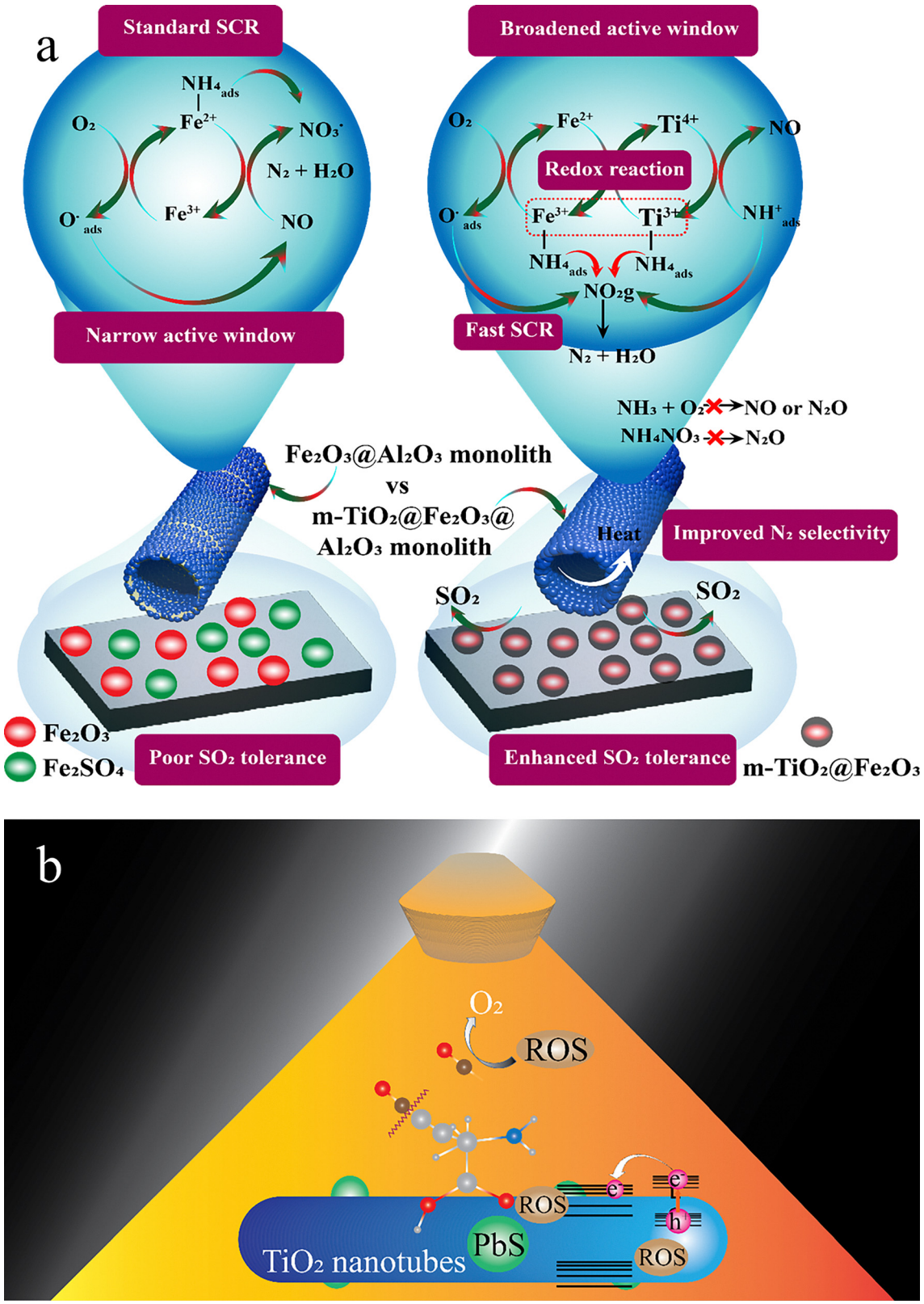

Fig. 7 (a) Mechanism of SO_2-tolerant selective catalytic reduction of NO_x with NH_3 employing mesoporous TiO_2@Fe_2O_3@Al_2O_3 monolith composites at low temperatures.[80] Reproduced with permission from the American Chemical Society (Copyright©2019). (b) Mechanism of NO_2 release *via* the combination of *S*-nitrocysteine with PbS quantum dots decorated TiO_2 nanotubes.[101] Reproduced with permission from American Chemical Society (Copyright©2011).

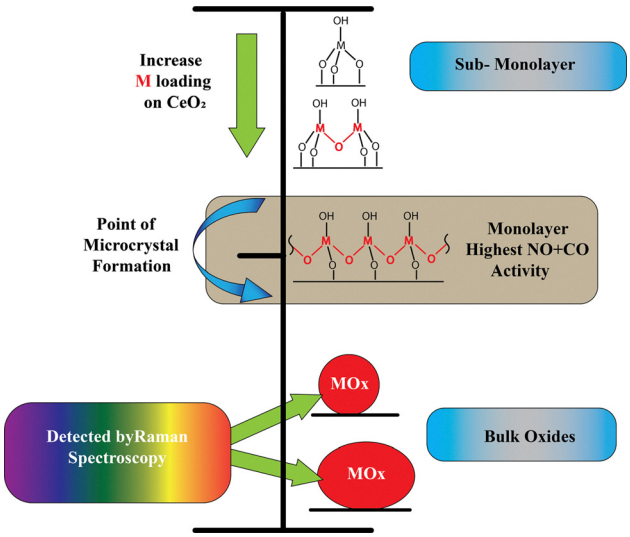

Fig. 8 Structure and activity relationship of ceria-supported Fe and Co oxides for NO reduction by CO.[105] Reproduced with permission from the American Chemical Society (Copyright©2017).

basicity.[75] Their advantages include improved stability, control and efficiency compared to other reaction systems. Because of their flexible structure, hydrotalcite-derived transition metal oxides are considered very active and selective catalysts, even far more efficient than zeolitic catalysts. They are also thermally very stable. When using hydrotalcite catalysts, N_2O decomposes below 500 K. Another benefit of calcined hydrotalcites is that they do not degrade at temperatures above 900 K, thus the high stability makes the hydrotalcite-derived catalysts quite promising for practical applications. Higher calcination temperatures combined with alkali promoters (*i.e.* K) have a great enhancing impact on the N_2O decomposition activity. However, water and oxygen are strong inhibitors of the N_2O conversion performance.[137]

The overall rate of N_2O decomposition reaction depends on the adsorption of N_2O molecules on the catalyst surface during the reaction. This adsorption is a crucial step in the decomposition process. The rapid formation of O_2 led to the fast desorption of adsorbed oxygen, making active sites on the catalyst surface available for further adsorption of N_2O. As a result of fast adsorption and desorption processes, the overall rate of N_2O decomposition is higher. This led to the establishment of first-order rate equation w.r.t the concentration of N_2O.[138]

Layered double hydroxides (LDHs) are successfully employed as starting materials for metal-supported catalysts. Generally, they are synthesized *via* three distinct routes: (1) with elements of redox properties present in between the layer spacing, direct calcination and/or reduction of LDH precursors is required, (2) within the LDH sheets, anionic exchange with the desired metal precursors is crucial, followed by calcination and/or reduction and (3) pre-calcined LDH precursors are impregnated with different inorganic materials followed by calcination and/or reduction.[139] Fig. 9a summarizes all three routes for the synthesis of LDH-derived metal-supported catalysts.

Oxygen molecules tend to adsorb on the catalyst's surface and occupy the active sites, reducing the availability of free active sites for the N_2O decomposition reaction. As a result, the overall N_2O decomposition rate decreases. The Eley–Rideal reaction, that involves the desorption of oxygen, is not active enough to drive the overall N_2O decomposition reaction within the temperature range of 250 °C and 500 °C. This behaviour of oxygen in N_2O decomposition process is different from selective catalytic reduction (SCR) processes where oxygen plays a key role in breaking down organic molecules to produce N_2 from nitrogen oxides.[142] A first-order reaction rate model can be employed to describe the decomposition of N_2O, but it is only applicable when the concentration of N_2O is less than 10 000 ppm. Beyond this range, the reaction kinetics deviate from the first-order behaviour. The presence of impurities in the feed gas can get adsorbed on the active sites of the catalysts, resulting in free defect sites on the surface, which can slowly decrease the rate of N_2O decomposition.[21] De Stefanis *et al.* used catalysts consisting of alumina-pillared smectites, which are a type of layered clay material. These clay materials were exchanged with transition metals.[143] The main focus of this study was to reduce N_2O *via* an eco-friendly decomposition reaction as follows:

$$N_2O \rightarrow N_2 + 1/2O_2$$

This reaction converts N_2O into less harmful nitrogen (N_2) and oxygen (O_2). The results of this study showed that when pillared clays were exchanged with transition metals, the yield of decomposition reaction increased, suggesting that catalysts with transition metals are effective in promoting the N_2O decomposition rate. It was noted that double-exchanged alumina-pillared montmorillonite/beidellite catalysts, exchanged with Ca and Co ions, exhibited the highest decomposition activity for N_2O. Overall, the mechanism suggested that N_2O is first adsorbed on the catalyst surface. Then, it underwent decomposition through catalytic oxidation and reduction.[143] Similarly, Zhang *et al.* synthesized La-hexaaluminates ($LaFe_xAl_{12-x}O_{19}$) having abundant Al sites in the mirror plane (MP) phase, so that the degradation of N_2O can be achieved efficiently. Fig. 9b demonstrates that Fe(III) ions prefer to occupy octahedral Al(III) sites in the MP of aluminate crystals confirming a high activity for N_2O decomposition.[140] Kiss *et al.* reported AlFe–PILC-type catalysts having different metal/OH ratios and employed them for N_2O decomposition reactions.[144] N_2O was 100% converted into N_2 and H_2O on treatment with NH_3 below 500 °C. However, in the direct conversion of N_2O below 500 °C, the activity of catalysts did not exceed 40%. For the N_2O abatement reaction, the catalytic activities of AlFe–PILC-type catalysts prepared with higher metal/OH ratios are higher than the apparent activity of AlFe–PILC-type catalysts having lower metal/OH ratios. It is attributed to the presence of free FeO–Fe_2O_3 particles.[145]

Hydrotalcites have been effectively utilized for dual decomposition of volatile organic compounds (VOCs) and gaseous pollutants. For instance, fabricated and calcined $Cu_xMg_{3-x}AlO$ were examined for 100% primary catalytic oxidation of *n*-butylamine and 83% secondary catalytic reduction of NO_x at a lower temperature of 350 °C, as represented in Fig. 9c.[141]

Table 4 Overview of synthesis methods, reaction conditions and various techniques employed during the course of analysis of different mixed metal oxide catalysts for N_2O decomposition

Catalysts	Methods	Reaction atmosphere	Air speed (mL min^{-1})	N_2O decomposition temp-range (°C K^{-1})	Techniques used for characterization and activity of catalysts	Ref.
Cu/CeO_2	Hydrothermal	H_2/Ar	25	300–450 °C	STEM–EDX, STEM–EELS, H_2-TPR, XPS, *operando* DRS-UV-Vis, DRIFTS, CO-DRIFTS	109
Rh/CeO_2	Hydrothermal	H_2/Ar	40	400 °C	CO-DRIFTS, N_2O-DRIFTS, MCT detector, IR	110
RuO_2/Al_2O_3	Wet impregnation	N_2	1000	25–300 °C	BET surface area measurement, XRD, FT-IR, DBD reactor	111
Ru/Al_2O_3	Impregnation	He	20	250–500 °C	—	112
$PrBaCoCO_3$	Hydrothermal	He	100	200–600 °C	XPS, BET, H_2-TPR, O_2-TPR	25
Cu–Al–O_x mixed metal oxides	Co-precipitation method	He	100	300–450 °C	XRD, ICP-MS, N_2-physisorption, O_2-TPD, H_2-TPR, *in situ* FT-IR and XAFS	113
Metal oxides supported Au-NPs (Au/M_xO_y) (M_xO_y: Al_2O_3, CeO_2, Fe_2O_3, TiO_2 and ZnO)	Deposition precipitation	He	10	400–700 °C	BET, XRD, SEM, HR-TEM, XPS, H_2-TPR, EDS, GC-TCD	114
Co_3O_4/CeO_2 mixed oxide catalysts	Hydrothermal	He	100	300–600 °C	BET, XRD, TEM, H_2-TPR, XPS, GC-TCD	115
K-modified Co–Mn–Al mixed oxides	Hydrothermal	He	50	250–450 °C	ICP, XPRD, H_2-TPR, CO_2-TPD, NO-TPD, XPS, N_2-sorption	116
Co_3O_4/ZrO_2	Hydrothermal	He	30	200–400 °C	XRD, TEM, HRTEM, N_2-physisorption, FTIR, XPS, O_2-TPD, H_2-TPR, GC, Raman	117
K/Y_2O_3–Co_3O_4	Co-precipitation	He/Ar	20	100–400 °C	BET, DTA	118
Nd(Cu,Co)Al–O_x	Co-precipitation	O_2/He	100	50–600 °C	XRD, BET, HRTEM, XPS, H_2-TPR	119
Co_3O_4–$LaCoO_3$	Co-precipitation	He	40	700–850 °C	XRD, BET, FTIR	120
$Mn_xCo_{1-x}Co_2O_4$	Co-precipitation	He	40	100–500 °C	XRF, XRD	121
$LaFeO_3$	Hydrothermal	—	—	250–500 °C	XRD, EDX, XPS	122
MnO_x/TiO_2	Ultrasonic impregnation	N_2	1000	0–400 °C	XRD, EDX, SEM	123
$CuFeO_x$ thin-film catalysts	Adsorption	Ar	20	100–550 °C	XRD, EDX, XPS	124
MnO_2/MO_x (M = Al, Si and Ti)	Wet impregnation	He	60	120–280 °C	XRD, XPS, BET	125
MnO_x/TiO_2	Wet impregnation	—	—	100–300 °C	XRD, BET, HRTEM, XPS, H_2-TPR and NH_3-TPD	126
Pd/CeO_2	Hydrothermal	NH_3/He	20	100–400 °C	XRD, XPS, TEM, FEI	127
Pt/Co_3O_4	Incipient-wetness	H2/Ar	35	100–500 °C	XRD, SEM, TEM, TPO, TPR	128
MnO_x/TiO_2	Ultrasonic impregnation	O_2/Ar/NO/NH_3	1000	0–350 °C	XRD, SEM, XPS, BET	129
Cs-supported Co_3O_4 (Cs/Co)	Co-precipitation	Ar	100	100–300 °C	XRD, XPS, H_2-TPR	130
$Bi_{0.1}NiO_{1.15}$	Co-precipitation	N_2/O_2	3100	300–400 °C	XRD, XPS, H_2-TPR	131
CuO/CeO_2	Co-precipitation	—	—	300–550 °C	STEM, EDX, XRD	132
Pd/γ-Al_2O_3	Impregnation	N_2	6	550–350 °C	XRD, XPS	18
Rh/PTA	—			—	DFT	38
P@SiC	Adsorption	—	—	—	DFT, PDOS	133
(SACs) M1/PTA (M = Fe, Co, Mn, Ru, Rh, Os, Ir & Pt; PTA = $[PW_{12}O_{40}]^{3-}$)	Ion exchange	—	—	—	DFT	134
Fe-substituted La-hexaaluminate supported Ir catalysts	Microemulsion	He	50	384–450 °C	XRD, XPS, DRFTS	135
Rh/CeO_2	Incipient wetness impregnation	Ar	30	300–500 °C	XRD, STEM, EDS, HRTEM, XPS, FTIR, DRIFTS	136

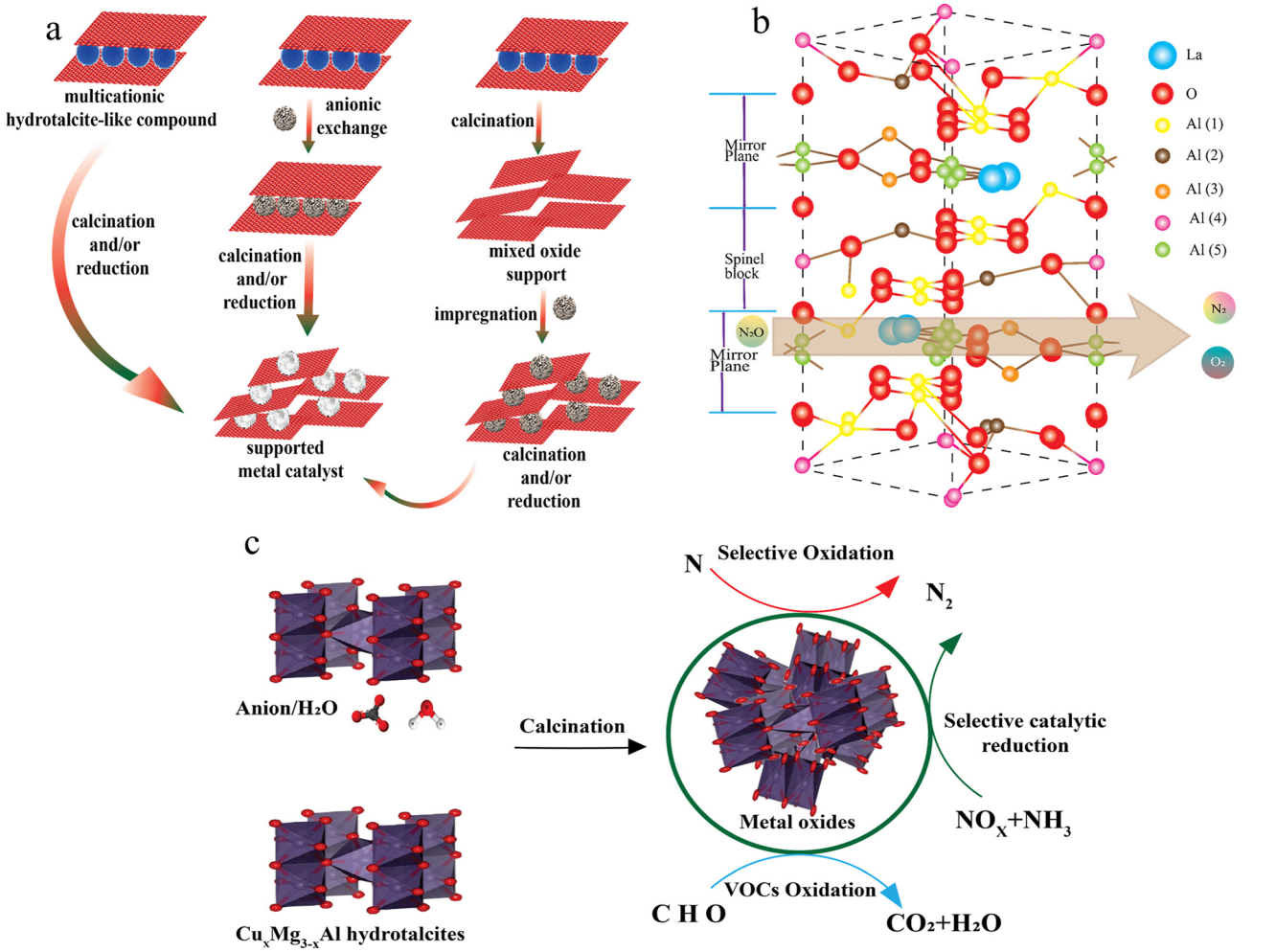

Fig. 9 (a) Representation of main routes leading to the synthesis of metal-supported catalysts from LDH precursors.[139] Reproduced with permission from Springer (Copyright©2003). (b) N_2O decomposition to N_2 and O_2 in the mirror plane phase of perovskite-type La-hexaaluminates ($LaFe_xAl_{12-x}O_{19}$).[140] Reproduced with permission from the American Chemical Society (Copyright©2014). (c) Hydrotalcite-derived $Cu_xMg_{3-x}AlO$ oxides for pollutant-destruction mechanism.[141] Reproduced with permission from the American Chemical Society (Copyright©2019).

In another study, catalytic decomposition of N_2O was estimated at Co/Al hydrotalcites, $[Co_{1-x}Al_x(OH)_2[(CO_3)]_{x/2}\cdot H_2O]$ (where $x \approx 0.25$–0.33), in a static glass reactor at a pressure of $\approx$50 torr within the temperature range of 150–280 °C. Catalysts exhibited a first-order dependence for the N_2O decomposition activity. An increase in Co concentration led to an increased decomposition activity. A higher activity was shown by the catalyst precursor synthesized under a low saturation (LS) method than that synthesized by a sequential precipitation (SP) method.[146] Table 5 presents various examples of hydrotalcites that have been applied for N_2O decomposition.

5.2.1.1. Shortcomings of hydrotalcite catalysts. Hydrotalcite catalysts, while offering tunable composition and high dispersion of active sites, suffer from several drawbacks. Their thermal stability is limited, as structural collapse can occur upon high-temperature calcination. The resulting mixed metal oxides may exhibit low surface area and poor crystallinity. Additionally, their activity in N_2O decomposition is generally moderate, requiring further modifications. Sensitivity to water and contaminants can also affect the long-term performance and catalyst durability.

5.2.1.2. Application scenario: automotive exhaust control. These catalysts with layered double hydroxide structures offer high surface area, tunable composition, and excellent dispersion of active metal sites, making them promising for N_2O decomposition in automotive exhaust systems. They are low cost and versatile but disadvantages include limited intrinsic activity, dependence on metal modification for efficiency and reduced stability under high-temperature, water and sulphur-rich exhaust conditions.

5.2.2. Zeolites with transition metal ions. Zeolite catalysts are among the few early known catalysts for N_2O decomposition, while some show catalytic activities below 600 K.[156] The activity of transition metal ion-exchanged zeolite was determined by the type of transition metal ion (TMI) and zeolite. This is the reason that the activity order for different transition

Table 5 Overview of synthesis methods, reaction conditions and various techniques employed during the course of analysis of different hydrotalcite catalysts for N_2O decomposition

Catalysts	Preparation method	Reaction atmosphere	Air speed (mL min^{-1})	Decomposition temp-range (°C K^{-1})	Techniques used for characterization and activity of catalysts	Ref.
Mn(Fe)$CoAlO_x$ hydrotalcite	Co-precipitation	N_2	100	100–500 °C	XRD, H_2-TPR, TGA, XPS, XAFS, BET	147
Ru/Me_xO_y	Hydrothermal	—	—	300–550 °C	CO_2-TPD, TEM	148
Rh/Mg/Al HT-derived film	Co-precipitation	H_2/Ar	30	50–500 °C	SEM, EDX, TEM, SAED, BET, Raman, H_2-TPR, XPS	149
Hydrotalcite-derived Cu_xCo_y (CuO–Co_3O_4 mixed oxides)	Co-precipitation	N_2	100	350–500 °C	XRD, XPS	150
Hydrotalcite-derived mixed oxides	Ion exchange	H_2	200	300–500 °C	XRD, XPS, BET	151
Hydrotalcite-derived Co_3O_4, Co_3O_4–P	Sol–gel method	—	—	150–400 °C	TEM, TGA, XRD and BET	152
Hydrotalcite-derived [y = Cu/(Cu + Ni)]	Co-precipitation	H_2/Ar	41	600–900 °C	XRD, XPS, TGA–DTA, BET, XPS	153
CoCuAl mixed oxides derived from hydrotalcites	Solid phase	H_2/Ar	60	150–350 °C	XRD, N_2-physisorption, H_2-TPR	154
Al@Cu-based hydrotalcite CuAl-HT-c and Cu-P	Co-precipitation	NO/He	8	450–600 K	XRD, TPR and *in situ* XANES	155
		CO/He	8			

metals in zeolite catalysts differs considerably from other metal oxide catalysts. One major advantage associated with zeolite catalysts is that the higher oxygen concentration shows a very small inhibitory effect on their catalytic efficiency, but one disadvantage associated with Rh-exchanged zeolites is their extreme sensitivity to water.[60]

Transition metal ions in zeolites, supported on oxides, or dispersed in solid solutions, are very active for N_2O decomposition.[157,158] Numerous zeolites with transition metal ions are extensively studied in heterogeneous catalysis. A zeolite's ion-exchange capacity (IEC) depends on how it is chemically composed. A higher IEC is perceived in the zeolites having low SiO_2/Al_2O_3 ratios. Specific ion-exchange capacity of a zeolite varies by varying the structure of zeolites and cations exchanged. When a wet ion exchange (WIE) method was used for the preparation of Fe–ZSM-5, Lobree *et al.* were able to achieve only half of the complete IEC without getting small iron oxide particles.[159]

Natural zeolites show low activity for the catalytic reduction of N_2O using NH_3 due to the complex structures of zeolites.[160] However, when natural zeolites were modified with Fe, their activity in the SCR of N_2O became comparable to synthetic zeolites. It was found that the highest activity of N_2O decomposition was achieved when natural zeolites contained 6.5 wt% Fe.

Natural zeolites prepared with $FeCl_2$ as the precursor exhibited higher activity for the reduction of N_2O due to the formation of more reducible Fe species with $FeCl_2$.[160] Zeolites prepared with $FeSO_4$ as the precursor showed a considerably lower activity for the decomposition of N_2O as surface sulphate ions were identified as inhibitors, and their presence shifted the reaction temperature to higher values. It is suggested that natural zeolites, especially when modified with Fe, can serve as a cost-effective alternative for catalysing the SCR of N_2O, as they demonstrated comparable activity to synthetic zeolites.[161,162]

Most active catalysts for N_2O decomposition are usually inhibited by NO. This suggests that NO can interfere with the process of breaking down N_2O into less harmful components. However, interestingly enough, NO can significantly enhance the rate of N_2O decomposition over a specific catalyst, Fe–ZSM-5. Pérez-Ramírez *et al.* were first to report this positive effect of NO on N_2O decomposition over Fe–ZSM-5. They proposed a mechanism where NO in the gas phase combines with both N_2O and adsorbed O_2, leading to the regeneration of active sites and the production of nitrogen oxide. This mechanism explains the increase in the N_2O decomposition rate due to NO.[61] However, Li and Armor reported that zeolites exchanged with Co or Cu ions were effective catalysts for N_2O decomposition, and that metal ions (particularly Co, Cu, and Fe) in ZSM-5 were far more active than the same ions on Al_2O_3.[163] On Cu–ZSM-5, Fe–ZSM-5 and Co–ZSM-5, the N_2O decomposition rate was proportional to the exchange extent. The existence of excess O_2 left the catalytic activity of Co–ZSM-5 unchanged and slightly decreased Cu–ZSM-5 activity, but enhanced the catalytic activity of Fe–ZSM-5.[164] Conversely, H_2O present in the feed strongly affected the catalytic activity of zeolites and led to irreversible deactivation because of its heterolytic adsorption on active sites. In the presence of water vapours, Co–ZSM-5 was more

stable than Cu–ZSM-5 and Fe–ZSM-5.[165] For the decomposition of N_2O into its elements, TMI-exchanged pentasil-zeolites are recognized as most appropriate catalysts. Among the samples investigated, the highest N_2O decomposition activity was displayed by Cu–ZSM-5 catalysts.[166] Therefore, Deka *et al.* have carried out an extensive investigation on the use of Cu-exchanged zeolite-based catalysts (that include zeolite Y, ZSM-5, SSZ-13 and zeolite beta) for the abatement of NO_x present in the exhaust emissions of light and heavy-duty vehicle engines.[11] However, Cu–ZSM-5 has a tendency to lose activity in the presence of H_2O vapours limiting its use in practical applications. However, Fe-containing zeolites are less sensitive towards H_2O vapours in comparison to Cu-containing zeolite.[167] Liu *et al.* studied N_2O formation using Cu–SSZ-13 zeolites *via* the NH_3-asssited SCR of NO_x. All reactions were performed in a flow reactor system, as shown in Fig. 10. It was found out that N_2O formation occurred through two entirely different mechanisms at low and high temperatures. At low temperatures, N_2O was released due to the decomposition of NH_4NO_3 on Cu–SSZ-13 zeolite, while high temperatures favoured the NH_3 oxidation route for N_2O formation.[168]

Yasumura *et al.* demonstrated an efficient strategy for the dispersion of metal species to design single-atom catalysts. Chabazite (CHA) zeolite precursors were utilized as templates to disperse bulk Pd atoms into their small pores.[169] At 600 °C, the flow of feed gas was regulated in such a way that Pd atoms present on the outside of CHA zeolites can get dispersed introducing Pd(II) ions into the pores of zeolite forming Pd–CHA zeolites along with the formation of N_2O. Fig. 11a illustrates the conversion of bulk Pd and CHA zeolites into Pd(II)-intercalated zeolites.

It has been observed that adsorbed NH_3 leaves the active sites by reaction with the surface O_2. As NH_3, as a reducing agent, preferably reacts with O_2, the N_2O decomposition process becomes suppressed due to the presence of surface O_2. As a result, a vast majority of studies on the SCR of N_2O have been devoted to Fe-exchanged zeolite catalytic systems, more specifically, the Fe–BEA catalysts.[171,172] The N_2O abatement by NH_3 follows the Mars and Van Krevelen mechanism that involves an oxidation–reduction cycle of interchange between two oxidation states of Fe ($Fe^{3+} \leftrightarrow Fe^{2+}$). In this scenario, N_2O reduction into oxygen surface species occurs over some definite Fe-sites, which lead to simultaneous N_2 release. Consequently, O_2 has no inhibitory influence on N_2O decomposition through NH_3.[173] In Fig. 11b, it can be noted that the presence of O_2 does not hinder the conversion of N_2O. In fact, there was small improvement in N_2O conversion when O_2 was present. This suggested that O_2 did not negatively impact the conversion of N_2O. Fig. 11d demonstrates that the enhanced reduction of N_2O was associated with the oxidation of NH_3, which could change the NH_3/N_2O stoichiometry. In the absence of O_2, the highest N_2O conversion occurred at around 3500 ppm of NH_3 concentration. In contrast, in the excess of O_2, the highest N_2O removal occurred at around 4000 ppm of NH_3 concentration. This also suggested that O_2 did not significantly interfere with N_2O decomposition and did not efficiently react with NH_3. Fig. 11c indicates that the oxidation of NH_3 by O_2 was much less significant when N_2O was present compared to when N_2O was absent. This suggested that in the reaction system involving N_2O, NH_3 and O_2, the selective catalytic reduction (SCR) of N_2O by NH_3 was more dominant than the oxidation of NH_3 by O_2. Fig. 11e shows that when NH_3 is oxidized by O_2, it produces a large amount of NO, NO_2 and N_2O. However, in the N_2O + NH_3 + O_2 reaction system, only N_2 is detected as the main product. This indicated that NH_3 can be oxidized by both O_2 and N_2O, but N_2O is much more reactive than O_2, and their reaction pathways are distinct.[170]

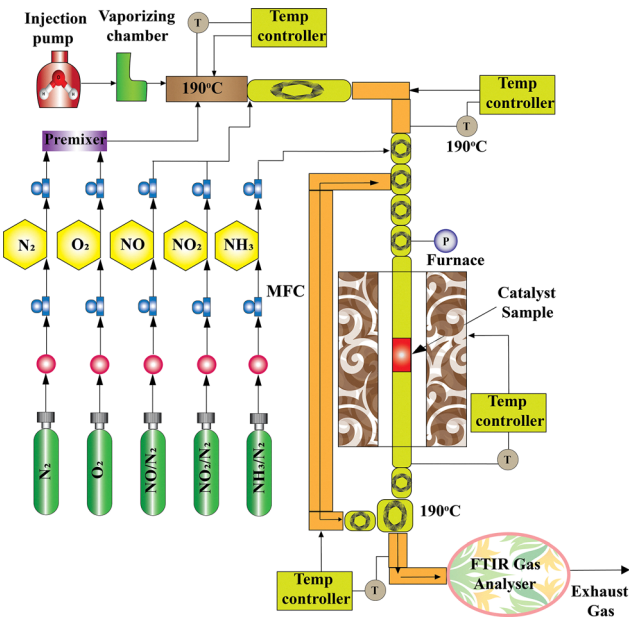

Fig. 10 Experimental setup of N_2O formation during the selective catalytic reduction of NO_x with NH_3 over Cu–SSZ-13.[168] Reproduced with permission from the American Chemical Society (Copyright©2019).

Ju *et al.* have found that UV irradiation of the Pb^{2+}–ZSM-5 catalyst led to the decomposition of N_2O at 298 K in a linear manner with the irradiation time.[174] It can be confirmed by observing the yield of N_2 that increases as a function of the UV-exposure time, while under dark conditions, the formation could not be noticed. The yield of N_2 also increases when the amount of Pb^{2+} loading becomes higher. It was reported that the photocatalytic decomposition of N_2O proceeds much more efficiently in the presence of propane.[130] In addition to the N_2 evolution, this reaction also led to the formation of oxygen-containing compounds such as ethanol and acetone. It was indicated that the efficient decomposition of N_2O proceeds photocatalytically in the presence of propane on the Pb^{2+}–ZSM-5 catalysts. The efficiency of the photocatalytic reduction of N_2O is found to be strongly dependent on the type of hydrocarbons used, *e.g.* methane or ethane, and among the hydrocarbons, the highest enhancement in the reaction rate is shown by propane. These results can be attributed to the observation that during the reaction, oxygen atoms formed by the photodecomposition of N_2O detach more easily from the isolated Pb^{2+} ions in the presence of propane.[174] Similarly, Co-based BEA zeolite catalysts were also used to study the oxidative

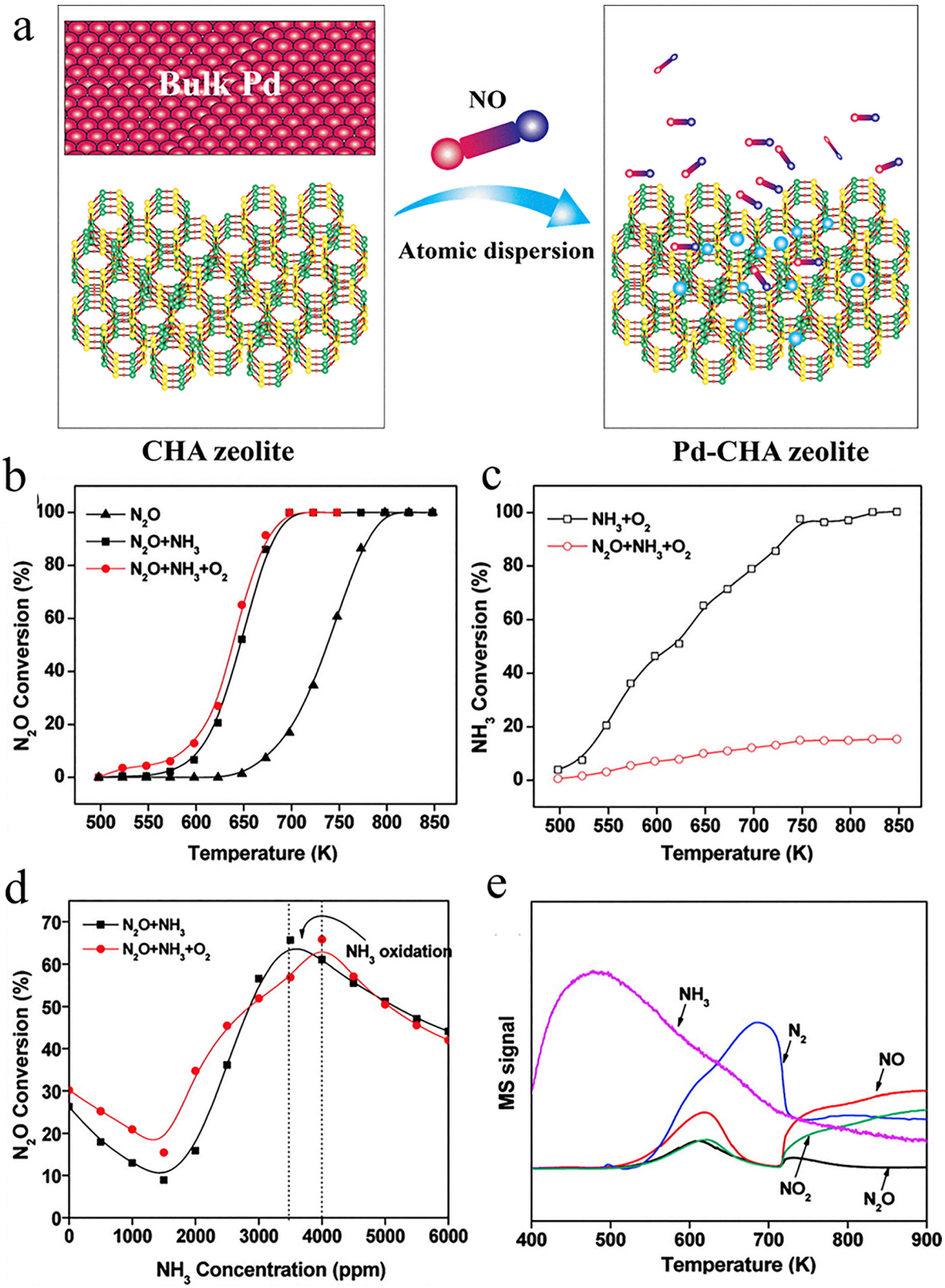

Fig. 11 (a) Transformation of bulk Pd to Pd cations in small-pore CHA zeolites facilitated by NO.[169] Reproduced with permission from the American Chemical Society (Copyright©2021). (b) Decomposition of N_2O (%) *via* selective catalytic reduction (SCR) through NH_3 on Fe-MOR catalysts. (c) Decomposition of NH_3 (%) by oxidation of NH_3 with and without N_2O. (d) Decomposition of N_2O (%) *via* NH_3 as a function of P(NH_3) with and without O_2 and e. TPSR profiles of oxidation of NH_3 (conditions: 100 mg catalyst, 0 or 4000 ppm NH_3, 0 or 5% O_2, 5000 ppm N_2O, and balance He. GHSV = 30 000 h^{-1}).[170] Reproduced with permission from the American Chemical Society (Copyright©2012).

dehydrogenation of propane (C_3H_8) with N_2O or a mixture of N_2O and oxygen (O_2) as the oxidants. N_2O is more selective but less active compared to O_2 as an oxidizing agent. Increasing the concentration of N_2O in the reaction mixture with C_3H_8 and O_2 led to a substantial increase in propane conversion while maintaining a constant selectivity for propene. The combination of O_2 and N_2O had a synergistic effect, resulting in a three-fold higher yield of propene compared using O_2 and N_2O alone.[175] Table 6 summarizes various examples of catalysts used along with the techniques applied during the course of analysis for the purpose of N_2O decomposition.

5.2.2.1. Shortcomings of zeolite catalysts. Zeolite catalysts, despite their well-defined microporous structures and strong metal–support interactions, have notable limitations in N_2O decomposition. Their narrow pore sizes can restrict the diffusion of reactants and products, especially at higher conversions. Metal ion exchange may lead to non-uniform dispersion or clustering, reducing active site accessibility. Thermal stability under prolonged high-temperature reactions can be a concern, leading to framework degradation. Additionally, zeolites are sensitive to water vapours and contaminants such as sulphur, which can cause deactivation and limit their industrial applicability.

5.2.2.2. Application scenario: diesel vehicle exhaust mechanism. These catalysts are highly effective for N_2O decomposition in diesel exhaust due to their high surface area, tunable acidity and excellent hydrothermal stability. They enable selective catalytic reduction with NH_3, offering high efficiency at medium temperatures. However, they are sensitive to sulphur poisoning, may deactivate under prolonged hydrothermal stress, and require careful formulation for durability.

5.2.3. Mixed metal oxides in mesoporous silica. After the discovery of well-organized mesoporous molecular sieves, scientific community has developed interest in their catalytic applications. Discovered by Mobil researchers, these mesoporous silica-supported catalysts possess a higher surface area than the conventional zeolite-based catalysts. Owing to their fascinating properties, these materials play an important role to support the other co-catalysts in many catalytic reactions.[204]

For example, SBA-15 is a mesoporous silica material with a fibre-like morphology that is several tens of micrometers long. It possesses a 2D porous structure and unique properties.[205,206] It has various applications including its use as a support material for Rh catalysts in N_2O abatement with Rh being one of the most active metals in N_2O decomposition. Different mesoporous silica-supported metal ions are crucial with regard to their N_2O abatement activity and age resistance, but among them Rh/SBA-15–S is found to be most active and durable. It is well known because of its superior performance in the presence of O_2 which is typically an inhibiting agent. This is attributed to the large pore size of Rh/SBA-15–S that enhances catalyst's access, diffusion and dispersion. The smaller particle size of Rh in Rh/SBA-15–S results in the higher dispersion of metals on the catalyst surface. It favours the formation of more Rh^+ ions than Rh^0 or Rh^{3+}, which, in turn, leads to higher N_2O decomposition activity. Rh/SBA-15–S is found to be durable, maintaining its performance at a temperature of 430 °C. This suggests its suitability as a support material in long-term applications and further research.[207] Similarly, Wei *et al.* reported the synthesis of a highly dispersed and well-homogenized bimetallic Au–Pd alloy supported on amine-functionalized SBA-15. The catalytic activities, when tested from 150 °C to 600 °C, revealed a decreasing trend with the increase in the percentage of Au in bimetallic alloy catalysts (Fig. 12a). It led to the conclusion that the addition of Au negatively affects the activity of Pd catalysts. Though on the one hand, the Au–Pd alloy facilitates the desorption of O_2 molecules, on the other hand, it affects other elementary steps that change the rate-determining step. Fig. 12b depicts the energy profiles of N_2O degradation over Pd, Pd_3Au/Pd and $PdAu_3$/Pd catalyst's surface, which has been split into three processes, *i.e.* (a) decomposition of N_2O into N_2 and O atoms, (b) diffusion of O atoms on the surface of catalysts and (c) recombination of two O atoms to form O_2. The respective mechanisms of degradation are shown in Fig. 12c–k.[208] Various other examples of such catalysts are summarized in Table 7.

5.2.3.1. Shortcomings of mesoporous silica-supported metal oxide catalysts. Mesoporous silica-supported metal oxide catalysts often suffer from weak metal-support interactions, leading to metal sintering or leaching under harsh conditions. Their thermal and hydrothermal stability is generally lower than that of crystalline supports like zeolites. Additionally, achieving uniform metal dispersion can be a challenge, and their catalytic activity may decline over time due to the structural degradation or active site deactivation.

5.2.3.2. Application scenario: chemical plant emissions. Mixed metal oxides dispersed in mesoporous silica supports provide high surface area, uniform metal dispersion and enhanced redox properties, making them effective for N_2O decomposition in chemical plant emissions. They offer thermal stability and tenability, but disadvantages include susceptibility to pore blockage, reduced activity under humid or sulphur-rich conditions, and higher synthesis complexity.

5.3. Nanostructured metal-doped materials

Nanostructured metal-doped materials exhibit high surface area, quantum size effects, and unique electronic properties. Doping enhances the catalytic activity by modifying charge distribution and creating active sites. Their tunable morphology – nanosheets, nanotubes or cages – improves reactant accessibility. These materials often show superior thermal stability, reactivity, and selectivity, making them promising candidates for advanced catalytic applications like N_2O decomposition.

5.3.1. Metal-doped nanotubes, nanosheets and nanocages. Nanotubes, nanosheets and nanocages are elongated, 2D and cage-like structures, respectively, possessing large surface area, crystallinity, high porosity, hollow structure and astonishing electrical and mechanical properties, rendering them novel and excellent choice of catalyst for N_2O decomposition due to a

Table 6 Overview of synthesis methods, reaction conditions and various techniques employed during the course of analysis of different zeolite catalysts for N_2O decomposition

Catalysts	Preparation method	Reaction atmosphere	Air speed (mL min^{-1})	Decomposition temp-range (°C K^{-1})	Techniques used for characterization and activity of catalysts	Ref.
Co–, Cu– and Fe–SSZ-13 zeolites	Hydrothermal	N_2 H_2/Ar	10 30	300–530 K	XRD, FT-IR, H_2-TPR, N_2O-TPR	27
Rh–ZSM catalysts	Incipient wetness	He/Ar	70	250–450 °C	STEM, XPS, TPR, N_2O-DRIFTS	104
CoMnAl HTC catalysts	Co-precipitation	He	25	330–460 °C	SEM, EDX, XRD, NH_3-TPD, CO_2-TPD, H_2-TPR, BET	157
Cu–ZSM-5 catalysts	Ion exchange	NH_3/He	30	200–600 °C	BET, XRD, TEM, CO_2-TPR, NH_3-TPR, GC–TCD	176
Fe–ZSM-5	Hydrothermal	He/Ar	15	550–750 K	N_2O-TPD, O_2-TPD, NO–TPD, AAS	177
Co–ZSM-5	Hydrothermal	He/O_2	25	380–500 °C	SEM, XRD, NH_3-TPD, H_2-TPR, ICP–AES, UV-Vis-DRS, DFT	178
Co/zeolites (Co/Beta, Co/mordenite, Co/ZSM-5, Co/MCM-49, Co/ZSM-23, Co/SSZ-13)	Wet impregnation	N_2	30	200–450 °C	XRD, BET, NH_3-TPD, H_2-TPR, XPS UV-Vis-DRS,	179
Fe–, Co–, Ni– and Cu–ZSM-5 catalysts	Ion exchange	Ar	4	400–800 °C	DFT, TPR	158
Fe, Co and Ni-exchanged Na-MOR catalysts (Fe-MOR, Co-MOR and Ni-MOR catalysts)	Ion exchange	O_2/He	100	293–773 K	GC, TCD, FID, *operando* FTIR equipped with MCT detector	180
Cu/ZSM-5 catalysts	Adsorption	N_2	40	250–500 °C	ICP–AES, UV-Vis-DRS, H_2-TPR, N_2O-TPD	181
Cu–ZSM-5 catalysts	Adsorption	—	—	—	DFT	182
Fe-zeolites (Fe–PST-7, Fe–LTA, Fe–RTH, Fe–SSZ-13, Fe–FER, Fe–ZSM-5)	Hydrothermal	He	55	600–850 °C	XRD, SEM, TEM, BET, UV-vis, ESR, FTIR, NMR	183
Cu–ZSM-5 catalysts	Hydrothermal	—	—	600–800 K	H_2-TPR, IR	184
Cu–ZSM-5 catalysts	Ion exchange	N_2O/N_2	300	350–450 °C	H_2-TPR, IR, BET, H_2-TPR, TPD, FESEM, EDX	151
Cu–, Ni–, Zn–, Co–, Fe– and Mn–ZSM-5 catalysts	Ion exchange	N_2	300	50–300 °C	DFT, N_2O-TPD, GC–TCD, FT-IR, BET, ICP–OES	185
Fe–ZSM-5 catalysts	Wet impregnation	N_2	30	250–550 °C	XRD, XPS, BET, HRTEM, UV-Vis-DRS, XPS, H_2-TPR, TPO, DRIFTS	186
Cu/HZSM-5 catalysts	Wet impregnation	N_2	60	620 K	FTIR, XPS, XPRD	187
Co/HZSM-5 catalysts	Citric acid impregnation	O_2/Ar	80	300–450 °C	XRD, TG–DSC, Raman, SEM, H_2-TPR, XPS, EPR, FTIR, DRIFTS	188
Fe–ZSM-5 catalysts	Hydrothermal	N_2	20	300–600 °C	XRD, SEM, BET, UV-vis, FTIR	189
Fe–ZSM-5, Fe-Beta, Fe–FER catalysts	Wet impregnation	He	70	200–400 °C	FTIR, BET, H_2-TPR, TGA–MS	190
Fe-beta, Fe–ZSM-5 and Fe–SAPO-34 catalysts	Ion exchange	H_2/Ar	30	200–400 °C	UV-vis-DRS, H_2-TPR	191
Fe–SSZ-13 catalysts	Ion exchange	He	103	400–600 °C	ICP–AES, BET, UV-vis-DRS, XRD, TEM, On-line GC–TCD	192
Fe/CHA catalysts	Ion exchange	N_2	80	160–550 °C	XRD, ICP–OES, DFT, TEM, EDX, XPS, EPR, FTIR, H_2-TPR	193
Fe-modified MCM-22 zeolite and its derivative ITQ-2 catalysts	Ion exchange	Ar	10	200–600 °C	XRD, ICP–OES, UV-vis-DRS, H_2-TPR, HRTEM	161
(Co, Fe)–ZSM-5 and (Co, Fe)-beta catalysts	Ion exchange	Ar	30	25–600 °C	XRD, H_2-TPR, UV-vis, TCD	165
Cu/SSZ-13, Cu/SSZ-5, Cu/BEA	Ion exchange	O_2	2	100–500 °C	XRD, BET, DRIFTS, FTIR, H_2-TPR, NH_3-TPD	194
Co(x)/PRSA catalysts	Impregnation	O_2	20	348–438 °C	XRD, BET, H_2-TPR, NH_3-TPD, XPS, XRF, DRIFTS	195
Fe-FER catalysts	impregnation	NO/O_2/H_2O	350	200–900 °C	XRD, BET, SEM, UV-vis-NIR, FTIR, Mössbauer spectroscopy	196
Fe zeolite catalysts	Diffusion impregnation	He	20	—	UV-Vis-NIR, FTIR, Mössbauer spectroscopy	197
Zeolite 5A, 13X and ZSM-5 catalysts	Wet impregnation	N_2	300	298–358 K	N_2O-TPD, BET, isosteric heat of adsorption	198
Cu/SSZ-13 catalysts	Hydrothermal	NO/NH_3/CO_2/H_2O/NO_2/N_2O	800–1500	200–600 °C	XRD, BET, ICP–OES, UV-Vis-DRS, H_2-TPR, HRTEM	199
Fe/BEA	Ion exchange	N_2	300	350–380 °C	XRF	200
Fe-MOR and Fe-FER	Hydrothermal	O_2/He	100	0–350 °C	FTIR, UV-vis	201
Fe–FER	Hydrothermal	—	—	500–900 °C	XRD, SEM, FTIR	202
Zeolite-based Fe catalysts	Ion exchange	NO/O_2/H_2O/He	350	400–800 °C	XRD, FTIR, TPD	203

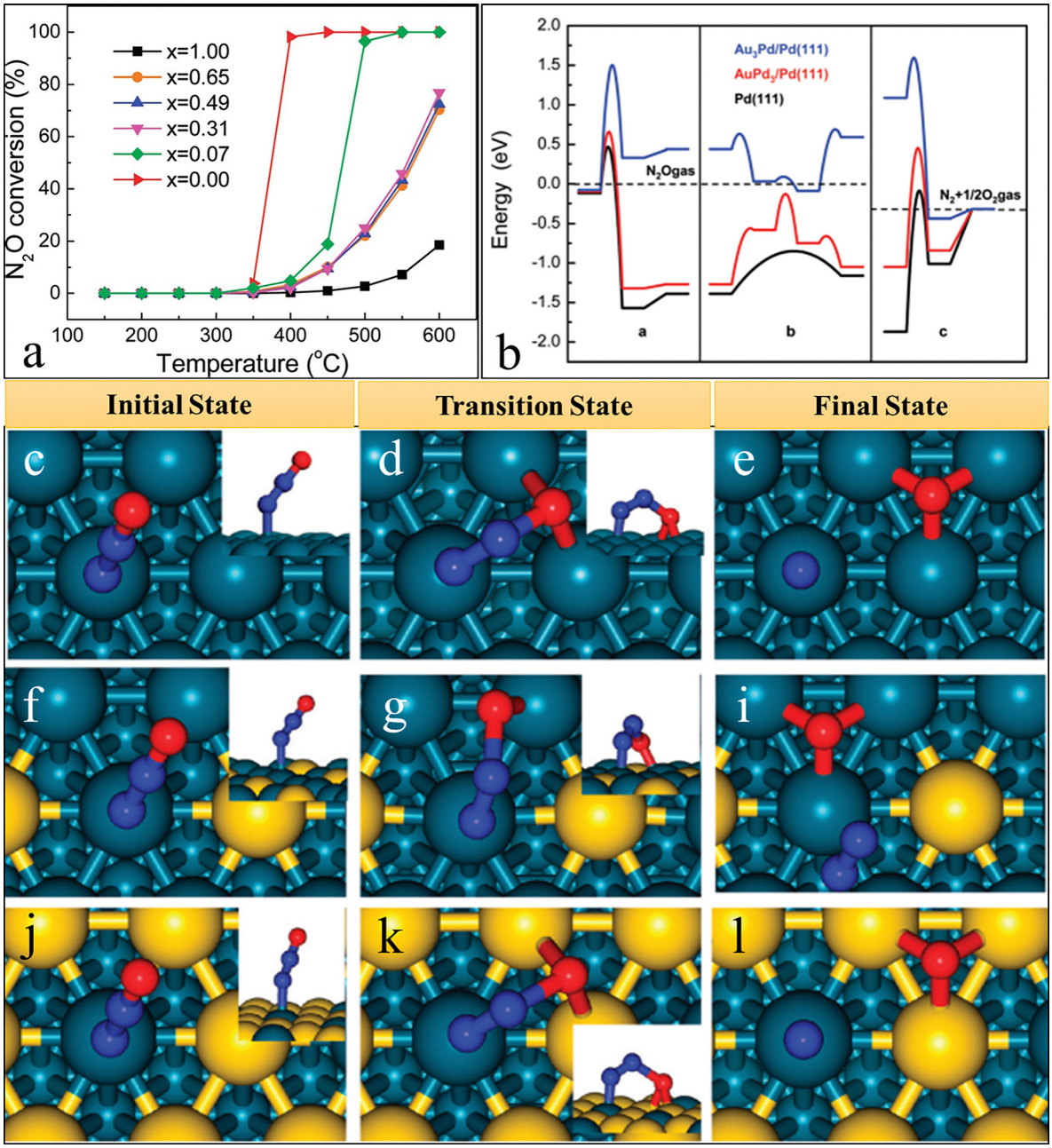

Fig. 12 (a) N_2O conversion (%) as a function of reaction temperature onto Au_xPd_{1-x}/SBA-15 catalysts (where x = atomic ratio of Au to total metal atoms; metal loading = 2 wt%). (b) Energy profiles for N_2O decomposition on Pd, $AuPd_3$ and Au_3Pd catalysts. (c)–(k) Mechanism of N_2O degradation into N_2 and O_2 over (c)–(e) Pd, (f)–(h) Pd_3Au/Pd and (i)–(k) $PdAu_3$/Pd catalysts.[209] Reproduced with permission from the American Chemical Society (Copyright©2012).

shorter diffusion length and easier mass/heat transport.[209,216] Recently, the decomposition of N_2O supported by metal-doped nanotubes (NTs), nanosheets (NSs) and nanocages (NCs)-has emerged. Researchers have predicted the roles of metal-confined titania nanotubes,[217,218]

carbon nanotubes (CNTs),[219,220] boron nitride nanotubes, nanosheets,[221,222] and nanocages[223] for N_2O decomposition by employing DFT studies.

Metal-doped nanocages are currently among very popular materials that can capture greenhouse gases and protect the environment from their harmful effects. Gao *et al.* have successfully doped four Ca atoms in a C_{60} molecule and examined its energy profile for CO_2 capture and N_2O adsorption. In comparison, the adsorption of N_2O on pristine C_{60} molecules was very weak as compared with Ca-decorated fullerene C_{60}.[224] Fig. 13a represents the doping of Ca atoms in a C_{60} molecule, while Fig. 13b and c show the adsorption of one and two N_2O molecules on the surface of CaC_{60}, respectively. Table 8 demonstrates the examples of metal-doped nanotubes, nanosheets and nanocages utilized for N_2O mitigation studies.

Table 7 Overview of synthesis methods, reaction conditions and various techniques employed during the course of analysis of mesoporous silica-supported metal/metal oxide catalysts for N_2O decomposition

Catalysts	Method	Reaction atmosphere	Air speed (mL min^{-1})	N_2O decomposition temp-range (°C K^{-1})	Techniques used for characterization and activity of catalysts	Ref.
Al_2O_3 + SiO_2	Wet impregnation	N_2	100	300–450 °C	AAS, XRD, TPR-H_2, FTIR, Raman, XPS, SEM, N_2 adsorption	210
Pt, Pd, Rh/Al_2O_3–SiO_2	Hydrothermal	He	100	600–900 °C	XRD, N_2 physisorption and FESEM	211
Pt/SiO_2	Impregnation	Ar	10	350–600 °C	BET, XRD, ICP	212
Cu-supported on hollow silica–alumina composite	Impregnation	N_2	50	450–800 K	EDX, UV-Vis-DRS, SEM, TEM	213
Rh@S-1	Hydrothermal	—	—	200–400 °C	STEM, XPS, DRIFTS, TEM	214
NiCoAl-based monolithic catalysts	Wet impregnation	N_2	10	300–600 °C	SEM, EDX, BET	215
TiO_2@Fe_2O_3@Al_2O_3 monolith catalysts	Co-precipitation	—	—	220–420 °C	XRD, XPS	100

5.3.1.1. Shortcomings of metal-doped nanotubes, nanosheets and nanocages. Controlled synthesis of metal-confined nanotubes remains a big issue. They face challenges like structural instability at high temperatures, metal agglomeration and limited long-term durability under reaction conditions. Their synthesis can be complex and costly and scalability remains a barrier. In low-temperature zones, these catalysts suffer from serious disadvantages at the industrial level.[251]

5.3.1.2. Application scenario: power plant emissions. Metal-doped nanostructures offer exceptional surface area, abundant active sites, and tunable electronic properties, making them highly promising for N_2O decomposition in power plant emissions. They provide excellent dispersion of doped metals and improved redox performance. However, challenges include complex synthesis, potential agglomeration, limited large-scale stability, and higher costs compared to conventional catalyst systems.

5.3.2. Metal-embedded graphene and graphitic nitrides. Graphene is considered one of the most promising candidates for next-generation electronic materials of this decade.[225,252] Extensive research is carried out on graphene because of its enormous surface-to-volume ratio (*i.e.* large area) for catalytic reactions. However, modified graphene sheets display high catalytic performance for N_2O decomposition, and several DFT studies have been conducted on this catalytic behaviour, *e.g.* transition metal-embedded graphene,[253–255] N-doped graphene,[256,257] Si-doped graphene,[245,258] metal oxide-doped graphene,[255] and metal-decorated graphene oxides.[253,259] Among them, transition metal-embedded graphene structures possess good thermal stabilities and stronger bonds between metals and neighbouring C-atoms.

Like graphene, graphitic carbon nitride (g-C_3N_4) is composed of carbon and nitrogen atoms arranged in a 2D, hexagonal lattice. However, in g-C_3N_4, carbon and nitrogen atoms are bonded together in a polymeric, layered structural form. This polymeric arrangement gives it a unique set of properties compared to graphene. However, graphene is a zero-bandgap material while g-C_3N_4 is a semiconductor with moderate bandgap that makes it suitable for electronics and photocatalytic applications especially under visible light. Furthermore, its properties can be tuned by modifying its structure, composition and doping that optimize its performance for specific applications.[260–262] For example, Troppovà *et al.* modified its structure by making its nanocomposites with TiO_2 at different weight ratios. The primary focus of the study was to assess the photocatalytic activity of these TiO_2/g-C_3N_4 nanocomposites. They investigated the decomposition of N_2O under UV treatment with a wavelength (λ) of 365 nm. The results indicated that all the synthesized nanocomposites exhibited higher photocatalytic activity than the individual parent materials (g-C_3N_4 and TiO_2).[263] The enhanced photocatalytic activity of TiO_2/g-C_3N_4 nanocomposites was attributed to the coupling of TiO_2 with g-C_3N_4. This coupling was found to improve the separation of electron–hole pairs and expand the range of spectral light absorption. Similarly, N-doped graphene embedded with single transition metal atoms produces single-atom catalysts (SACs), and enable the conversion of CH_4 into

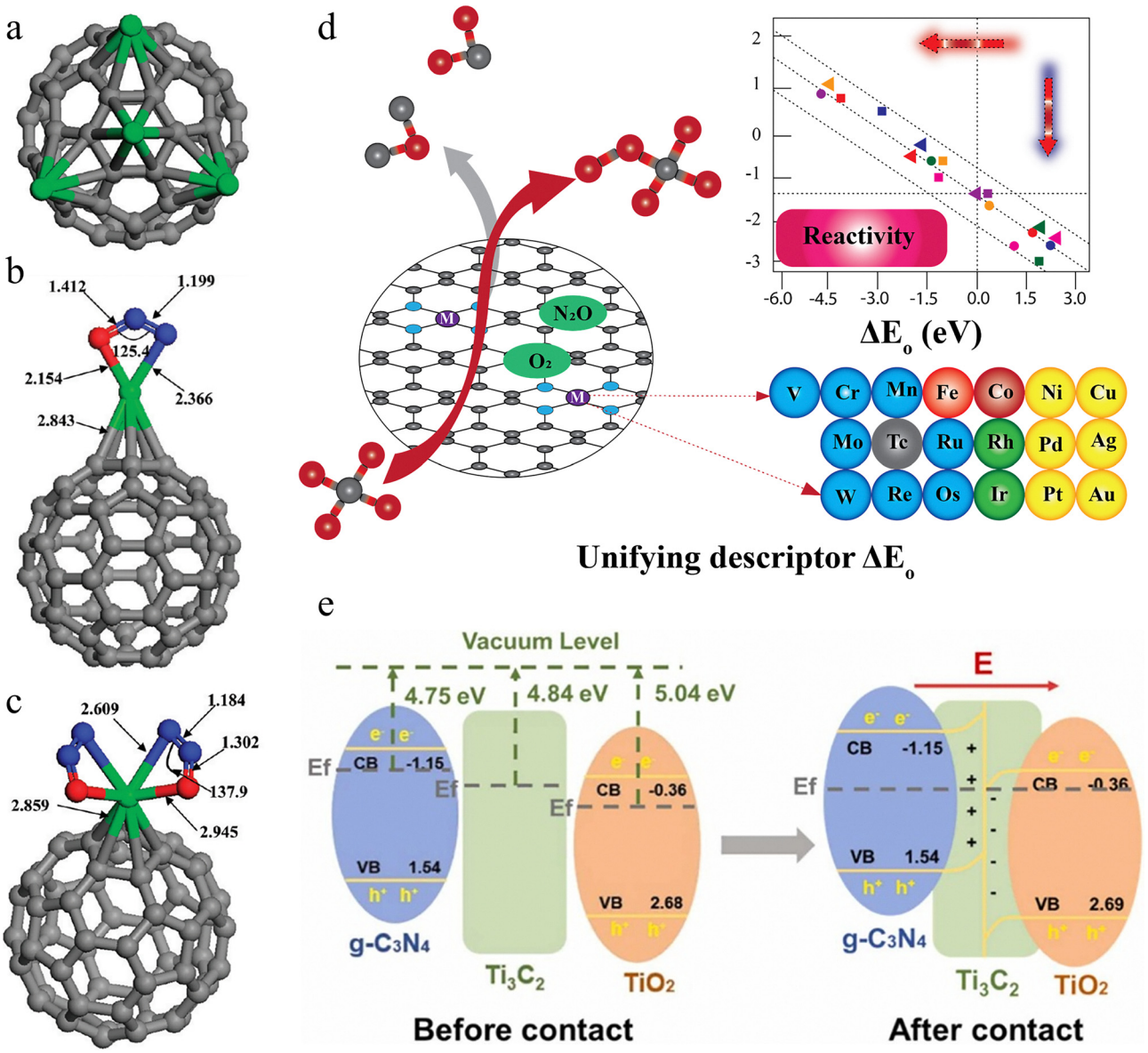

Fig. 13 (a) Four Ca atoms doped C_{60} nanocage; adsorption profiles and corresponding energies of (b) one and (c) two N_2O molecules on fullerene (CaC_{60}).[225] Reproduced with permission from the American Chemical Society (Copyright©2011); (d) mechanism of methane-to-methanol conversion by transition-metal-atom-embedded N-doped graphene (TM–N_4/C) catalysts with N_2O and O_2 oxidants and a comparison of their reactivity.[226] Reproduced with permission from the American Chemical Society (Copyright©2023). (e) Energy bands of TiO_2/MXene/g-C_3N_4 displaying energy bending.[227] Reproduced with permission form Elsevier (Copyright©2023).

CH_3OH with the help of N_2O and O_2 oxidants (Fig. 13d). The relationship between the adsorption energy of oxygen molecules (ΔE_{Ads}) and the catalytic reactivity in the conversion of methane to methanol can be seen in the inset.[264] Many other examples of use of such catalysts in N_2O abatement are provided in Table 9.

5.3.2.1. Shortcomings of metal-embedded graphene and graphitic oxides/nitrides. Major disadvantages associated with these types of catalysts are their low surface area and a rapid recombination between photoexcited electrons and holes. However, this problem is overcome by impregnation or doping of a noble metal or co-catalyst into these semiconductor materials.[226,280]

5.3.2.2. Application scenario: industrial flue gas treatment. Metal-embedded graphene and graphitic oxides/nitrides provide high conductivity, large surface area, and strong metal-support interactions, enhancing N_2O decomposition in industrial flue gas treatment. They enable efficient electron transfer and dispersion of active sites. However, their disadvantages include high synthesis costs, sensitivity to oxidation at elevated temperatures, and scalability issues for long-term industrial deployment.

5.3.3. MXene-based materials. MXene-based catalysts have emerged as promising materials for N_2O decomposition due to their unique 2D structure, high electrical conductivity and

Table 8 Overview of synthesis methods, reaction conditions and various techniques employed during the course of analysis of metal-doped nanotubes, nanosheets and nanocages for N_2O decomposition

Catalysts	Method	Reaction atmosphere	Air speed (mL min^{-1})	N_2O decomposition temp-range (°C K^{-1})	Techniques used for characterization and activity of catalysts	Ref.
Metal oxide-confined interweaved TiO_2 nanotubes M/TNT (M = Mn, Cu, Ce, Fe, V, Cr and Co)	Wet impregnation	—	—	100–300 °C	BET, HRTEM, XRD, XPS, H_2-TPR, NH_3–TPD	228
C-doped BN nanotubes (C-BNNTs)	Adsorption	—	—	—	DFT calculations for N_2O adsorption and reduction reaction	229
C-doped BN nanosheets	Adsorption	—	—	—	DFT calculations, computational calculations	222
Si-doped C_3N (Si–C_3N) nanosheets	Adsorption	—	—	—	First-principle (DFT) calculations	230
Fullerene-like boron nitride nanocages (C-doped $B_{12}N_{12}$)	Adsorption	—	—	—	DFT calculation of adsorption behaviors of N_2O and CO	231
Boron-doped C_3N monolayers	Adsorption	—	—	—	DFT	232
$A_{0.5}Co_{2.5}O_4$ (A = Mg, Ca, Sr, Ba)	Hydrothermal	O_2/N_2	80	—	DFT	233
Fe-embedded C_2N monolayer	—	—	—	—	DFT	234
SACs supported on defective boron nitride nanotubes (BNNT)	—	—	—	—	DFT	235
Potassium promoted $Gd_{0.06}Co$ catalysts	Co-precipitation	Ar	50	150–500 °C	XPS, H_2-TPR, O_2–TPD, XRD, SEM, TEM	236
Gd to Co_3O_4	Co-precipitation	N_2	350	—	DFT	237
Ni–Co mixed oxides ($Ni_xCo_{1-x}Co_2O_4$)	—	—	—	250–600 °C	SEM, EDX, XRD,	238
CuO–Co_3O_4	Co-precipitation	NH_3/O_2/He	100	400–700 °C	XAFS, DRIFTS, DFT, XANES	239
Si (Si-doped haeck-BNNT)	Adsorption	O_2	550	—	DFT	240
MgO(100) in SO_2 and CO	Adsorption	—	—	—	DFT	241
Rh(0.2)/NC–MnFe	Adsorption	H_2	60	100–150 °C	XRD	242
MC_{23} clusters (M = Ru, Mn, V, Rh, and Pd) clusters	—	—	—	—	DFT	243
Al- or P-doped hexagonal boron nitride nanosheets (h-BNNS)	Adsorption	—	—	—	DFT	244
Si@BN-yne	—	—	—	—	DFT, PDOS	245
Co-doped Fe–Mn@CNTs	Co-precipitation	—	—	170–250 °C	XRD, XPS	246
$Sm_{0.06}Ni$	Adsorption	Ar	50	100–600 °C	SEM, TEM, XRD, XPS, HRTEM	247
Co_3O_4@$CoMn_2O_4$	Hydrothermal	$NH_3/O_2/SO_2/H_2O$/Ar	300	90–270 °C	SEM, TEM, HRTEM, XPS, DRIFTS	248
M_{13}@Cu_{42} (M = Cu, Co, Ni, Zn, Ru, Rh, Pd, Pt) core–shell clusters	Adsorption	—	—	—	DFT	249
Si@$C_{24}N_{24}$	—	—	—	—	DFT	250

Table 9 Overview of synthesis methods, reaction conditions and various techniques employed during the course of analysis of metal-embedded graphene, graphitic oxides and nitrides for N_2O decomposition

Catalysts	Method	Reaction atmosphere	Air speed (mL min^{-1})	N_2O decomposition temp-range (°C K^{-1})	Techniques used for characterization and activity of catalysts	Ref.
BC_mN_n-doped graphene sheets	Adsorption	—	—	—	DFT calculations, Computational studies on adsorption configurations, electronic structures, and catalytic activity by quantum chemical calculations	257
Single Si or P atom incorporated N-doped graphene(SiN_4-Gr/PN_4-Gr)	—	—	—	—	Comparative DFT study, computational calculations for adsorption energies and reduction mechanism by first-principle	265
Single Ge or Ga atom-doped graphene	Adsorption	—	—	—	DFT study, computational estimation of adsorption energies and reaction mechanisms	266
ZnO-doped graphene [ZnO(001)@G]	—	—	—	—	DFT calculation for adsorption and activation energies, *ab initio* model, OAT, ER and LH pathway	267
Al- and Ti-doped graphene (Al-/Ti-graphene)	—	—	—	—	DFT calculations for reaction barriers and thermodynamic parameters	268
M-decorated graphene oxide (M = Mg, Cu or Ag)	Adsorption	—	—	—	DFT computational method	259
Graphitic carbon nitride (g-C_3N_4)	Melamine condensation	N_2	15	400–700 °C	UV-Vis-DRS, PL, FTIR, Raman, SSA, XRD, SEM, TEM	269
TiO_2/g-C_3N_4 photocatalysts	Adsorption	N_2	30	—	XRPD, UV-Vis-DRS, Raman, FTIR, SEM, TEM, BET, PL, XPS, GC-BID	270
TiO_2/g-C_3N_4 photocatalysts	Hydrothermal	O_2	3.5–4.5	—	N_2-physisorption, XRD, UV-Vis-DRS, FTIR, Raman, PL, TEM, XPS	263
g-C_3N_4/WO_3 photocatalysts	Calcination	—	—	—	XRD, XPS, HR–TEM, STEM, N_2-adsorption, UV-Vis-DRS, PL, EDS	271
g-C_3N_4/ZnO nanocomposite photocatalysts	Co-precipitation	—	—	—	XRD, UV-Vis, FTIR, Raman Spectroscopy, TEM and AAS	272
g-C_3N_4/$BiVO_4$ composite photocatalysts	Sol–gel	N_2	500	—	XRD, N_2-physisorption, UV-Vis-DRS, PL, FTIR, XPS, TEM	273
$BiVO_4$/g-C_3N_4 (1 : 1) composite photocatalysts	Adsorption	—	—	—	XPS, UV-Vis-DRS, PL, FTIR, Raman, BET, TEM	274
g-C_3N_4 and $BiOIO_3$	Hydrothermal	—	—	300–800 °C	FTIR, XRPD, XPS, HRTEM, DRS, TEM	275
SiN_4G	—	—	—	—	DFT	276
Cu-Embedded Graphene	Adsorption	—	—	—	DFT	253
Si@Graphene	Adsorption		—	100–350 °C	DFT	258
Au/C_2N and Cu/C_2N	Adsorption	—	—	—	DFT	277
Si-doped C_3N (Si–C_3N) nanosheets	Co-adsorption	—	—	—	DFT	278
Co_3O_4/g-CN	Wet impregnation	N_2	5	100–700 °C	XRD, HR–TEM, N_2-physisorption, Raman, FT-IR, XPS, H_2-TPR, CO_2-TPD, EC	279

Table 10 Overview of synthesis methods, reaction conditions and various techniques employed during the course of analysis of MXene-based catalysts for N_2O decomposition

Catalysts	Method	Reaction atmosphere	Air speed (mL min^{-1})	N_2O decomposition temp-range (°C K^{-1})	Techniques used for characterization and activity of catalysts	Ref.
UO_2@MXnene (*e.g.* Ti_2CO_2, V_2CO_2, Cr_2CO_2, Zr_2CO_2, Nb_2CO_2, Mo_2CO_2)	—	—	—	—	*ab initio* calculations	283
Y-doped Ti_2CO_2 (MXene) monolayer	—	—	—	—	DFT and *ab initio* calculations	284
P@Cr_2CO_2 and P@$MoCO_2$	—	—	—	—	DFT	285
g-C_3N_4/TiO_2/Ti_3C_2 MXene	Air oxidation and ultrasonic processing	O_2	3000	—	XRD, SEM, TEM, HRTEM, EDS, XPS, PL, BET, EPR	286
TiO_2–N–$Ti_3C_2T_x$	Co-precipitation	—	—	—	TEM, SEM, FTIR, Raman, XPS, PL, EPR	287
(Ti,C)-BiOBr/$Ti_3C_2T_x$	Solvothermal	N_2	200	—	XRD, FESEM, STEM, DRS, XPS, BET, Raman	288
Ti_3C_2–OH with TiO_2	Co-precipitation	N_2	—	—	SEM, TEM, XRD, XPS	289
Cu/$Ti_3C_2O_2$-V_0 and Ni/$Ti_3C_2O_2$–Ti_1	—	—	—	—	DFT	290

tunable surface chemistry. Doping transition metals (*e.g.* Fe, Co, and Cu) into MXenes enhances redox activity and introduces abundant active sites for N_2O adsorption and activation. Their layered morphology facilitates gas diffusion and charge transfer, which are critical for catalytic efficiency. However, stability under high-temperature and oxidative conditions remains a concern. Additionally, scalable synthesis and control over metal dispersion require further development. Despite these challenges, MXene-based catalysts offer a novel platform for designing efficient and selective N_2O abatement systems.[281]

As of now, there are very limited experimental studies reporting the use of MXene-based catalysts for N_2O abatement. However, a few studies have been conducted for their N_2O decomposition efficiency by mixing MXenes with other semiconductor photocatalysts. For example, Zhao *et al.* prepared triphase heterostructures *via* the self-assembly of titania, MXene and graphitic carbon nitride (TiO_2/MXene/g-C_3N_4) that showed an improved photocatalytic efficiency for NO removal. Z-scheme heterojunctions enhance photocatalysis by preserving strong redox carriers and minimizing recombination of low-activity electrons and holes, as shown in Fig. 13e.[282] Other studies on photocatalytic decomposition of NO_x using MXenes coupled with other materials are listed in Table 10.

5.4. Porous MOFs and MOF-derived catalysts

MOFs act as porous solid material catalysts possessing coordinatively unsaturated sites (CUS) for gas adsorption, separation and catalysis.[291] Their well-defined composition, hollow structures, small particle size, and exposed surface impart considerable efficiency and stability to these catalysts. MOFs are also utilized as precursors for the synthesis of metal oxides that can prevent the nanoparticle's clustering during the calcination.[227]

Metal–organic frameworks are composed of metal atoms or metal oxide clusters coordinated to organic linkers. This arrangement creates a highly ordered, porous network with a large surface area. The choice of metal and linkers can be tailored to achieve specific applications. MOFs are well known for their structural flexibility, meaning that their frameworks can be tuned or modified to suit particular needs. This flexibility allows for the design of customized surface and porous structures. Coordinative unsaturated metal sites are of particular interest, as these sites have metal atoms with unoccupied coordination, making them highly reactive. CUS can be crucial in gas adsorption and separation processes as well as catalytic reactions, which is why MOFs are excellent candidates for gas adsorption and separation due to their high surface area and tunable porosity. The tunable nature of MOFs generate catalytic sites with precise geometries, enhancing the catalytic efficiency and selectivity.[292,293] For example, nanoscale MOFs may exhibit different properties compared to their bulk counterparts, making them suitable for their specific dynamic applications.[294,295]

Despite the huge number of reports on gas sorption, the N_2O abatement studies by MOFs are still scarce. The common route of N_2O abatement is through catalytic decomposition, but adsorptive removal of N_2O by MOFs has also been reported in cases when catalytic decomposition is not economically feasible due to very low N_2O concentrations.[156] In some studies, MOFs also offer an important means for dissociative adsorption of N_2O,[296–300] as displayed in Fig. 14.

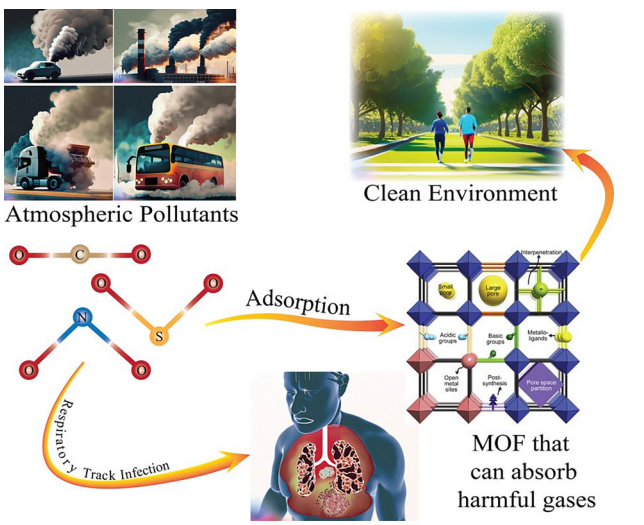

Fig. 14 Layout of the removal of atmospheric pollutants (that affect respiratory tract) *via* adsorption through MOFs.

Table 11 Overview of synthesis methods, reaction conditions and various techniques employed during the course of analysis of MOFs and MOF-derived catalysts for N_2O decomposition

Catalysts	Method	Reaction atmosphere	Air speed (mL min^{-1})	N_2O decomposition temp-range (°C K^{-1})	Techniques used for characterization and activity of catalysts	Ref.
$M_3(BTC)_2$ MOF [M = Cr, Fe, Co, Ni, Cu and Zn]	Wet impregnation	—	—	—	DFT calculations with M06-L functional, EXAFS, computational screening	302
MOF-derived Ni/CeO_2 HPOC	Wet impregnation	Ar	10	250–500 °C	SEM, TEM, N_2-adsorption, EDS, XRD, H_2-TPR, Raman, XPS, ICP–MS, GC–TCD	297
Fe-supported MOF Zr-NU-1000	Wet impregnation	—	—	—	DFT and CASPT2 calculations with M06-L functional	303
MnO_2 decorated Ru-MOF (Ru-NH_2-UiO-66/MnO_2)	Hydrothermal	—	—	Not clear	XRD, XPS, BET, SEM, TEM, N_2O–TPD, MS, EXAFS, IC, DFT	304
MFU-4l MOFs (MFU-4l, Cu^{I}-MFU-4l and Li-MFU-4l) ($BTDD^{2-}$ ligands and $[Zn_5Cl_4]^{6+}$ building units)	Wet impregnation	N_2	3	Not clear	DFT calculations, PXRD, FTIR, TGA, ICP–OES, BET	305
Fe(II)(Me_3TACN)(S_2SiMe_2)	Hydrothermal	—	—	100–135 °C	UV-vis, resonance Raman, EPR, Mössbauer, XAS, DFT	306
ZIF-67 derived Co/CoO_x@C	Hydrothermal	N_2	30	305–650 °C	TPD, DRIFTS	307
Mn@$Cu_3(BTC)_2$	Ion exchange	—	—	230–260 °C	SEM, TEM, XRD, XPS, FESEM, ZEISS-ΣIGMA HD, BET	308

Vogiatzis *et al.* conducted a computational study on high-spin Fe(IV)–OXO complexes that have well-known activating effects on the strong C–H bonds.[301] Although it is difficult to stabilize a high-spin electronic configuration for homogeneous catalysis in molecular species, the results suggested that it is attainable in MOF-based catalysts, *e.g.* Fe_2(dobdc) and its Mg-substituted analogues. Using a screening approach, different frameworks were identified that could form Fe(IV)–OXO complexes on N_2O adsorption. It was concluded from the study that among different materials, Fe–BTT selectively oxidizes C_2H_6 to C_2H_5OH by N_2O adsorption. The follow-up spectroscopic techniques suggested that the observed reactivity was attributed to the existing defect sites.[301] Further examples from the recent studies are given in Table 11.

5.4.1. Shortcomings of MOFs and MOF-derived catalysts. MOFs and MOF-derived catalysts face challenges such as limited thermal stability, structural degradation under reaction conditions, and low conductivity, which can hinder electron transfer during N_2O decomposition. Additionally, their synthesis can be complex and costly and active site accessibility may be restricted, affecting the overall catalytic efficiency.

5.4.2. Application scenario: waste gas purification. MOFs and MOF-derived catalysts offer ultra-high surface area, tunable porosity, and flexible metal-ligand coordination, making them highly effective for N_2O decomposition in waste gas purification. Their derived metal oxides or carbons show strong redox activity and stability. However, drawbacks include complex synthesis, limited hydrothermal and thermal stability and challenges in scaling up for industrial applications.

5.5. Emerging or novel materials

Antenna-reactor catalysts and quantum dot-based catalysts exhibit unique light-harvesting and charge separation abilities, crucial for N_2O decomposition. Further details are provided in the coming sections.

5.5.1. Antenna-reactor catalysts. Very recently, the concept of ''Antenna–Reactor'' plasmonic photocatalysts is introduced, and it is rapidly gaining interest in the field of catalysis. In a few studies conducted to date, N_2O decomposition was selected as a model reaction.[138,309] The use of antenna-reactor photocatalysts holds special significance in controlling the rate and products of various chemical reactions. Being poor absorbers of light, many traditional catalysts lack the ability to catalyze efficiently because of the restricted surface chemistry. By combining a catalytic nanoparticle with a plasmonic nanoantenna in a single complex, the light-harvesting properties of plasmonic nanoparticles can be fine-tuned to increase light absorption.[310] Table 12 summarizes few examples of these catalysts.

Table 12 Overview of synthesis methods, reaction conditions and various techniques employed during the course of analysis of antenna-reactor catalysts for N_2O decomposition

Catalysts	Method	Reaction atmosphere	Air speed (mL min^{-1})	N_2O decomposition temp-range (°C K^{-1})	Techniques used for characterization and activity of catalysts	Ref.
Al−Ir antenna−reactor photocatalysts	Ion exchange	—	—	250–350 °C	HAADF–STEM, MS, XPS and UV-Vis-NIR	138
Antenna-reactor plasmonic photocatalysts (Pd decorated Al NCs, Al@Cu_2O and Cu–Ru surface alloy@Cu)	Co-precipitation	—	—	—	XPS, ICP–MS, UV-Vis-DRS, TEM, HAADF, GC-MS, HR–TEM	309

5.5.2. Quantum dots. Quantum dots (QDs) can play a significant role in N_2O decomposition due to their tunable band-gaps, high surface-to-volume ratios, and excellent light absorption properties. These features enable efficient electron–hole pair generation and separation under visible light, promoting redox reactions. QDs can be engineered to provide active sites for N_2O adsorption and activation, potentially lowering the activation energy and enhancing catalytic efficiency under mild, sustainable reaction conditions.[311] Currently, there are no experimental studies specifically reporting the use of QDs for N_2O decomposition. However, theoretical investigations have predicted their potential.

6. Performance-based summary of N_2O decomposition catalysts

Performance-based comparisons are critical for identifying optimal catalysts and guiding their future research directions. Table 13 provides a comparative summary of the benchmark performance metrics for different classes of catalysts used in N_2O decomposition, based on their catalytic activity, temperature range, hydrothermal stability, and resistance to inhibitors. This provides a clear performance-based comparison of N_2O decomposition catalysts.

7. Mechanisms of N_2O decomposition

There are five primary mechanisms of N_2O decomposition in the context of fundamental steps and catalyst surface interactions. These mechanisms are key to understanding how various catalysts function in breaking down N_2O into harmless components (Fig. 15).

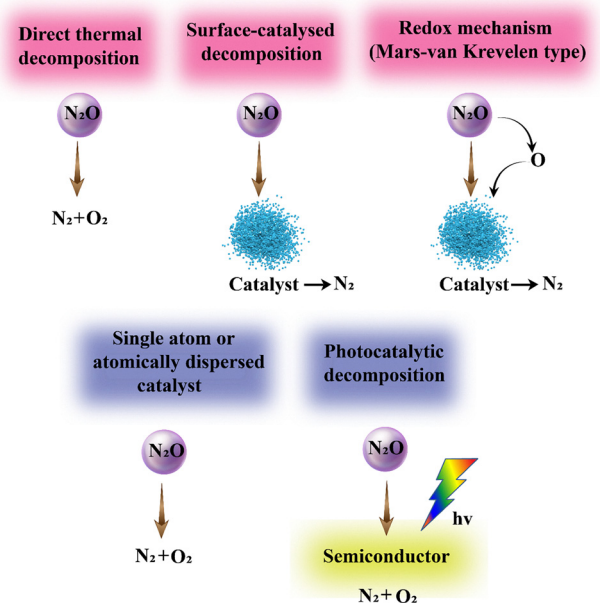

Fig. 15 Different mechanisms of N_2O decomposition.

7.1. Direct thermal decomposition $N_2O \rightarrow N_2 + \frac{1}{2} O_2$

Direct thermal decomposition of nitrous oxide occurs at temperatures above 800 °C in the absence of catalysts. Although the reaction is thermodynamically favourable, the extreme energy demand makes this route impractical for most industrial applications. However, in certain specialized high-concentration

Table 13 Comparison of the benchmark performances of N_2O decomposition catalysts

Catalyst class	Typical active sites	T_{50} [a] (°C)	Hydrothermal stability	Resistance to H_2O/O_2 [b]	Remarks
Metal oxides	CuO, Co_3O_4, MnO_2	300–500	Moderate	Low moderate	Inexpensive; deactivated by moisture
Spinel oxides	$CoFe_2O_4$, $MnFe_2O_4$	300–450	High	Moderate	Good stability; better than simple oxides
Hydroxyapatites	$Ca_{10}(PO_4)_6(OH)_2$ doped with Fe, Cu	>450	Moderate	Poor	High thermal stability; lower activity
Mixed metal oxides	Cu–Mn, Fe–Al oxides	250–400	Moderate	Low – moderate	Synergistic effects; still limited by deactivation
Hydrotalcites	Mg–Al–Fe–Cu layered structures	300–500	Moderate	Moderate	Tunable; activity depends on calcination
Zeolites	Fe, Co, Cu in ZSM-5, SSZ-13	200–400	High	High	Fe–SSZ-13 shows best performance under wet/oxidizing conditions
Mixed metal oxides in mesoporous silica	Fe/Cu in SBA-15, MCM-41	250–450	Moderate – high	Moderate	Good dispersion and surface area
Metal-doped nanotubes/ nanosheets	Fe, Co, Cu on CNTs, g-C_3N_4, BN	300–500	Moderate	Low – moderate	High surface are; expensive synthesis
Graphene and graphitic nitrides	Single atoms or clusters (Fe, Co)	250–450	Low – moderate	Low – moderate	Tunable electronic structure; prone to sintering
MXene-based materials	Ti_3C_2, Mo_2TiC_2 doped with metals	250–400	Moderate	Moderate	Emerging materials with potential for hybrid photocatalysis
MOFs and MOF-derived catalysts	Fe-MIL-100, ZIF-8-derived oxides	300–500	Low – moderate	Poor	High porosity; often thermally unstable
Antenna-reactor catalysts	Dual-site systems (*e.g.* Ce, Fe)	200–350	Moderate	Moderate – high	Emerging concept; synergistic enhancement
Quantum dots-based catalysts	CdS, Fe_3O_4 QDs supported on hosts	<300 (predicted)	Unknown	Unknown	Theoretical potential; lacks direct experimental validation

[a] T_{50} (°C): temperature at which 50% N_2O conversion is achieved. [b] Resistance to H_2O/O_2: resistance to inhibition by water vapour or oxygen.

processes such as semiconductor manufacturing, direct pyrolysis of N_2O has been investigated under nitrogen-rich atmospheres at temperatures approaching 1000 °C. These studies demonstrate that while N_2O can indeed be decomposed under such conditions, the process requires significant thermal input and careful gas-phase control, which limits its scalability for broader emission abatement. Nonetheless, this pathway remains relevant in niche applications where high-purity nitrogen or oxygen streams are simultaneously desired.[312]

7.2. Surface-catalysed decomposition

Most practical catalysts (*e.g.* Fe-, Co- and Cu-based) accelerate this reaction by activating N_2O on their surfaces. It requires active oxygen-vacancy sites. Catalysts can be used to lower the activation energy for N–O bond cleavage. Overall, it is summarized in three steps:[313,314]

1. Adsorption

$$N_2O_{(g)} \rightarrow N_2O_{(ads)}$$

2. N–O bond cleavage

$$N_2O \rightarrow N_{2(g)} + O_{(ads)}$$

3. Recombination of surface oxygen

$$O_{(ads)} + O_{(ads)} \rightarrow O_{2(g)}$$

7.3. Redox mechanism (Mars–van Krevelen type)

It is commonly observed in transition metal oxide catalysts. Here, the catalyst surface is first reduced and then deoxidized, enabling a catalytic cycle:[315,316]

1. In the first step, N_2O reacts with a lattice oxygen.

$$N_2O + [M]\text{–}O \rightarrow N_2 + [M]\text{–}O\text{–}O$$

2. Oxygen vacancy is replenished by O_2 from the gas phase.

$$[M] + \tfrac{1}{2}O_2 \rightarrow [M]\text{–}O$$

7.4. Single atom or atomically dispersed catalysis

This type of catalysis is common in Fe–ZSM-5, Fe–SSZ-13 and Cu-CHA materials. During this catalysis, first N_2O coordinates to a single metal centre. Then, the N–O bond is cleaved through electron transfer from the metal. Oxygen binds to the metal site or adjacent framework oxygen. It shows high site selectivity and stability, especially in the presence of steam or O_2.

7.5. Photocatalytic decomposition

It involves photon-excitation of catalysts such as TiO_2, g-C_3N_4 or MXene hybrids. In this case, light generates electron–hole pairs in the photocatalysts. Electrons are responsible for the reduction of N_2O to N_2. The holes may oxidize adsorbed species or water to maintain charge neutrality. This mechanism is still under development particularly for low-temperature N_2O removal.

8. N_2O activation mechanisms

N_2O activation mechanisms follow different pathways, three of which are most common, namely dual-pathway mechanism, radical-initiated oxidative decomposition and electron-assisted surface decomposition. Representative reactions belonging to each category are indicated in this section.

8.1. Dual-pathway mechanism

It corresponds to the classical surface-mediated activation of H_2O on catalytic active sites (*), described as follows:

$$N_2O + * \rightarrow N_2 + *O^-$$

$$2*O^- \rightarrow O_2 + 2*$$

$$N_2O + *O^- \rightarrow N_2 + O_2 + *$$

When NH_3 is present (NH_3-assisted SCR), surface O_2 can be removed as follows:

$$2NH_3 + 3*O^- \rightarrow N_2 + 3H_2O + 3*$$

Interaction of NH_3 with N_2O is given as

$$3N_2O + 2NH_3 \rightarrow 4N_2 + 3H_2O$$

The Fe–MOR catalyst was employed for the systematic investigation of N_2O reduction reaction mechanism by NH_3, through which the roles of different oxygen species were examined[317] (Fig. 16a).

8.2. Radical-mediated oxidation of N_2O

In this case, N_2O activation occurs *via* the following main reaction routes (Fig. 16b):

$$N_2O \rightarrow NO + N$$

$$NO + O \rightarrow NO_2$$

$$NO + OH \rightarrow HNO_2$$

$$NO_2 + OH \rightarrow HNO_3$$

8.3. Electron-mediated reduction of N_2O

The solid solution system is fairly active toward the decomposition reaction of N_2O in the temperature range of 300–450 °C. Winter proposed the mechanism of N_2O decomposition reaction involving the following steps[318] (Fig. 16c):

$$2N_2O \rightarrow N_2 + 2O_2$$

$$N_2O_{(g)} \rightarrow N_2O_{(ads)} \quad (1)$$

$$N_2O_{(ads)} + e^- \rightarrow N_2O^-{}_{(ads)}$$

$$N_2O^-{}_{(ads)} \rightarrow N_{2(ads)} + O^-{}_{(ads)}$$

$$O^-{}_{(ads)} + O^-{}_{(ads)} \rightarrow O_{2(g)} + 2e^- \quad (2)$$

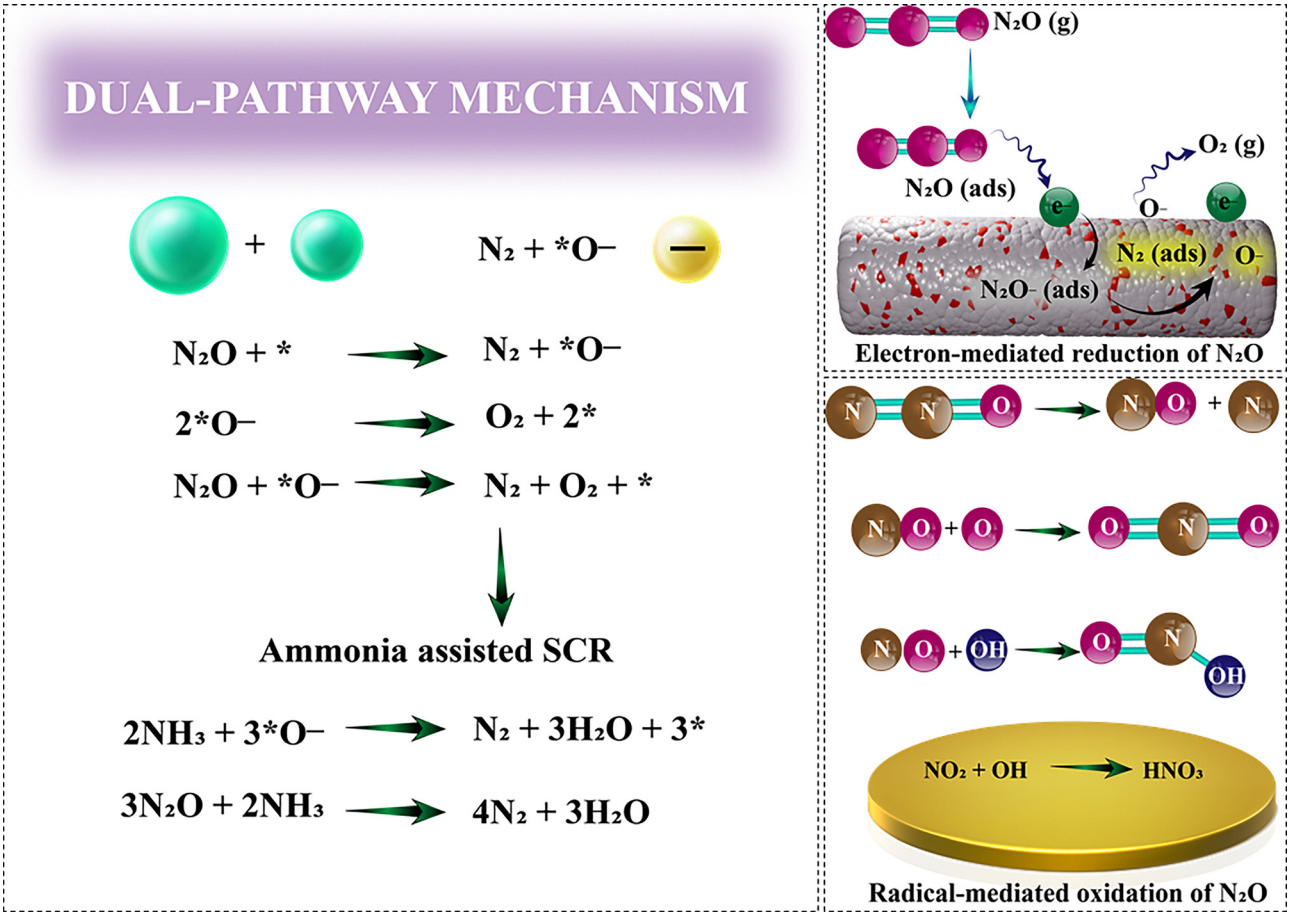

Fig. 16 Different mechanisms of N_2O activation.

$$O^- + N_2O \rightarrow O_{2(g)} + N_{2(g)} + 2e^-$$

In governing the reaction rate, N_2O adsorption [step 1] and oxygen (O_{ads}^-) desorption as O_2 [step 2] are the key steps. Using the following rate equations, the kinetic parameters of N_2O decomposition have been derived:[319]

$$\ln\left(\frac{a}{a-x}\right) = k_1 t$$

$$\left(\frac{1}{2}a\right)\ln\left(\frac{a^{1/2}+x^{1/2}}{a^{1/2}+x^{1/2}}\right) - (2x)^{1/2} = k_2 t$$

$$\ln\left(\frac{a}{a-x}\right) - b\left[\left(\frac{1}{2}a\right)\ln\left(\frac{a^{1/2}+x^{1/2}}{a^{1/2}+x^{1/2}}\right) - (2x)^{1/2}\right] = k_t 3 \quad (3)$$

Here, $\alpha = P^\circ$ N_2O (*i.e.* initial pressure of N_2O), $x = P^t$ N_2O (which represents the pressure of N_2O at time 't'), and $x/2 = P^t O_2$ (*i.e.* pressure of oxygen released at any time 't').

This rate equation corresponds to the non-inhibitory effect caused by O_2. The rate eqn (3) corresponds to strong inhibition by O_2 and represents weak inhibition of the decomposition kinetics by O_2.[320]

9. Conclusions and future perspectives

In this review, we summarized various categories of N_2O decomposition catalysts. Starting with the well-known category of TMI-exchanged zeolites, we then presented other different classes including hydrotalcites, spinel oxides, mixed metal oxides, mesoporous silica-supported metal oxides and pure metal oxides, and finally, the more recent categories of catalysts such as metal-doped nanotubes, nanosheets and nanocages, graphene and graphitic oxides/nitrides, MOFs and MOF-derived catalysts for adsorptive reduction of N_2O. Nitrous oxide (N_2O) is a potent greenhouse gas and a major contributor to stratospheric ozone depletion. Its anthropogenic and natural emissions through biological processes such as nitrification, denitrification and nitrifier denitrification along with abiotic pathways and industrial activities demand urgent and effective mitigation strategies. Catalytic decomposition of N_2O into benign products (N_2 and O_2) stands out as a promising solution owing to its direct applicability in emission abatement technologies and potential integration into existing industrial setups.

This review comprehensively categorizes N_2O decomposition catalysts based on their mechanisms, compositions and material structures, providing a unified understanding of their

functionality and efficiency. Mechanistically, the catalysts are classified into those following direct catalytic decomposition (DCD), selective catalytic reduction (SCR) and other redox or surface-catalysed processes. Composition-wise, both precious metal-based catalysts (*e.g.* Rh, Pt, and Pd) and non-precious alternatives (*e.g.* Fe, Co, and Cu-based materials) have been investigated with emphasis on cost, stability and activity trade-offs. The type of support materials – ranging from metal oxides, spinels to mesoporous and layered structures – plays a vital role in modulating dispersion, redox behaviour and oxygen vacancy dynamics.

Importantly, this review offers a progress-based classification, moving from classical oxide-based catalysts to novel nanostructured materials and framework materials such as MOFs and MOF-derived catalysts, which have shown significant promise due to their high surface areas, tunable porosity and ability to accommodate multiple active sites. Emerging materials such as antenna-reactor systems and quantum dots illustrate the frontier of N_2O decomposition research, hinting at the exciting potential of photonic and nanoscale control over activation energies.

Mechanistic pathways such as surface-catalysed decomposition, Mars–van Krevelen mechanisms, and single-atom catalysis reveal the intricate nature of N_2O activation, where lattice oxygen, metal oxidation states and coordination environments dictate the reaction rate and selectivity. Novel mechanisms including photocatalytic and electron/radical-mediated pathways further expand the toolkit available for N_2O conversion, particularly under mild conditions or light-driven environments.

Looking ahead, several key future perspectives emerge. First, the rational design of catalysts with high activity at low temperatures coupled with selectivity and durability under industrial gas compositions remains an urgent priority. The integration of computational modelling and machine learning can accelerate the discovery of optimal catalyst compositions and structures. Second, a shift towards earth-abundant, non-toxic elements is essential to scale these technologies sustainably. Single-atom catalysts and dual-function catalysts that combine decomposition with selective oxidation or reduction reactions open new frontiers in multifunctional reactor design.

Moreover, *in situ* and *operando* characterization techniques should be leveraged to elucidate real-time reaction mechanisms, bridging the gap between theoretical models and actual catalyst performance. Finally, interdisciplinary collaboration between catalysis, materials science, environmental engineering and process design is essential to translate laboratory successes into commercially viable solutions.

In summary, catalytic N_2O decomposition is a vibrant and evolving field. Continued research on catalyst development, mechanistic understanding and scalable application will be pivotal in mitigating N_2O emissions and achieving global climate and sustainability goals.

Conflicts of interest

Authors declare no competing financials interest.

Abbreviations

WHO	World Health Organization
EPA	Environmental Protection Agency
IPPC	Intergovernmental Panel on Climate Change
AFED	Arab Forum for Environment and Development
APAN	Asian Pacific Adaptation Network
CCCCC	Caribbean Community Climate Change Centre
CAN	Climate Action Network
CCL	Citizen Climate Lobby
CJA	Climate Justice Alliance
EDF	Environmental Defense Fund
HEA	Health and Environmental Alliance
NRDC	Natural Resources Defense Council
GWP	Global warming potential
AOB	Ammonia-oxidizing bacteria
AOA	Ammonia-oxidizing archaea
DCD	Direct catalytic decomposition
SCR	Selective catalytic reduction
ZSM	Zeolite Socony Mobil
SSZ	Aluminosilicate zeolite
MOF	Metal–organic framework
E_a	Activation energy
CFBC	Circulating fluidized bed combustion
SNCR	Selective non-catalytic reduction
EG	Ethylene glycol
DP	Deposition precipitation
IMP	Impregnation method
DP–Cl	Deposition precipitation by chloride precursor
PTA	Phosphotungstic acid
SACs	Single-atom catalysts
DFT	Density functional theory
GC	Gas chromatography
XRD	X-ray diffraction
XPS	X-ray photoelectron spectroscopy
FTIR	Fourier transform infrared spectroscopy
TEM	Transmission electron microscopy
HRTEM	High-resolution transmission electron microscopy
TPR	Temperature-programmed reduction
H_2–TPR	Temperature-programmed reduction with H_2
XPS	X-ray photoelectron spectroscopy
EXAFS	Extended X-ray absorption fine structure
EDS	Energy-dispersive spectroscopy
STEM	Scanning transmission electron spectroscopy
EELS	Electron energy loss spectroscopy
O_2–TPR	Temperature-programmed reduction with O_2
nHAP	Natural hydroxyapatites
SSA	Specific surface area
HADDF	High-angle annular dark field
O_2-TPD	Temperature-programmed desorption of chemisorbed O_2
XRF	X-ray fluorescence
TPSR	Temperature-programmed surface reaction

SEM	Scanning electron microscopy
FESEM	Field emission scanning electron microscopy
SAED	Selected area electron diffraction
TPCR	Transfer-PCR
QMS	Quadrupole mass spectrometer
EPR	Electron paramagnetic resonance
TGA	Thermogravimetric analysis
ICP–OES	Inductively coupled plasma-optical emission spectrometry
BET	Brunauer, Emmett and Teller theory
MS	Mass spectrometry
GC–TCD	Gas chromatograph equipped with a thermal conductivity detector
DTA	Differential thermal analysis
XRPD	X-ray powder diffraction
QDs	Quantum dots
DRS	Diffuse reflectance spectroscopy
DRIFTS	Diffuse reflectance infrared Fourier transform spectroscopy
CO-DRIFTS	Diffuse reflectance infrared Fourier transform spectroscopy of CO adsorption
MCT	Mercury cadmium telluride
LDHs	Layered double hydroxides
MP	Mirror plane
PILC	Pillared clay
VOCs	Volatile organic compounds
LS	Low saturation
SP	Sequential precipitation
TMIs	Transition metal ions
IEC	Ion exchange capacity
WEI	Wet ion exchange
XANES	X-ray absorption near-edge structure
CHA	Chabazite
AAS	Atomic absorption spectroscopy
ICP–AES	Inductive coupled plasma atomic emission spectroscopy
FID	Flame ionization detector
ESR	Electron spin resonance
NMR	Nuclear magnetic resonance
SBA	Santa Barbara Amorphous
NTs	Nanotubes
NSs	Nanosheets
NCs	Nanocages
CNTs	Carbon nanotubes
TNTs	Titania nanotubes
PL	Photoluminescence
CUS	Coordinatively unsaturated sites
BDC	1,4-Benzenedicarboxylate
BTC	1,3,5-Benzenetricarboxylate
MCM	Mobil Composition of Matter
KIT	Korea Advanced Institute of Science and Technology
MCF	Mesoporous Cellular Foam
Fe-FER	Iron Ferrierite
TG–DTA–MS	Thermogravimetric differential thermal analysis mass spectrometry

Data availability

The data and necessary protocols of this study have been included as part of the SI.

Acknowledgements

This work was financially supported and was provided access to the international journals and financial resources by the Higher Education Commission (HEC) of Pakistan (no. 377/IPFP-II) (Batch-I/) SRGP/NAHE/HEC/2020/. Dr. Ejaz Hussain thanks Govt. of Pakistan, WHO and EPA for arranging consistant seminars, conferences, debates and attention for Globle Warming.

References

1 F. Charlson, S. Ali, T. Benmarhnia, M. Pearl, A. Massazza, J. Augustinavicius and J. G. Scott, *Int. J. Environ. Res. Public Health*, 2021, **18**, 4486.
2 S. Sinhababu, Y. Lakliang and N. P. Mankad, *Dalton Trans.*, 2022, **51**, 6129–6147.
3 K. Hayashi and N. Itsubo, *Int. J. Life Cycle Assess.*, 2023, 1–13.
4 N. J. Bassous, A. C. Rodriguez, C. I. L. Leal, H. Y. Jung, C. K. Lee, S. Joo, S. Kim, C. Yun, M. G. Hahm and M. H. Ahn, *Adv. Sens. Res.*, 2023, 2300094.
5 R. Feng and X. Fang, *Environ. Sci. Technol.*, 2022, **56**, 5299–5301.
6 S. He, Y. Han and X. Qin, *J. Environ. Sci.*, 2025, **157**, 615–632.
7 B. K. Sovacool, S. Griffiths, J. Kim and M. Bazilian, *Renewable Sustainable Energy Rev.*, 2021, **141**, 110759.
8 X. Zhu, M. Burger, T. A. Doane and W. R. Horwath, *Proc. Natl. Acad. Sci. U. S. A.*, 2013, **110**, 6328–6333.
9 N. Wrage, G. L. Velthof, M. L. Van Beusichem and O. Oenema, *Soil Biol. Biochem.*, 2001, **33**, 1723–1732.
10 T. C. Robinson, D. E. Latta, L. Notini, K. E. Schilling and M. M. Scherer, *Environ. Sci.: Processes Impacts*, 2021, **23**, 1531–1541.
11 U. Deka, I. Lezcano-Gonzalez, B. M. Weckhuysen and A. M. Beale, *ACS Catal.*, 2013, **3**, 413–427.
12 Y. Zhang, G. Cao and X. Yang, *Energy Fuels*, 2021, **35**, 6443–6464.
13 Y. Liu, F. Gao, H. Yi, C. Yang, R. Zhang, Y. Zhou and X. Tang, *Environ. Sci. Pollut. Res.*, 2021, **28**, 2549–2571.
14 H. Chen, L. Zeng, D. Wang, Y. Zhou and X. Yang, *Water Res.*, 2020, **184**, 116168.
15 M. Galle, D. Agar and O. Watzenberger, *Chem. Eng. Sci.*, 2001, **56**, 1587–1595.
16 A. E. Hughes, N. Haque, S. A. Northey and S. Giddey, *Resources*, 2021, **10**, 93.
17 Q. Zhang, S. Gao and J. Yu, *Chem. Rev.*, 2022, **123**, 6039–6106.
18 N. Richards, J. H. Carter, E. Nowicka, L. A. Parker, S. Pattisson, Q. He, N. F. Dummer, S. Golunski and G. J. Hutchings, *Appl. Catal., B*, 2020, **264**, 118501.

19 S. Hinokuma, T. Iwasa, Y. Kon, T. Taketsugu and K. Sato, *Catal. Commun.*, 2021, **149**, 106208.
20 S. Hinokuma, T. Iwasa, Y. Kon, T. Taketsugu and K. Sato, *Sci. Rep.*, 2020, **10**, 21605.
21 M. Miao, M. Zhang, H. Kong, T. Zhou, X. Yang and H. Yang, *Energies*, 2021, **14**, 6148.
22 Y. Yin, R. Xiao, L. Qiu, C. Wang and H. Chang, *Fuel*, 2024, **366**, 131303.
23 Y. Li, S. Yang, H. Peng, W. Liu, Y. Mi, Z. Wang, C. Tang, D. Wu and T. An, *J. Catal.*, 2021, **395**, 195–209.
24 R. Li, Y. Li and Z. Liu, *Fuel*, 2024, **355**, 129405.
25 N. Richards, J. H. Carter, L. A. Parker, S. Pattisson, D. G. Hewes, D. J. Morgan, T. E. Davies, N. F. Dummer, S. Golunski and G. J. Hutchings, *ACS Catal.*, 2020, **10**, 5430–5442.
26 A. Szymaszek-Wawryca, P. Summa, D. Duraczyńska, U. Díaz and M. Motak, *Materials*, 2022, **15**, 7884.
27 F. Lin, T. Andana, Y. Wu, J. Szanyi, Y. Wang and F. Gao, *J. Catal.*, 2021, **401**, 70–80.
28 F. Saleem, M. Z. Abid, K. Rafiq, A. Rauf, K. Ahmad, S. Iqbal, R. Jin and E. Hussain, *Int. J. Hydrogen Energy*, 2024, **52**, 305–319.
29 N. Wajid, K. Rafiq, M. Z. Abid, A. Ilyas, T. Najam, A. Rauf and E. Hussain, *Mater. Chem. Phys.*, 2023, **306**, 128062.
30 M. Sabir, K. Rafiq, M. Z. Abid, U. Quyyum, S. S. A. Shah, M. Faizan, A. Rauf, S. Iqbal and E. Hussain, *Fuel*, 2023, **353**, 129196.
31 T. Gaidei, A. Kokorin, N. Pillet, M. Srukova, E. Khaustova, G. Shmurak and N. Yaroshenko, *Russ. J. Phys. Chem. A*, 2007, **81**, 895–900.
32 L. Han, S. Cai, M. Gao, J.-Y. Hasegawa, P. Wang, J. Zhang, L. Shi and D. Zhang, *Chem. Rev.*, 2019, **119**, 10916–10976.
33 D. Shun, D. H. Bae, J. Y. Paek and Y. S. Park, *Korean J. Chem. Eng.*, 2004, **21**, 890–894.
34 A. Ilyas, K. Rafiq, M. Z. Abid, A. Rauf and E. Hussain, *RSC Adv.*, 2023, **13**, 2379–2391.
35 M. Z. Abid, A. Ilyas, K. Rafiq, A. Rauf, M. A. Nadeem, A. Waseem and E. Hussain, *Environ. Sci.: Water Res. Technol.*, 2023, **9**, 2238–2252.
36 M. Z. Abid, K. Rafiq, A. Rauf, S. S. A. Shah, R. Jin and E. Hussain, *Nanoscale Adv.*, 2023, **5**, 3247–3259.
37 J. Liu, L. Wang, W. Song, M. Zhao, J. Liu, H. Wang, Z. Zhao, C. Xu and Z. Duan, *ACS Sustainable Chem. Eng.*, 2018, **7**, 2811–2820.
38 L.-L. Zhang, X.-M. Chen and C.-G. Liu, *Inorg. Chem.*, 2019, **58**, 5221–5229.
39 V. G. Komvokis, M. Marti, A. Delimitis, I. A. Vasalos and K. S. Triantafyllidis, *Appl. Catal., B*, 2011, **103**, 62–71.
40 P. S. S. Reddya, N. S. Babua, N. Lingaiaha, P. S. Prasada and I. Raob, *Proc. Eur. Cong. Chem. Eng.*, 2007, 1–12.
41 S. N. Basahel, M. Mokhtar, T. T. Ali and K. Narasimharao, *Catal. Today*, 2020, **348**, 166–176.
42 N. Zhang, C. He, Y. Jing, Y. Qian, T. Toyao and K.-I. Shimizu, *Surf. Interfaces*, 2024, **46**, 104120.
43 M. K. Singh and G. Rajaraman, *Inorg. Chem.*, 2019, **58**, 3175–3188.
44 M. G. Galloni, S. Campisi, A. Gervasini, S. Morandi and M. Manzoli, *Appl. Catal., A*, 2023, **655**, 119101.
45 X. Hu, L. Wu, S. Ju, C. Dong, Y. Yang and W. Qin, *Environ. Eng. Sci.*, 2014, **31**, 308–316.
46 X. Li, J. Chen, C. Lu, G. Luo and H. Yao, *Fuel*, 2021, **299**, 120910.
47 M. D. Esrafili, H. Janebi and P. Mousavian, *Appl. Surf. Sci.*, 2021, **569**, 151001.
48 H. Yu, X. Qi, X. Du, Y. Pan, X. Feng, W. Shan and Y. Xiong, *Mol. Catal.*, 2023, **537**, 112960.
49 E. M. Goliaei and N. Seriani, *Appl. Surf. Sci.*, 2022, **579**, 152215.
50 K. Feng, R. Lin, T. Chen, Y. Hu, Y. Feng, D. Chen, M. H. Tahir and T. Cao, *J. Environ. Chem. Eng.*, 2024, 111891.
51 H. Liu, S. Yang, G. Wang, H. Liu, Y. Peng, C. Sun, J. Li and J. Chen, *Environ. Sci. Technol.*, 2022, **56**, 16325–16335.
52 H. Liu, J. Chen, Y. Wang, S. Xiong, Z. Su, Y. Wang, W. Yang, X. Chu, W. Yang and Y. Peng, *Chem. Eng. J.*, 2021, **414**, 128643.
53 X. Hu, Y. Wang, R. Wu and Y. Zhao, *Mol. Catal.*, 2021, **509**, 111656.
54 W. Gao, D. Wen, J. Ho and Y. Qu, *Mater. Today Chem.*, 2019, **12**, 266–281.
55 F. Zasada, J. Gryboś, E. Budiyanto, J. Janas and Z. Sojka, *J. Catal.*, 2019, **371**, 224–235.
56 Q. Zhao, Z. Yan, C. Chen and J. Chen, *Chem. Rev.*, 2017, **117**, 10121–10211.
57 G. Chen, C. Guyon, Z. Zhang, B. Da Silva, P. Da Costa, S. Ognier, D. Bonn and M. Tatoulian, *Microfluid. Nanofluid.*, 2014, **16**, 141–148.
58 Q. Shen, L. Li, J. Li, H. Tian and Z. Hao, *J. Hazard. Mater.*, 2009, **163**, 1332–1337.
59 M.-J. Kim, S.-J. Lee, I.-S. Ryu, M.-W. Jeon, S.-H. Moon, H.-S. Roh and S. G. Jeon, *Mol. Catal.*, 2017, **442**, 202–207.
60 Y. Li, A. Sundermann, O. Gerlach, K.-B. Low, C. C. Zhang, X. Zheng, H. Zhu and S. Axnanda, *Catal. Today*, 2019, **355**, 608–619.
61 J. Pérez-Ramírez, F. Kapteijn, G. Mul and J. A. Moulijn, *J. Catal.*, 2002, **208**, 211–223.
62 X. Wei, Y. Wang, X. Li, R. Wu and Y. Zhao, *Mol. Catal.*, 2020, **491**, 111005.
63 L. Rocha-Meneses, A. Inayat, M. Ayoub, S. Ullah, S. R. Naqvi, S. Farrukh, A. Mustafa, A. Z. Abdullah and A. H. Bhat, *Environ. Prog. Sustainable Energy*, 2023, **42**, e13982.
64 S. Wojcik, P. Indyka, Z. Sojka and A. Kotarba, *Catal. Today*, 2020, **348**, 111–117.
65 G. Grzybek, P. Stelmachowski, S. Gudyka, J. Duch, K. Ćmil, A. Kotarba and Z. Sojka, *Appl. Catal., B*, 2015, **168–169**, 509–514.
66 M. Inger, J. Rajewski, M. Ruszak and M. Wilk, *Chem. Papers*, 2019, **73**, 1979–1986.
67 B. M. Abu-Zied, S. A. Soliman and S. E. Abdellah, *J. Ind. Eng. Chem.*, 2015, **21**, 814–821.
68 S. Li, J. Zhao, Z. Song, H. Wang, T. Zhang, J. Liu and Q. Jiang, *Fuel*, 2024, **362**, 130745.
69 A. Inayat, L. Rocha-Meneses, M. Ayoub, S. Ullah, A. Z. Abdullah, S. R. Naqvi and A. H. Bhat, *Environ. Sci. Pollut. Res.*, 2023, 1–12.

70 T. Franken and R. Palkovits, *Appl. Catal., B*, 2015, **176–177**, 298–305.
71 A. Klyushina, K. Pacultová, K. Karásková, K. Jirátová, M. Ritz, D. Fridrichová, A. Volodarskaja and L. Obalová, *J. Mol. Catal. A: Chem.*, 2016, **425**, 237–247.
72 H. Yu, X. Wang, X. Wu and Y. Chen, *Chem. Eng. J.*, 2018, **334**, 800–806.
73 M. Tursun, X. Wang, F. Zhang and H. Yu, *Catal. Commun.*, 2015, **65**, 1–5.
74 S. Wójcik, G. Grzybek, P. Stelmachowski, Z. Sojka and A. Kotarba, *Catalysts*, 2020, **10**, 41.
75 M. Inger, B. Moszowski, M. Ruszak, J. Rajewski and M. Wilk, *Catalysts*, 2020, **10**, 987.
76 P. Hermawan, J. Kim, M. H. Jeong, S. A. Choi, S.-M. Hwang and S. K. Jeong, *Chemosphere*, 2024, **367**, 143642.
77 A. Klegova, K. Pacultová, T. Kiška, P. Peikertová, A. Rokicińska, P. Kuśtrowski and L. Obalová, *Mol. Catal.*, 2022, **533**, 112754.
78 B. Abu-Zied, S. Soliman and S. Abdellah, *Curr. Catal.*, 2020, **9**, 152–162.
79 B. Li, X. Duan, T. Zhao, B. Niu, G. Li, Z. Zhao, Z. Yang, D. Liu, F. Zhang and J. Cheng, *Environ. Sci. Technol.*, 2024, **58**(4), 2153–2161.
80 P. Lu, L. Ye, X. Yan, X. Chen, P. Fang, D. Chen, D. Chen and C. Cen, *J. Hazard. Mater.*, 2021, **414**, 125468.
81 S. Li, Y. Li, W. Shen, Y. Bai and L. Kong, *J. Cleaner Prod.*, 2022, **380**, 134961.
82 Y. Matsumura and J. B. Moffat, *J. Catal.*, 1994, **148**, 323–333.
83 S. Sugiyama, K. Abe, H. Hayashi and J. B. Moffat, *Appl. Catal., A*, 1999, **183**, 135–142.
84 Y. Cui, H. Liu, Y. Lin and Z. Ma, *J. Taiwan Inst. Chem. Eng.*, 2016, **67**, 254–262.
85 C. Huang, Z. Ma, P. Xie, Y. Yue, W. Hua and Z. Gao, *J. Mol. Catal. A: Chem.*, 2015, **400**, 90–94.
86 M. G. Galloni, S. Campisi, A. Gervasini, S. Morandi and M. Manzoli, *Appl. Catal., A*, 2023, **655**, 119101.
87 X. Tan, H. Chen, L. Shi, Q. Lu, S. Qi, C. Yi and B. Yang, *Catal. Lett.*, 2023, **153**, 3724–3733.
88 Y. Lin, T. Meng and Z. Ma, *J. Ind. Eng. Chem.*, 2015, **28**, 138–146.
89 Y. Wang, X. Zhou, X. Wei, X. Li, R. Wu, X. Hu and Y. Zhao, *Mol. Catal.*, 2021, **501**, 111370.
90 M. G. Galloni, *Development of metal functionalized hydroxyapatite catalysts for air-quality protection*, PhD Thesis, Università degli Studi di Milano, 2022.
91 M. Galloni, S. Campisi and A. Gervasini, *Iron functionalised hydroxyapatites as efficient eco-friendly catalysts for air-quality protection*, 2020.
92 X. Liu, Y. Wang, R. Wu and Y. Zhao, *Catal. Surveys Asia*, 2021, **25**, 168–179.
93 K.-M. Lee, G. Kwon, S. Hwang, J. A. Boscoboinik and T. Kim, *Catal. Sci. Technol.*, 2021, **11**, 7850–7865.
94 D. Jia, K. Hanna, G. Mailhot and M. Brigante, *Molecules*, 2021, **26**, 5748.
95 U. Quyyum, K. Rafiq, M. Z. Abid, F. Ahmad, A. Rauf and E. Hussain, *Environ. Sci.: Water Res. Technol.*, 2023, **9**, 1147–1160.
96 M. Jalil, K. Rafiq, M. Z. Abid, A. Rauf, S. Wang, S. Iqbal and E. Hussain, *Nanoscale Adv.*, 2023, **5**, 3233–3246.
97 K. U. Sahar, K. Rafiq, M. Z. Abid, A. Rauf, U. U. Rehman, M. A. Nadeem, R. Jin and E. Hussain, *Colloids Surf., A*, 2023, **674**, 131942.
98 A. Aslam, M. Z. Abid, K. Rafiq, A. Rauf and E. Hussain, *Sci. Rep.*, 2023, **13**, 6306.
99 H. Beyer, J. Emmerich, K. Chatziapostolou and K. Koehler, *Appl. Catal., A*, 2011, **391**, 411–416.
100 L. Han, M. Gao, J.-Y. Hasegawa, S. Li, Y. Shen, H. Li, L. Shi and D. Zhang, *Environ. Sci. Technol.*, 2019, **53**, 6462–6473.
101 C. Ratanatawanate, A. Chyao and K. J. Balkus Jr, *J. Am. Chem. Soc.*, 2011, **133**, 3492–3497.
102 T. Gaidei, A. Kokorin, N. Pillet, V. Sadov, M. Strukova, S. Filatov, E. Khaustova and N. Yaroshenko, *Russ. J. Appl. Chem.*, 2010, **83**, 1130–1138.
103 S. Imamura, J.-i Tadani, Y. Saito, Y. Okamoto, H. Jindai and C. Kaito, *Appl. Catal., A*, 2000, **201**, 121–127.
104 Y. Li, A. Sundermann, O. Gerlach, K.-B. Low, C. C. Zhang, X. Zheng, H. Zhu and S. Axnanda, *Catal. Today*, 2020, **355**, 608–619.
105 T. C. Peck, G. K. Reddy, M. Jones and C. A. Roberts, *J. Phys. Chem. C*, 2017, **121**, 8435–8443.
106 M. Konsolakis, *ACS Catal.*, 2015, **5**, 6397–6421.
107 Y. Ni, Z. Han, Y. Chai, G. Wu and L. Li, *EES Catal.*, 2023, **1**, 459–494.
108 H. Xu, Y. Ma, J. Chen, W.-X. Zhang and J. Yang, *Chem. Soc. Rev.*, 2022, **51**, 2710–2758.
109 M. Zabilskiy, P. Djinović, E. Tchernychova and A. Pintar, *Appl. Catal., B*, 2016, **197**, 146–158.
110 H. Zhu, Y. Li and X. Zheng, *Appl. Catal., A*, 2019, **571**, 89–95.
111 X. Fan, S. Kang, J. Li and T. Zhu, *RSC Adv.*, 2018, **8**, 26998–27007.
112 H. Zeng and X. Pang, *Appl. Catal., B*, 1997, **13**, 113–122.
113 M. Jabłońska, M. A. Arán, A. M. Beale, K. Góra-Marek, G. Delahay, C. Petitto, K. Pacultová and R. Palkovits, *RSC Adv.*, 2019, **9**, 3979–3986.
114 S. Carabineiro, E. Papista, G. Marnellos, P. Tavares, F. Maldonado-Hódar and M. Konsolakis, *Mol. Catal.*, 2017, **436**, 78–89.
115 M. Lykaki, E. Papista, N. Kaklidis, S. A. Carabineiro and M. Konsolakis, *Catalysts*, 2019, **9**, 233.
116 K. Karásková, K. Pacultová, K. Jirátová, D. Fridrichová, M. Koštejn and L. Obalová, *Catalysts*, 2020, **10**, 1134.
117 X. Hu, Y. Wang, R. Wu, L. Zhao, X. Wei and Y. Zhao, *Appl. Surf. Sci.*, 2020, **514**, 145892.
118 T. Zhao, Y. Li, Q. Gao, Z. Liu and X. Xu, *Catal. Commun.*, 2020, **137**, 105948.
119 P. H. Ho, M. Jabłońska, M. Nocuń, G. Fornasari, F. Ospitali, A. Vaccari, P. Benito and R. Palkovits, *ChemCatChem*, 2019, **11**, 5580–5592.
120 E. M. Iwanek, L. F. Liotta, G. Pantaleo, K. Krawczyk, E. Gdyra, J. Petryk, J. W. Sobczak and Z. Kaszkur, *Catalysts*, 2021, **11**, 325.
121 B. M. Abu-Zied, L. Obalová, K. Pacultová, A. Klegova and A. M. Asiri, *J. Ind. Eng. Chem.*, 2021, **93**, 279–289.

122 E. M. Kostyukhin, A. L. Kustov, N. V. Evdokimenko, A. I. Bazlov and L. M. Kustov, *J. Am. Ceram. Soc.*, 2021, **104**, 492–503.
123 D. Wang, Q. Yao, S. Hui and Y. Niu, *Fuel*, 2019, **251**, 23–29.
124 W. Muhammad, L. Wu, A. El Kasmi, A. Muhammad and Z. Tian, *J. Therm. Sci.*, 2023, **32**, 531–541.
125 Y. Zeng, Z. Wu, L. Guo, Y. Wang, S. Zhang and Q. Zhong, *Mol. Catal.*, 2020, **488**, 110916.
126 Y. Zeng, F. Lyu, Y. Wang, S. Zhang, Q. Zhong and Z. Zhong, *Mol. Catal.*, 2022, **525**, 112356.
127 L. Sheng, Z. Ma, S. Chen, J. Lou, C. Li, S. Li, Z. Zhang, Y. Wang and H. Yang, *Chin. J. Catal.*, 2019, **40**, 1070–1077.
128 Z. Z. Khan, I. A. Khan, I. Khan, M. H. S. Wattoo and A. Badshah, *Solid State Sci.*, 2019, **98**, 106035.
129 D. Wang, Q. Yao, C. Mou, S. Hui and Y. Niu, *Fuel*, 2019, **254**, 115719.
130 F. Zhao, D. Wang, X. Li, Y. Yin, C. Wang, L. Qiu, J. Yu and H. Chang, *Ind. Eng. Chem. Res.*, 2022, **61**, 13854–13862.
131 M.-x Xu, H.-X. Wang, H.-d Ouyang, L. Zhao and Q. Lu, *J. Hazard. Mater.*, 2021, **401**, 123334.
132 M. Zabilskiy, I. Arčon, P. Djinović, E. Tchernychova and A. Pintar, *ChemCatChem*, 2021, **13**, 1814–1823.
133 A. A. Khan, A. Ahmad, H. M. Al-Swaidan, S. Haider, M. S. Akhtar and S. U. Khan, *Mol. Catal.*, 2022, **527**, 112392.
134 C.-G. Liu, Y.-J. Chu, L.-L. Zhang, C. Sun and J.-Y. Shi, *Environ. Sci. Technol.*, 2019, **53**, 12893–12903.
135 M. Wang, W. Li and S. Wang, *J. Phys. Chem. C*, 2023, **127**, 20344–20353.
136 S. Xie, D. Kim, K. Ye, L. Tetard and F. Liu, *J. Rare Earths*, 2023, **41**, 941–951.
137 M. Jabłońska and R. Palkovits, *Catal. Sci. Technol.*, 2016, **6**, 49–72.
138 D. F. Swearer, H. Robatjazi, J. M. P. Martirez, M. Zhang, L. Zhou, E. A. Carter, P. Nordlander and N. J. Halas, *ACS Nano*, 2019, **13**, 8076–8086.
139 D. Tichit and B. Coq, *CATTECH*, 2003, **7**, 206–217.
140 Y. Zhang, X. Wang, Y. Zhu, B. Hou, X. Yang, X. Liu, J. Wang, J. Li and T. Zhang, *J. Phys. Chem. C*, 2014, **118**, 1999–2010.
141 X. Xing, N. Li, J. Cheng, Y. Sun, G. Wang, Z. Zhang, H. Xu, C. He and Z. Hao, *Ind. Eng. Chem. Res.*, 2019, **58**, 9362–9371.
142 F. Gholami, M. Tomas, Z. Gholami and M. Vakili, *Sci. Total Environ.*, 2020, **714**, 136712.
143 A. De Stefanis, M. Dondi, G. Perez and A. Tomlinson, *Chemosphere*, 2000, **41**, 1161–1165.
144 E. E. Kiss, T. J. Vulić and A. F. Reitzmann, *React. Kinet. Catal. Lett.*, 2005, **86**, 233–240.
145 M. C. Karaeyvaz and S. Balci, *Microporous Mesoporous Mater.*, 2021, **323**, 111193.
146 S. Kannan and C. Swamy, *Catal. Today*, 1999, **53**, 725–737.
147 M. Jabłońska, M. A. Arán, A. M. Beale, G. Delahay, C. Petitto, M. Nocuń and R. Palkovits, *Appl. Catal., B*, 2019, **243**, 66–75.
148 Y. Zhang, Y. Guo, N. Li and Y. Feng, *Pol. J. Environ. Stud.*, 2019, **28**, 4477–4484.
149 P. H. Ho, M. Jabłońska, R. Palkovits, E. Rodríguez-Castellón, F. Ospitali, G. Fornasari, A. Vaccari and P. Benito, *Chem. Eng. J.*, 2020, **379**, 122259.
150 S. Xiong, J. Chen, N. Huang, S. Yang, Y. Peng and J. Li, *Environ. Sci. Technol.*, 2019, **53**, 10379–10386.
151 M. Armandi, T. Andana, S. Bensaid, M. Piumetti, B. Bonelli and R. Pirone, *Catal. Today*, 2020, **345**, 59–70.
152 A. Inayat, M. Ayoub, A. Z. Abdullah, S. Ullah and S. R. Naqvi, *Environ. Prog. Sustainable Energy*, 2019, **38**, 13129.
153 D. Lopes, F. Zotin and L. A. Palacio, *Appl. Catal., B*, 2018, **237**, 327–338.
154 J. Akil, C. Ciotonea, S. Siffert, S. Royer, L. Pirault-Roy, R. Cousin and C. Poupin, *Catal. Today*, 2022, **384**, 97–105.
155 C. d O. P. Teixeira, S. da Silva Montani, J. C. S. Soares, L. A. Palacio and F. M. Z. Zotin, *Mol. Catal.*, 2024, **561**, 114157.
156 Z. Zhuang, B. Guan, J. Chen, C. Zheng, J. Zhou, T. Su, Y. Chen, C. Zhu, X. Hu and S. Zhao, *Chem. Eng. J.*, 2024, 150374.
157 Z. Tišler, A. Klegová, E. Svobodová, J. Šafář, K. Strejcová, J. Kohout, S. Šlang, K. Pacultová, D. Rodríguez-Padrón and R. Bulánek, *Catalysts*, 2020, **10**, 1398.
158 G. He, B. Zhang, H. He, X. Chen and Y. Shan, *Sci. Total Environ.*, 2019, **673**, 266–271.
159 L. J. Lobree, I.-C. Hwang, J. A. Reimer and A. T. Bell, *J. Catal.*, 1999, **186**, 242–253.
160 A. Ates, A. Reitzmann, C. Hardacre and H. Yalcin, *Appl. Catal., A*, 2011, **407**, 67–75.
161 M. Rutkowska, A. Jankowska, E. Różycka-Dudek, W. Dubiel, A. Kowalczyk, Z. Piwowarska, S. Llopis, U. Díaz and L. Chmielarz, *Catalysts*, 2020, **10**, 1139.
162 J. Zhang, X. Tang, H. Yi, Q. Yu, Y. Zhang, J. Wei and Y. Yuan, *Appl. Catal., A*, 2022, **630**, 118467.
163 Y. Li and J. N. Armor, *Appl. Catal., B*, 1992, **1**, L21–L29.
164 S. A. Yashnik, O. P. Taran, T. A. Surovtsova, A. B. Ayusheev and V. N. Parmon, *J. Environ. Chem. Eng.*, 2022, **10**, 107950.
165 N. F. Biturini, A. P. N. Santos and M. S. Batista, *React. Kinet., Mech. Catal.*, 2019, **126**, 341–352.
166 P. J. Smeets, J. S. Woertink, B. F. Sels, E. I. Solomon and R. A. Schoonheydt, *Inorg. Chem.*, 2010, **49**, 3573–3583.
167 T. Žumbar, I. Arčon, P. Djinović, G. Aquilanti, G. Žerjav, A. Pintar, A. Ristić, G. Dražić, J. Volavšek and G. Mali, *ACS Appl. Mater. Interfaces*, 2023, **15**, 28747–28762.
168 B. Liu, D. Yao, F. Wu, L. Wei, X. Li and X. Wang, *Ind. Eng. Chem. Res.*, 2019, **58**, 20516–20527.
169 S. Yasumura, H. Ide, T. Ueda, Y. Jing, C. Liu, K. Kon, T. Toyao, Z. Maeno and K.-I. Shimizu, *JACS Au*, 2021, **1**, 201–211.
170 X. Zhang, Q. Shen, C. He, C. Ma, J. Cheng, L. Li and Z. Hao, *ACS Catal.*, 2012, **2**, 512–520.
171 M. Jin, P. Wang, L. Zhang, C. Ao and L. Lei, *Therm. Sci. Eng. Prog.*, 2023, **45**, 102088.
172 M. Jabłońska, M. E. Potter and A. M. Beale, *ChemCatChem*, 2024, **16**, e202301214.
173 C. Ruan, X. Wang, C. Wang, L. Zheng, L. Li, J. Lin, X. Liu, F. Li and X. Wang, *Nat. Commun.*, 2022, **13**, 718.
174 W.-S. Ju, M. Matsuoka and M. Anpo, *Catal. Lett.*, 2001, **71**, 91–93.

175 S. Dzwigaj, D. Reja, S. Koné-Guira, A. Miche, G. Costentin and C. Thomas, *Appl. Catal., A*, 2023, **657**, 119119.
176 M. Shukla, B. V. Chauhan, S. Verma and A. Dhar, *Solids*, 2022, **3**, 665–683.
177 B. Bromley, C. Pischetola, L. Nikoshvili, F. Cárdenas-Lizana and L. Kiwi-Minsker, *Molecules*, 2020, **25**, 3867.
178 B. Kang, M. Li, Z. Di, X. Guo, Y. Wei, J. Jia and R. Zhang, *Catal. Today*, 2022, **402**, 17–26.
179 B. Kang, R. Zhang, M. Guo, X. Guo, Z. Di, Y. Wei and J. Jia, *Energy Fuels*, 2023, **37**(23), 18019–18029.
180 D. Pietrogiacomi, M. C. Campa, L. Ardemani and M. Occhiuzzi, *Catal. Today*, 2019, **336**, 131–138.
181 G. A. Zenkovets, R. A. Shutilov, V. I. Sobolev and V. Y. Gavrilov, *Catal. Commun.*, 2020, **144**, 106072.
182 C. Gao, J. Li, J. Zhang and X. Sun, *Catalysts*, 2020, **10**, 646.
183 J. B. Lim, S. H. Cha and S. B. Hong, *Appl. Catal., B*, 2019, **243**, 750–759.
184 K. M. Farhan, A. N. Thabassum, T. M. Ismail and P. Sajith, *Catal. Sci. Technol.*, 2022, **12**, 1466–1475.
185 B. Zhang, G. He, Y. Shan and H. He, *Catal. Today*, 2019, **327**, 177–181.
186 Y. You, S. Chen, J. Li, J. Zeng, H. Chang, L. Ma and J. Li, *J. Hazard. Mater.*, 2020, **383**, 121117.
187 L. M. Kustov, S. F. Dunaev and A. L. Kustov, *Molecules*, 2022, **27**, 398.
188 S. Li, J. Wang, R. Shang, J. Zhao, Q. Xu, H. Wang and J. Liu, *Mol. Catal.*, 2024, **552**, 113706.
189 X. Liang, H. Tang, F. Yang, G. Tu, F. Zhang, Q. Xiao, Y. Zhong and W. Zhu, *Microporous Mesoporous Mater.*, 2019, **290**, 109655.
190 G. Zhao, E. Benhelal, A. Adesina, E. Kennedy and M. Stockenhuber, *J. Phys. Chem. C*, 2019, **123**, 27436–27447.
191 J. Zeng, S. Chen, Z. Fan, C. Wang, H. Chang and J. Li, *Ind. Eng. Chem. Res.*, 2020, **59**, 19500–19509.
192 J. Cheng, D. Zheng, G. Yu, R. Xu, C. Dai, N. Liu, N. Wang and B. Chen, *ACS Catal.*, 2022, **13**, 934–947.
193 T. Zhang, Y. Qiu, G. Liu, J. Chen, Y. Peng, B. Liu and J. Li, *J. Catal.*, 2020, **392**, 322–335.
194 J. Han, A. Wang, G. Isapour, H. Harelind, M. Skoglundh, D. Creaser and L. Olsson, *Ind. Eng. Chem. Res.*, 2021, **60**, 17826–17839.
195 S. Li, C. Zhang, J. Li, Y. Li, H. Wang, C. Li and Y. Song, *Res. Chem. Intermed.*, 2019, **45**, 3601–3616.
196 G. Sádovská, M. Bernauer, B. Bernauer, E. Tabor, A. Vondrová and Z. Sobalík, *Catal. Commun.*, 2018, **112**, 58–62.
197 M. L. Bols, B. E. Snyder, H. M. Rhoda, P. Cnudde, G. Fayad, R. A. Schoonheydt, V. Van Speybroeck, E. I. Solomon and B. F. Sels, *Nat. Catal.*, 2021, **4**, 332–340.
198 T. Wu, Y. Shen, L. Feng, Z. Tang and D. Zhang, *J. Chem. Eng. Data*, 2019, **64**, 3473–3482.
199 A. J. Shih, J. M. González, I. Khurana, L. P. Ramírez, A. Peña, L. A. Kumar and A. L. Villa, *ACS Catal.*, 2021, **11**, 10362–10376.
200 S. J. Lee, I. S. Ryu, S. G. Jeon and S. H. Moon, *Environ. Prog. Sustainable Energy*, 2019, **38**, 451–456.
201 M. C. Campa, D. Pietrogiacomi, C. Catracchia, S. Morpurgo, J. Olszowka, K. Mlekodaj, M. Lemishka, J. Dedecek, A. Kornas and E. Tabor, *Appl. Catal., B*, 2024, **342**, 123360.
202 E. Tabor, K. Mlekodaj, G. Sádovská, M. Bernauer, P. Klein, P. Sazama, J. Dědeček and Z. Sobalík, *Microporous Mesoporous Mater.*, 2019, **281**, 15–22.
203 E. Tabor, G. Sádovská, M. Bernauer, P. Sazama, J. Nováková, V. Fila, T. Kmječ, J. Kohout, K. Závěta and Z. Sobalík, *Appl. Catal., B*, 2019, **240**, 358–366.
204 N. Pal and A. Bhaumik, *RSC Adv.*, 2015, **5**, 24363–24391.
205 P. Verma, Y. Kuwahara, K. Mori, R. Raja and H. Yamashita, *Nanoscale*, 2020, **12**, 11333–11363.
206 Y. Qin, Z. Qu, C. Dong, Y. Wang and N. Huang, *J. Environ. Sci.*, 2019, **76**, 208–216.
207 M. Marafi and E. Furimsky, *Energy Fuels*, 2017, **31**, 5711–5750.
208 X. Wei, X.-F. Yang, A.-Q. Wang, L. Li, X.-Y. Liu, T. Zhang, C.-Y. Mou and J. Li, *J. Phys. Chem. C*, 2012, **116**, 6222–6232.
209 L. Yu, H. Hu, H. B. Wu and X. W. Lou, *Adv. Mater.*, 2017, **29**, 1604563.
210 K. Pacultová, A. Klegova, T. Kiška, D. Fridrichová, A. Martaus, A. Rokicińska, P. Kuśtrowski and L. Obalová, *Mater. Res. Bull.*, 2020, **129**, 110892.
211 M. C. Campa, A. M. Doyle, G. Fierro and D. Pietrogiacomi, *Catal. Today*, 2022, **384**, 76–87.
212 B. Bozorgi, J. Karimi-Sabet and P. Khadiv-Parsi, *Environ. Technol. Innovation*, 2022, **26**, 102344.
213 T. Umegaki, H. Katori, K. Otake, R. Yamamoto and Y. Kojima, *J. Sol-Gel Sci. Technol.*, 2019, **92**, 715–722.
214 S. Wang, B. Yan, J. Chai, T. Li, H. Yu, T. Li, P. Cao, F. Yang, X. Yuan and H. Yin, *Eur. J. Inorg. Chem.*, 2021, 2201–2210.
215 O. Muccioli, E. Meloni, S. Renda, M. Martino, F. Brandani, P. Pullumbi and V. Palma, *Processes*, 2023, **11**, 1511.
216 Z. Li, B. Li, C. Yu, H. Wang and Q. Li, *Adv. Sci.*, 2023, **10**, 2206605.
217 T. Boningari, D. K. Pappas and P. G. Smirniotis, *J. Catal.*, 2018, **365**, 320–333.
218 D. K. Pappas, T. Boningari, P. Boolchand and P. G. Smirniotis, *J. Catal.*, 2016, **334**, 1–13.
219 P. Nematollahi and M. D. Esrafili, *RSC Adv.*, 2016, **6**, 59091–59099.
220 J.-H. Lee, Y.-J. An, H. Choi, J. Lee, S.-Y. Lee and S.-J. Park, *Appl. Catal., O*, 2024, 206937.
221 M. D. Esrafili and N. Saeidi, *Appl. Surf. Sci.*, 2017, **403**, 43–50.
222 M. D. Esrafili and N. Saeidi, *Appl. Surf. Sci.*, 2018, **444**, 584–589.
223 M. D. Esrafili, *Phys. Lett. A*, 2017, **381**, 2085–2091.
224 B. Gao, J.-X. Zhao, Q.-H. Cai, X.-G. Wang and X.-Z. Wang, *J. Phys. Chem. A*, 2011, **115**, 9969–9976.
225 S. K. Tiwari, S. Sahoo, N. Wang and A. Huczko, *J. Sci.: Adv. Mater. Devices*, 2020, **5**, 10–29.
226 J. Li, M. Zhang, Q. Li and J. Yang, *Appl. Surf. Sci.*, 2017, **391**, 184–193.
227 P. Liu, X. Gu, K. Kang, H. Zhang, J. Cheng and H. Su, *ACS Appl. Mater. Interfaces*, 2017, **9**, 10759–10767.

228 T. Boningari, D. K. Pappas and P. G. Smirniotis, *J. Catal.*, 2018, **365**, 320–333.
229 M. D. Esrafili and N. Saeidi, *Appl. Surf. Sci.*, 2017, **403**, 43–50.
230 M. D. Esrafili and S. Heydari, *Mol. Phys.*, 2020, 1–8, DOI: 10.1080/00268976.2020.1759830,.
231 M. D. Esrafili, *Phys. Lett. A*, 2017, **381**, 2085–2091.
232 M. D. Esrafili and S. Heidari, *Chem. Phys. Lett.*, 2019, **725**, 52–58.
233 J. Sun, L. Wang, L. Zhang, Y. Zhao, Y. Chi, H. Wang, C. Li, J. Liu and J. Liu, *ACS Appl. Energy Mater.*, 2021, **4**, 8496–8505.
234 X. Liu and L. Sheng, *Mater. Today Commun.*, 2021, **28**, 102585.
235 G. Fan, Q. Wang, H. Xu, X. Wang, X. Tu and X. Chu, *Appl. Surf. Sci.*, 2021, **544**, 148776.
236 Y. Xiong, Y. Zhao, W. Shan, X. Feng, J. Cui, Z. Lou, G. Shao, M. Dong and H. Yu, *Chemosphere*, 2022, **303**, 135257.
237 Y. Xiong, Y. Zhao, X. Qi, J. Qi, Y. Cui, H. Yu and Y. Cao, *Environ. Sci. Technol.*, 2021, **55**, 13335–13344.
238 E. Meloni, M. Martino, S. Renda, O. Muccioli, P. Pullumbi, F. Brandani and V. Palma, *Catalysts*, 2022, **12**, 1405.
239 X. Guan, H. Asakura, R. Han, S. Xu, H.-X. Liu, L. Chen, Z. Yao, J. H. C. Yan, T. Tanaka and Y. Guo, *ACS Catal.*, 2023, **13**, 13816–13827.
240 A. Hassanpour, M. Kamel, S. Ebrahimiasl, A. G. Ebadi, S. Arshadi and Z. Ghulinezhad Ahangari, *J. Mol. Model.*, 2022, **28**, 1–14.
241 X. Hu, E. Zhang, W. Li, L. Wu, Y. Zhou, H. Zhang and C. Dong, *Appl. Sci.*, 2022, **12**, 5034.
242 X. Tan, S. Qi, G. Cheng, C. Yi and B. Yang, SSRN, 2023, preprint, DOI: 10.2139/ssrn.4470798.
243 M. Derdare, A.-G. Boudjahem and M. Boulbazine, *Struct. Chem.*, 2022, **33**, 2043–2062.
244 M. D. Esrafili, S. Asadollahi and S. Heydari, *J. Mol. Graphics Modell.*, 2019, **89**, 41–49.
245 A. A. Khan, M. D. Esrafili, F. Ali, R. Ahmad and I. Ahmad, *J. Mol. Graphics Modell.*, 2022, **114**, 108186.
246 P. Li, T. Zhang, H. Sun, Y. Gao, Y. Zhang, Y. Liu, C. Ge, H. Chen, X. Dai and X. Zhang, *Nano Res.*, 2022, **15**, 3001–3009.
247 J. Qi, X. Qi, Y. Pan, J. Cui, Y. Xiong, W. Shan and H. Yu, *Appl. Surf. Sci.*, 2023, **611**, 155657.
248 Y. Bai, Y. Hou, Y. Guo, N. Xiang, X. Han, H. Wang, Z. Wu and Z. Huang, *J. Colloid Interface Sci.*, 2022, **616**, 55–66.
249 Z. Liu, H. Wang, Y. Gao and J. Zhao, *Molecules*, 2023, **28**, 4485.
250 M. D. Esrafili and B. Nejadebrahimi, *Chem. Phys. Lett.*, 2019, **716**, 11–16.
251 X. Dai, Y. Cheng, T. Liu and L. Mao, *Energy Fuels*, 2024, **38**(11), 9262–9279.
252 T. Das, B. K. Sharma, A. K. Katiyar and J.-H. Ahn, *J. Semicond.*, 2018, **39**, 011007.
253 A. Akça, O. Karaman and C. Karaman, *ECS J. Solid State Sci. Technol.*, 2021, **10**, 041003.
254 X. Liu and L. Sheng, *Adv. Theory Simul.*, 2023, **6**, 2200680.
255 R. Gholizadeh, Y.-X. Yu and Y. Wang, *Appl. Surf. Sci.*, 2017, **420**, 944–953.
256 M. D. Esrafili, *Chem. Phys. Lett.*, 2018, **708**, 94–99.
257 M. D. Esrafili, *Chem. Phys. Lett.*, 2018, **705**, 44–49.
258 M. Vakili, R. Gholizadeh, A. Ghadi, E. Salmasi and M. Sinnokrot, *J. Mol. Graphics Modell.*, 2020, **101**, 107752.
259 Z. Liu, X.-r Cheng, Y.-m Yang, H.-z Jia, B.-q Bai and L. Zhao, *Materials*, 2019, **12**, 2611.
260 I. Majeed, U. Manzoor, F. K. Kanodarwala, M. A. Nadeem, E. Hussain, H. Ali, A. Badshah, J. A. Stride and M. A. Nadeem, *Catal. Sci. Technol.*, 2018, **8**, 1183–1193.
261 L. Hu, J. Yan, C. Wang, B. Chai and J. Li, *Chin. J. Catal.*, 2019, **40**, 458–469.
262 K. U. Sahar, K. Rafiq, M. Z. Abid, U. ur Rehman, A. Rauf and E. Hussain, *React. Chem. Eng.*, 2023, **8**, 2522–2536.
263 I. Troppová, M. Šihor, M. Reli, M. Ritz, P. Praus and K. Kočí, *Appl. Surf. Sci.*, 2018, **430**, 335–347.
264 D. Ma, X. Cao and Z. Cao, *J. Phys. Chem. C*, 2023, **127**, 5800–5809.
265 M. D. Esrafili, *Chem. Phys. Lett.*, 2018, **708**, 94–99.
266 M. D. Esrafili and E. Vessally, *Surf. Sci.*, 2018, **667**, 105–111.
267 R. Gholizadeh, Y.-X. Yu and Y. Wang, *Appl. Surf. Sci.*, 2017, **420**, 944–953.
268 M. D. Esrafili, F. Mohammadian-Sabet and P. Nematollahi, *RSC Adv.*, 2016, **6**, 64832–64840.
269 P. Praus, L. Svoboda, M. Ritz, I. Troppová, M. Šihor and K. Kočí, *Mater. Chem. Phys.*, 2017, **193**, 438–446.
270 K. Kočí, M. Reli, I. Troppová, M. Šihor, J. Kupková, P. Kustrowski and P. Praus, *Appl. Surf. Sci.*, 2017, **396**, 1685–1695.
271 M. Reli, L. Svoboda, M. Šihor, I. Troppová, J. Pavlovský, P. Praus and K. Kočí, *Environ. Sci. Pollut. Res.*, 2018, **25**, 34839–34850.
272 K. Kočí, M. Reli, I. Troppová, M. Šihor, T. Bajcarová, M. Ritz, J. Pavlovský and P. Praus, *Catalysts*, 2019, **9**, 735.
273 M. Reli, I. Troppová, M. Šihor, J. Pavlovský, P. Praus and K. Kočí, *Appl. Surf. Sci.*, 2019, **469**, 181–191.
274 P. Praus, J. Lang, A. Martaus, L. Svoboda, V. Matějka, M. Kormunda, M. Šihor, M. Reli and K. Kočí, *J. Inorg. Organomet. Polym. Mater.*, 2019, **29**, 1219–1234.
275 V. Matějka, M. Šihor, M. Reli, A. Martaus, K. Kočí, M. Kormunda and P. Praus, *Mater. Sci. Semicond. Process.*, 2019, **100**, 113–122.
276 P. Maitarad, A. Junkaew, V. Promarak, L. Shi and S. Namuangruk, *Appl. Surf. Sci.*, 2020, **508**, 145255.
277 S. Su, J. Ma, Z. Liu, D. Holiharimanana and H. Sun, *Catalysts*, 2023, **13**, 578.
278 M. D. Esrafili and S. Heydari, *Mol. Phys.*, 2020, **118**, e1759830.
279 X. Hu, Y. Wang, R. Wu and Y. Zhao, *Appl. Surf. Sci.*, 2021, **538**, 148157.
280 D. Masih, Y. Ma and S. Rohani, *Appl. Catal., B*, 2017, **206**, 556–588.
281 J. O. Ighalo, M. L. Smith, A. Al Mayyahi and P. B. Amama, *Appl. Catal., B*, 2024, 124352.
282 S. Zhao, D. Chen, N. Li, Q. Xu, H. Li and J. Lu, *J. Alloys Compd.*, 2023, **960**, 170830.
283 B. Huang, Y. F. Wu, Z. Zhang, R. Chen, G. Y. Ren, N. Zhou, N. Li and Y. Qian, *J. Mater. Chem. A*, 2025, **13**, 16970–16980.

284 Y.-X. Yu, *J. Colloid Interface Sci.*, 2025, 137799.
285 B. Huang, G. y Ren, R. Chen and N. Li, *Chem. Phys. Lett.*, 2025, **874–875**, 142178.
286 X. Hu, Y. Wang, Z. Ling, H. Song, Y. Cai, Z. Li, D. Zu and C. Li, *Appl. Surf. Sci.*, 2021, **556**, 149817.
287 A. Al Mayyahi, S. Sarker, B. M. Everhart, B. Tonyali, U. Yucel and P. B. Amama, *J. Phys. Chem. Solids*, 2022, **170**, 110875.
288 A. Hermawan, T. Hasegawa, Y. Asakura and S. Yin, *Sep. Purif. Technol.*, 2021, **270**, 118815.
289 A. A. Mayyahi, S. Sarker, B. M. Everhart, X. He and P. B. Amama, *Mater. Today Commun.*, 2022, **32**, 103835.
290 L. Kong, M. Wang and C.-M. L. Wu, *ACS Mater. Lett.*, 2024, **6**, 1711–1721.
291 H. D. Mai, K. Rafiq and H. Yoo, *Chem. – Eur. J.*, 2017, **23**, 5631–5651.
292 S. M. Rogge, A. Bavykina, J. Hajek, H. Garcia, A. I. Olivos-Suarez, A. Sepúlveda-Escribano, A. Vimont, G. Clet, P. Bazin and F. Kapteijn, *Chem. Soc. Rev.*, 2017, **46**, 3134–3184.
293 A. Bavykina, N. Kolobov, I. S. Khan, J. A. Bau, A. Ramirez and J. Gascon, *Chem. Rev.*, 2020, **120**, 8468–8535.
294 K. Rafiq, H. D. Mai, J. K. Kim, J. M. Woo, B. M. Moon, C. H. Park and H. Yoo, *Sens. Actuators, B*, 2017, **251**, 472–480.
295 F. Ahmad, K. Rafiq, T. Najam, E. Hussain, M. Sohail, M. Z. Abid, A. Mahmood, M. S. Javed and S. S. A. Shah, *Int. J. Hydrogen Energy*, 2023, **48**(90), 35075–35111.
296 S. Ketrat, T. Maihom, S. Wannakao, M. Probst, S. Nokbin and J. Limtrakul, *Inorg. Chem.*, 2017, **56**, 14005–14012.
297 P. Zhao, F. Qin, Z. Huang, C. Sun, W. Shen and H. Xu, *Chem. Eng. J.*, 2018, **349**, 72–81.
298 V. Paluka, T. Maihom, M. Probst and J. Limtrakul, *Phys. Chem. Chem. Phys.*, 2020, **22**, 13622–13628.
299 S. Chen, Y. Zhou, J. Li, Z. Hu, F. Dong, Y. Hu, H. Wang, L. Wang, K. K. Ostrikov and Z. Wu, *ACS Catal.*, 2020, **10**, 10185–10196.
300 H. Louis, T. C. Egemonye, T. O. Unimuke, B. E. Inah, H. O. Edet, E. A. Eno, S. A. Adalikwu and A. S. Adeyinka, *ACS Omega*, 2022, **7**, 34929–34943.
301 K. D. Vogiatzis, E. Haldoupis, D. J. Xiao, J. R. Long, J. I. Siepmann and L. Gagliardi, *J. Phys. Chem. C*, 2016, **120**, 18707–18712.
302 S. Ketrat, T. Maihom, S. Wannakao, M. Probst, S. Nokbin and J. Limtrakul, *Inorg. Chem.*, 2017, **56**, 14005–14012.
303 V. Paluka, T. Maihom, M. Probst and J. Limtrakul, *Phys. Chem. Chem. Phys.*, 2020, **22**, 13622–13628.
304 S. Chen, Y. Zhou, J. Li, Z. Hu, F. Dong, Y. Hu, H. Wang, L. Wang, K. Ostrikov and Z. Wu, *ACS Catal.*, 2020, **10**(17), 10185–10196.
305 D. Denysenko, J. Jelic, O. V. Magdysyuk, K. Reuter and D. Volkmer, *Microporous Mesoporous Mater.*, 2015, **216**, 146–150.
306 A. Dey, T. Albert, R. Y. Kong, S. N. MacMillan, P. Moënne-Loccoz, K. M. Lancaster and D. P. Goldberg, *Inorg. Chem.*, 2022, **61**, 14909–14917.
307 H. Tang, Y. He, P. Liu, J. Shao, F. Lin and Z. Wang, *Energy Fuels*, 2021, **35**, 18664–18679.
308 Z. Yao, D. Qu, Y. Guo, Y. Yang and H. Huang, *Adv. Mater. Sci. Eng.*, 2019, **2019**, 1–9.
309 N. J. Halas, P. Nordlander, H. Robatjazi, D. F. Swearer, C. Zhang, H. Zhao and L. Zhou, *US Pat.*, US10766024B2 2020.
310 D. F. Swearer, H. Zhao, L. Zhou, C. Zhang, H. Robatjazi, J. M. P. Martirez, C. M. Krauter, S. Yazdi, M. J. McClain and E. Ringe, *Proc. Natl. Acad. Sci. U. S. A.*, 2016, **113**, 8916–8920.
311 K. Rafiq, I. Sadia, M. Z. Abid, M. Z. Waleed, A. Rauf and E. Hussain, *ACS Biomater. Sci. Eng.*, 2024, **10**, 7268–7313.
312 R. Nava, B. Pawelec, P. Castaño, M. C. Álvarez-Galván, C. V. Loricera and J. L. G. Fierro, *Appl. Catal., B*, 2009, **92**, 154–167.
313 G. J. Kubas, *Chem. Rev.*, 2007, **107**, 4152–4205.
314 B. Kim, Z. Li, B. D. Kay, Z. Dohnálek and Y. K. Kim, *J. Phys. Chem. C*, 2014, **118**, 9544–9550.
315 S. Royer, D. Duprez, F. Can, X. Courtois, C. Batiot-Dupeyrat, S. Laassiri and H. Alamdari, *Chem. Rev.*, 2014, **114**, 10292–10368.
316 I. Fechete, Y. Wang and J. C. Védrine, *Catal. Today*, 2012, **189**, 2–27.
317 T. Selvaraj, P. Aghalayam and J. J. Varghese, *Ind. Eng. Chem. Res.*, 2024, **63**, 6591–6599.
318 E. Winter, *J. Catal.*, 1969, **15**, 144–152.
319 E. V. Kondratenko and J. Pérez-Ramírez, *J. Phys. Chem. B*, 2006, **110**, 22586–22595.
320 S. Subramanian and C. Swamy, *Catal. Lett.*, 1995, **35**, 361–372.